



Norwegian University of
Science and Technology

Experimental and numerical study on perforated plates subjected to blast loading

Benjamin Stavnar Elveli

Master of Science in Mechanical Engineering

Submission date: June 2018

Supervisor: Vegard Aune, KT

Co-supervisor: Tore Børvik, MTP

Norwegian University of Science and Technology
Department of Structural Engineering



MASTER THESIS 2018

| | | |
|--|-------------------------------------|----------------------|
| SUBJECT AREA: Computational Mechanics | DATE: June 11 th 2018 | NO. OF PAGES: 129 |
|--|-------------------------------------|----------------------|

TITLE:

Experimental and numerical study on perforated steel plates subjected to blast loading

Eksperimentelt og numerisk studie av perforerte stålplater utsatt for eksplosjonslast

BY:

Benjamin Stavnar Elveli

Mads Bakken Iddberg



SUMMARY:

This thesis investigates the behavior of deformable steel plates exposed to blast-loading, using experimental two numerical studies. The numerical work consists of a preliminary study and a numerical study with more realistic models. All experiments were conducted in the SIMLab Shock Tube Facility (SSTF) at the Norwegian University of Technology and Science (NTNU). The tested plates were made from 0.8 mm thick Docol 600DL steel with a 300 mm x 300 mm blast-exposed area. In total, four different plate-geometries were tested; two configurations containing square holes, and two configurations containing slits. The purpose of including holes and slits was to study crack propagation and fluid-structure interaction effects in the plates. The experimental results were documented through the use of two high-speed cameras, three-dimensional digital image correlation, laser scanning of the deformed plates and high frequency pressure measurements.

The objective of the preliminary study was to determine a test matrix to execute experimentally in the SSTF. The geometry of the tested plates, and the intensity of the applied blast load were determined in this part. The numerical models neglected fluid-structure interaction effects, and were all run solely in Abaqus Explicit. The loading was applied as idealized pressure-time curves. A benchmark for the numerical models in the preliminary study was created from the previous testing done at NTNU. The effects of element size, element type, boundary conditions, friction coefficients, and strain rate sensitivity were explored in separate parametric studies.

In total 13 plates were tested during the experiments. The four configurations were all tested at the nominal firing pressures associated with three distinct responses; complete failure, crack arrest, and deformation with limited to no cracking. The intended response was accomplished for all configurations except one.

In the numerical study with more realistic models, numerical solutions were compared to the experimental data for validation. This study includes pure Lagrangian models in Abaqus Explicit and models in Europlexus, which includes fluid structure interaction.

RESPONSIBLE TEACHER: Vegard Aune

SUPERVISOR(S): Vegard Aune and Tore Børvik

CARRIED OUT AT: Department of Structural Engineering, NTNU



MASTEROPPGAVE 2018

| | | |
|----------------------------------|------------------------|----------------------|
| FAGOMRÅDE: Beregningsmekanikk | DATO: 11. juni 2018 | ANTALL SIDER: 129 |
|----------------------------------|------------------------|----------------------|

TITTEL:

Eksperimentelt og numerisk studie av perforerte stålplater utsatt for eksplosjonslast

Experimental and numerical study on perforated steel plates subjected to blast loading

UTFØRT AV:

Benjamin Stavnar Elveli

Mads Bakken Iddberg



SAMMENDRAG:

Hovedmålet med denne oppgaven er å studere deformerbare stålplater utsatt for eksplosjonslast ved hjelp av et eksperimentelt og et numerisk studie. Det numeriske arbeidet består av et forstudie og et påfølgende numerisk studie med mer avanserte modeller. Alle eksperimenter ble utført i SIMLab Shock Tube Facility (SSTF) ved Norges teknisk-naturvitenskapelige universitet (NTNU). Platene var laget av 0.8 mm tykt Docol 600DL stål og hadde et lasutsatt område på 300 mm x 300 mm. Totalt ble fire forskjellige plategeometrier testet; to konfigurasjoner som inneholder firkantede hull og to konfigurasjoner som inneholdt slisser. Hensikten med å inkludere hull og slisser var å studere strukturoppførselen og fluid-struktur-interaksjonseffekter i platene. De eksperimentelle resultatene ble dokumentert av to høyhastighets kameraer, tredimensjonal digital bildekorrelasjon, laserskanning av deformerte plater og av høyfrekvente trykkmålinger.

Gjennom å bestemme geometrien til platene og lastintensiteten var formålet med forstudiet å bestemme en testmatrise. De numeriske modellene i denne studien neglisjerte fluid-struktur interaksjon, og alle modeller ble kjørt i Abaqus Eksplisitt. Lasten ble påført som idealiserte trykk-tidskurver. Modellene ble vurdert opp mot tidligere studier utført på NTNU, og ulike numeriske modellparametere ble studert.

13 eksperimentelle forsøk ble gjennomført, og alle de fire konfigurasjonene var tiltenkt tre ulike oppførsler. Dette var total kollaps av platen, sprekk arrestasjon og deformasjon med begrenset eller ingen sprekkvekst. Det tiltenkte testresultatet ble oppnådd for alle konfigurasjoner bortsett fra en.

Den numeriske studien som ble gjennomført etter forsøksdataene var behandlet, var ment som en sammenligningen mellom testdata og geometrisk komplekse modeller som kun beskrev strukturen med en Lagrange beskrivelse. I tillegg ble det kjørt modeller i Europlexus, dette ble gjort for å undersøke fluid-struktur interaksjonen.

MASTER'S THESIS 2018

for

Benjamin Stavnar Elveli and Mads Bakken Iddberg

Experimental and numerical study on perforated steel plates subjected to blast loading

1. INTRODUCTION

Protection of engineering structures against blast loading has received a lot of attention in recent years. Steel is often a preferred material due to its combination of high strength, high ductility and good formability, resulting in an effective load carrying capability at a relatively low cost compared to many other materials. Since plated structures are frequently being used in engineering applications, it has become necessary to predict the structural response of such components exposed to blast loading. Moreover, plated structures are often perforated (e.g. for design purposes or by fragments accelerated by the blast and impacting the target plate prior to the blast pressure). This introduces the need to consider the influence of such perforations on the overall performance of plated structures. Computational methods are now available to predict both the loading and structural response in these extreme loading situations, and experimental validation of such methods is necessary in the development of safe and cost-effective protective structures. In this study blast experiments will be performed, and the data will be used for validation and verification of some frequently used computational methods involving blast loading.

2. OBJECTIVES

The main objective of the research project is to determine how thin perforated steel plates behave under blast loading, and to validate to which extent this can be predicted using computational tools. Special focus is placed on the influence of pre-cut defects on the performance of the perforated plates.

3. A SHORT DESCRIPTION OF THE RESEARCH PROJECT


The main topics in the research project will be as follows;

1. A comprehensive literature review should be conducted to understand the blast load phenomenon, blast load design, shock tube facilities, constitutive and failure modeling of steel plates exposed to extreme loadings, and explicit finite element methods.
2. The steel plates are manufactured from medium-strength, high-hardening and cold-rolled sheets of type Docol 600DL. Material data and calibrated material input for the numerical simulations will be based on previous studies in the literature.
3. The SIMLab Shock Tube Facility will be used to expose perforated plates to blast loading, as an alternative to explosive detonations. The shock tube experiments will be used to investigate typical dynamic responses and failure modes of perforated plates exposed to blast loading.
4. Digital Image Correlation (DIC) and laser scanning will be used to measure the 3D transverse displacement fields of the plates in the shock tube experiments.
5. Non-linear FE numerical simulations of the shock tube experiments will be performed, and the numerical results shall be compared and discussed based on the experimental findings.

Supervisors: Vegard Aune (NTNU), Tore Børvik (NTNU)

The thesis must be written according to current requirements and submitted to the Department of Structural Engineering, NTNU, no later than June 11th, 2018.

NTNU, January 15th, 2018


Vegard Aune
Associate Professor

Abstract

This thesis investigates the behavior of deformable steel plates exposed to blast-loading, using experimental and numerical studies. The numerical work consists of a preliminary study and a numerical study with more realistic models. All experiments were conducted in the SIMLab Shock Tube Facility (SSTF) at the Norwegian University of Technology and Science (NTNU). The tested plates were made from 0.8 mm thick Docol 600DL steel with a 300 mm x 300 mm blast-exposed area. In total, four different plate-geometries were tested; two configurations containing square holes, and two configurations containing slits. The purpose of including holes and slits was to study crack propagation and fluid-structure interaction effects in the plates. The experimental results were documented through the use of two high-speed cameras, three-dimensional digital image correlation, laser scanning of the deformed plates and high-frequency pressure measurements.

The objective of the preliminary study was to determine a test matrix to execute experimentally in the SSTF. The geometry of the tested plates and the intensity of the applied blast load were determined in this part. The numerical models neglected fluid-structure interaction effects and were all run solely in Abaqus Explicit. The loading was applied as idealized pressure-time curves. A benchmark for the numerical models in the preliminary study was created from the previous testing done at NTNU. The effects of element size, element type, boundary conditions, friction coefficients, and strain rate sensitivity were explored in separate parametric studies.

In total 13 plates were tested during the experiments. The four configurations were all tested at the nominal firing pressures associated with three distinct responses; complete failure, crack arrest, and deformation with limited to no cracking. The intended response was accomplished for all configurations except one.

In the numerical study with more realistic models, numerical solutions were compared to the experimental data for validation. This study includes pure Lagrangian models in Abaqus Explicit and models in Europlexus, which includes fluid-structure interaction.

Acknowledgements

This thesis is written for SIMLab/SFI-CASA at Norwegian University of Science and Technology (NTNU). The Center for Advanced Structural Analysis (CASA) was opened on July 1st, 2015, and it aims to build an attractive scientific working environment where fundamental knowledge is created through multidisciplinary theoretical, numerical and experimental research on different scales. The main objective is to provide a research and technology platform for the creation and development of smart, cost-effective, safe and environmentally friendly structures and products through multi-scale testing, modelling, and simulation. The thesis serves as a continuance of The doctoral thesis of Vegard Aune, and The masters thesis of Henrik Granum and Lars Marcus Løken, on the behavior and modeling of blast-loaded structures.

The topic of blast-loading and protective structures has been subject to a number of research projects at CASA recent years. We are thankful for the opportunity to work with this topic. The work on this thesis has been challenging and at times frustrating but has always been exciting. It has given us a great educational experience and motivated us for the coming challenges as engineers in the future.

We would like to thank our supervisors Associate Professor Vegard Aune and Professor Tore Børvik for guidance and interesting discussions through weekly meetings. A special thanks goes to Vegard Aune for always being interested and helpful through our many problems along the way. Your passion and curiosity for your work and our thesis is much appreciated.

We would also like to thank Mr. Trond Auestad for your help during the shock tube experiments, Professor Torodd Berstad for helping us with the cluster "Snurre" and Dr. Egil Fagerholt for helpful input for analyses in eCorr.

Lastly, we would like to thank Christoffer Martinsen, Vegard Haraldseid, Olaf Kieland, Sigurd Lekve and Nikolai Skåre for the many discussions and for the good company throughout the year.

Contents

| | | |
|----------|--|-----------|
| 1 | Introduction | 1 |
| 2 | Theory | 5 |
| 2.1 | Characteristics of a shock wave | 5 |
| 2.1.1 | Chemical explosions | 5 |
| 2.1.2 | Mechanical explosions | 6 |
| 2.1.3 | Shock wave | 6 |
| 2.2 | Basic shock tube design and function | 7 |
| 2.3 | Lagrangian and Eulerian description | 9 |
| 2.4 | Explicit finite element methods | 10 |
| 2.4.1 | Mass scaling | 11 |
| 2.4.2 | Energy considerations | 12 |
| 2.4.3 | Element erosion | 12 |
| 2.4.4 | Adaptive mesh refinement | 12 |
| 2.4.5 | Contact formulations | 13 |
| 2.5 | Computational fluid dynamics | 15 |
| 2.5.1 | Conservation laws in fluid dynamics | 15 |
| 2.5.2 | Equation of state | 18 |
| 2.5.3 | Discretization of the flow regime | 18 |
| 2.6 | Modeling of blast-loaded structures | 18 |
| 2.6.1 | The Lagrangian approach | 18 |
| 2.6.2 | Euler-Lagrange methods | 20 |
| 2.6.3 | Loading regimes | 20 |
| 2.6.4 | Fluid-structure interaction algorithms in Europlexus | 21 |
| 2.7 | Previous work | 22 |
| 3 | Material models | 25 |
| 3.1 | Docol 600DL steel | 25 |
| 3.1.1 | Previously conducted material testing | 25 |
| 3.1.2 | Model assumptions | 27 |
| 3.1.3 | Elastic behavior | 27 |
| 3.1.4 | Yield criteria | 28 |
| 3.1.5 | Strain hardening and flow stress | 28 |
| 3.1.6 | Viscoplasticity | 30 |

Contents

| | | |
|----------|---|-----------|
| 3.1.7 | Thermal softening | 30 |
| 3.1.8 | Modified Johnson-Cook | 31 |
| 3.1.9 | Ductile fracture | 32 |
| 3.2 | Shock wave propagation in air | 32 |
| 3.2.1 | The Euler equations | 33 |
| 3.2.2 | Equation of state for air | 33 |
| 3.2.3 | Fluid parameters | 34 |
| 4 | Preliminary study part I | 35 |
| 4.1 | Description | 36 |
| 4.2 | Models | 37 |
| 4.2.1 | Description of the shell element models | 38 |
| 4.2.2 | Description of the solid element models | 41 |
| 4.3 | Results | 42 |
| 4.3.1 | Benchmark study | 42 |
| 4.3.2 | New plate configurations | 50 |
| 4.3.3 | Resulting test matrix | 60 |
| 4.4 | Discussion | 60 |
| 4.4.1 | Element size and formulation | 60 |
| 4.4.2 | Structural response | 61 |
| 4.4.3 | Comparison to other numerical studies | 62 |
| 5 | Preliminary study part II | 63 |
| 5.1 | Description | 63 |
| 5.2 | Models | 64 |
| 5.2.1 | Complex model | 64 |
| 5.3 | Results | 66 |
| 5.3.1 | Effect of rate dependency and thermal softening | 66 |
| 5.3.2 | Effect of friction | 68 |
| 5.4 | Concluding remarks | 70 |
| 6 | Experimental work | 71 |
| 6.1 | Experimental setup | 71 |
| 6.1.1 | The SIMLab shock tube facility | 71 |
| 6.1.2 | Measuring equipment and calibration | 73 |
| 6.1.3 | Plate setup | 74 |
| 6.1.4 | Three-dimensional digital image correlation | 74 |
| 6.1.5 | Laser scanning | 76 |
| 6.2 | Experimental results | 77 |
| 6.2.1 | Post test images | 78 |
| 6.2.2 | Pressure-time data | 79 |
| 6.2.3 | Midpoint displacements data | 84 |
| 6.2.4 | Deformation profiles | 86 |
| 6.2.5 | Laser scanning and final deformation profiles | 89 |
| 6.2.6 | Observed failure modes | 93 |

| | | |
|----------|---|------------|
| 6.2.7 | Measured crack lengths | 96 |
| 6.2.8 | Concluding remarks | 99 |
| 7 | Numerical work | 101 |
| 7.1 | Description | 101 |
| 7.2 | Numerical models | 102 |
| 7.2.1 | Lagrangian models in Abaqus | 102 |
| 7.2.2 | Europlexus | 102 |
| 7.2.3 | Naming convention | 104 |
| 7.3 | Validation of Abaqus models | 105 |
| 7.3.1 | Evaluation of failure modes and cracking | 105 |
| 7.3.2 | Evaluation of displacements | 107 |
| 7.4 | Comparison of Lagrangian models in Abaqus and Europlexus | 109 |
| 7.5 | Fluid structure interaction effects | 111 |
| 7.5.1 | Midpoint displacement response | 111 |
| 7.5.2 | Pressure evolution in front of the plates | 114 |
| 7.6 | Concluding remarks | 120 |
| 8 | Concluding remarks | 123 |
| 8.1 | Summary and discussion | 123 |
| 8.2 | Conclusions | 126 |
| 8.3 | Further work | 127 |
| | Appendices | 139 |
| A | Experimental results | i |
| A.1 | Failure modes obtained from [30] | ii |
| A.1.1 | Experimentally measured midpoint displacements. | iii |
| A.1.2 | Experimental deformation evolution | iii |
| B | Numerical results | vii |
| B.1 | Energy plots from Chapter 5 | vii |
| B.2 | Midpoint displacement plots for from Chapter 7 | x |
| B.3 | Effect of excluding the pre-tension in the bolts for the clamping frame | xi |
| B.3.1 | Tables from Chapter 7 | xiii |
| B.3.2 | Pressure distribution from Chapter 7 | xv |
| B.3.3 | Varying the strain rate sensitivity for P3 and S2 | xvi |
| B.3.4 | Evaluation of displacements, from Chapter 7 | xviii |

Chapter 1

Introduction

Explosives-based terrorist attacks and accidents involving explosions have extensive social and structural damage potential. Civilian structures subjected to loading from such events are often lightweight and flexible, leaving them less protected than traditional military installations. Historically, most research in the field of blast-resistant design was focused on fortified structures. However, the last couple of decades has seen a significant increase in research concerning more lightweight structures subjected to blast loading.

The SIMlab shock tube facility (SSTF) allows for studies on blast loaded structures in a very predictable and controlled manner, making it well suited for comparison and validation of numerical methods. The shock tube allows one to choose the area of focus for experimentation specifically. Material response, shock wave propagation and the interaction between the structure and the shock wave are all relevant phenomena that have to be studied in detail in this context. Knowledge about the governing parameters pertaining to these phenomena and how they affect the loading and the structural response in an isolated manner, can thus be applied to more complex problems.

Thin plate structures are often present in buildings, explosion may subject these plates to the combination of fragments and shock waves. Fragments can cause both slits and perforations, or the structure can be perforated for design purposes. Both slits and perforations can effect the structural behavior of the plates, but these can also affect an incoming shock wave. Full-scale testing is seldom an option when estimating a potential threat. Because of this, it is important to have a trustworthy numerical framework that is validated through controlled experiments.

This thesis focuses on the structural response of thin Docol 600DL steel plates subjected to blast loading created in the shock tube. This is done by planning and executing a series of tests, as well as running numerical simulations. In order to set up an experimental test series, a two-part preliminary study was conducted. This resulted in a pre-planned test matrix consisting of 12 separate tests. All tests were conducted on 0.8 mm thick plates, with four different geometrical configurations. The

Chapter 1. Introduction

different geometrical configurations are all a continuation of previous work at NTNU, and consists of two perforated- and two slitted configurations.

In blast problems, the loading and the structural response are often mutually dependent. The tested configurations are designed with this in mind and are meant to provoke fluid structure interaction effects as well as to challenge the numerical tools available.

Depending on the design of the blast-exposed plate, it may be subjected to large plastic deformations, fracture and possibly complete failure and fragmentation. The deformation process typically takes a few milliseconds, and due to the high non-linearity of the problem, the structural response of the plate is preferentially handled by explicit finite element methods. Numerical models of the plate problem have to describe the material behavior by taking into account; large plastic strains, visco-plastic behavior, possibly temperature dependency and a fracture criterion. In addition to the description of the purely structural response, the complete solution to the problem also needs to incorporate a description of the loading of the structure. This can be done by considering the full fluid-structure interaction, or by modeling the blast load using simplified approaches. Both methods will be described and applied in this thesis.

Chapter 2, Theory: Gives an introduction to the blast phenomenon and methods for a numerical representation of blast loadings. Theoretical topics explicitly related to the numerical framework used for the models in this thesis are also presented. The given theory is not intended to be a thorough description but meant as an introduction to some of the most important aspects pertaining to this thesis. A literature survey on previous work will also be presented.

Chapter 3, Material: Explains how the material behavior of the Docol 600DL steel is modeled in the numerical work. The assumptions that are made to idealize the model of the material are specified. The modified Johnson-Cook relation and the Cockcroft-Latham fracture criteria are also presented.

Chapter 4, Preliminary study Part I: Aims to develop a test matrix for the experimental work and to study the structural response of the plates. To evaluate the numerical response, a benchmark study was conducted. The benchmark study includes experimental results obtained from previous studies at NTNU.

Chapter 5, Preliminary study Part II: Is a continuation of the findings from the first benchmark study in part I. More realistic boundary conditions are introduced through the modeling of the clamping frames and bolts holding the plates in place. This new and more realistic description gives rise to the inclusion of contact modeling and the calibration of a friction coefficient. In addition, it involves a parametric study on the strain rate sensitivity, which was found to be important when evaluating fracture in the plates.

Chapter 6, Experimental work: Presents the experimental work, where the test matrix obtained in the preliminary study was tested in the SSTF. All tests are analyzed through the use of high-speed cameras and 3D-DIC, synchronized with high-frequency measurements of the reflected pressure. Post-test pictures, laser scanning of the deformed plates, obtained crack lengths, deformation profiles, and midpoint data will be presented and discussed.

Chapter 7, Numerical work: Serves as a final numerical study of the problem, taking both experimental- and numerical results from the previous chapters into account. In this section, fully coupled Eulerian-Lagrangian models in Europlexus are compared to purely Lagrangian models in Abaqus.

Chapter 2

Theory

This chapter aims to cover some of the most relevant theory needed to describe the shock tube experiments and the applied numerical framework. The starting point will be the characteristics of a shock wave followed by an introduction to the basic shock tube design and function. The tools at hand when numerically solving the shock tube problem is the finite element method (FEM) and computational fluid dynamics (CFD). Some important characteristics regarding both methods will be included. When modeling blast loading of structures, many approaches are available and the ones applied in this thesis will be outlined.

It should be emphasized that most topics presented in this chapter are comprehensive by them self. It is not the intention of this thesis to cover the theory in any detail. However, a brief introduction covering some of the most relevant fundamentals is included for a better understanding of the models and techniques applied.

2.1 Characteristics of a shock wave

An explosion is defined by a sudden increase of energy, resulting in expansion of a fluid from a defined source. The release of energy creates a rapid increase in pressure, density, and temperature, propagating through the undisturbed fluid at supersonic velocity. Explosions may be categorized by the cause of the explosion such as nuclear, chemical and mechanical explosions [1]. Only the two last mentioned types will be presented in this section.

2.1.1 Chemical explosions

A chemical explosion is created when detonation traditional explosives such as TNT and C4. The chemical explosion is initiated by a wave of rapid combustion/reaction of the explosive material moving outwards from the center at a supersonic velocity. This wave may transfer the explosive material into a hot and compressed fluid at a very high pressure. The rapid increase in pressure creates a shock wave in the air[2]. In relation to terror attacks, this is probably the most important type of explosion.

2.1.2 Mechanical explosions

A mechanical explosion is purely caused by the rupture of a solid structure. An example could be a tank containing a compressed fluid with high pressure. If this tank were to rupture, a rapid release of the fluid within results in a wave of high pressure and density propagating outward from the tank. The latter example could have been the result of an industrial accident, but mechanical explosions can also be initiated in a controlled manner as it is done in the SSTF.

2.1.3 Shock wave

A shock wave represents a sudden change in pressure, density and temperature propagating outward from the source with a velocity higher than the speed of sound in the fluid itself. The moving disturbance is referred to as the shock front and typically has a thickness in the order of 10^{-7} m [3]. The mechanism that allows for the wave to propagate is the disequilibrium between the compressed high-pressurized fluid in the shock front and the undisturbed neighboring fluid. The pressure and density of the shock wave are decreasing as the wave propagates, typically in a cubic manner due to the spherical expansion of the shock front.

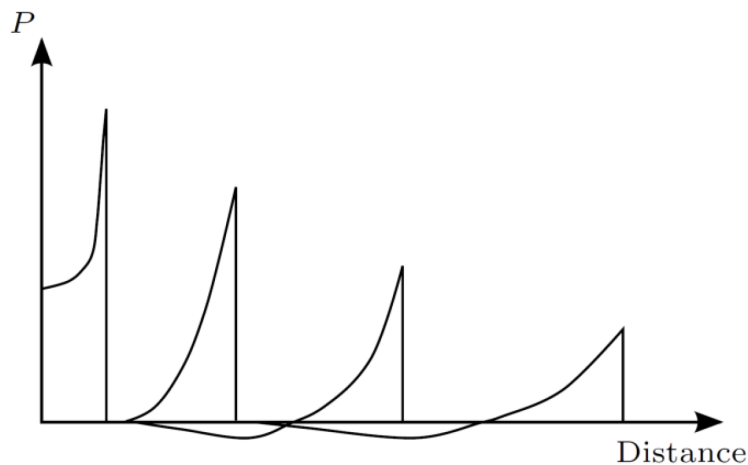


Figure 2.1: Showing the decrease of pressure in the shock front with respect to distance from source. Image is taken from[3]

Two surface orientations are especially important for bodies interacting with the shock wave. Surfaces parallel to the propagation direction experience side-on pressure. Surfaces perpendicularly facing the incoming shock wave experience head-on pressure. This is illustrated in Figure 2.2.

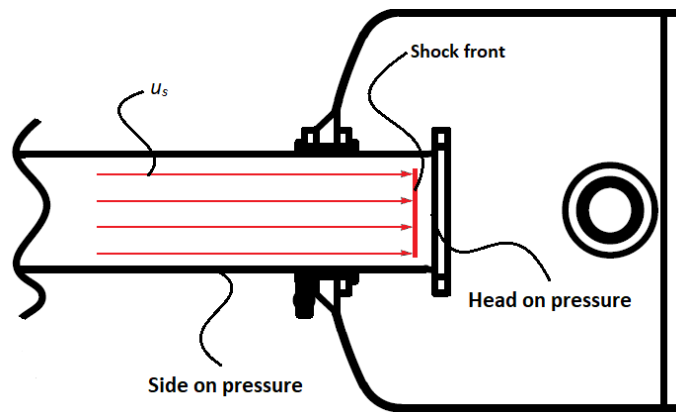


Figure 2.2: Illustration of a shock wave propagating down the shock tube, towards the testing plate. The figure is inspired by [3]

When the shock wave interacts with angled surfaces with respect to the propagation direction, the pressure is being reflected and reinforced. If assuming an ideal linear elastic behavior, which means that the pressure and the density of the fluid are linearly dependent, the result is a reflected head-on pressure twice the incoming side-on pressure. However, in the nonlinear case, the reflected pressure is significantly higher. This is due to the accumulation of fluid particles. The particles are prevented from bouncing back from the surface because of the stream of new particles arriving at the plate, which bring the pressure-density relation in the fluid into the non-linear domain.

2.2 Basic shock tube design and function

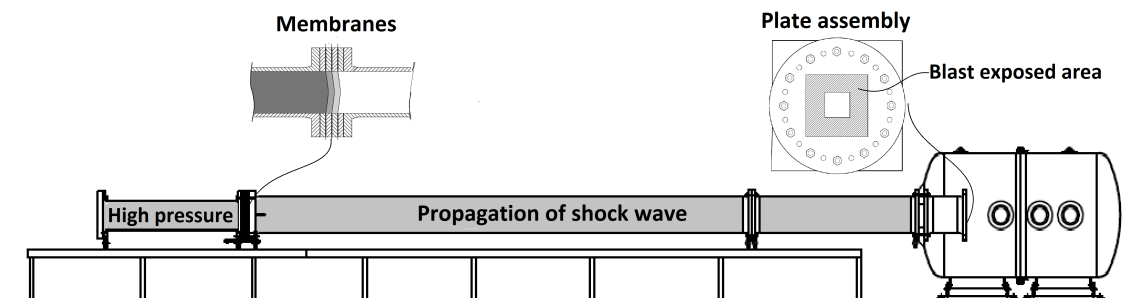


Figure 2.3: Schematic illustration of the basic shock tube design. Figure inspired by [3].

The basic shock tube design is illustrated in Figure 2.3. The illustration shows how the shock tube consists of a high-pressure chamber, referred to as the driver and a section where the shock wave can propagate, referred to as the driven. Separating the two sections is a set of membranes, and the blast-exposed plate is mounted downstream the end of the tube.

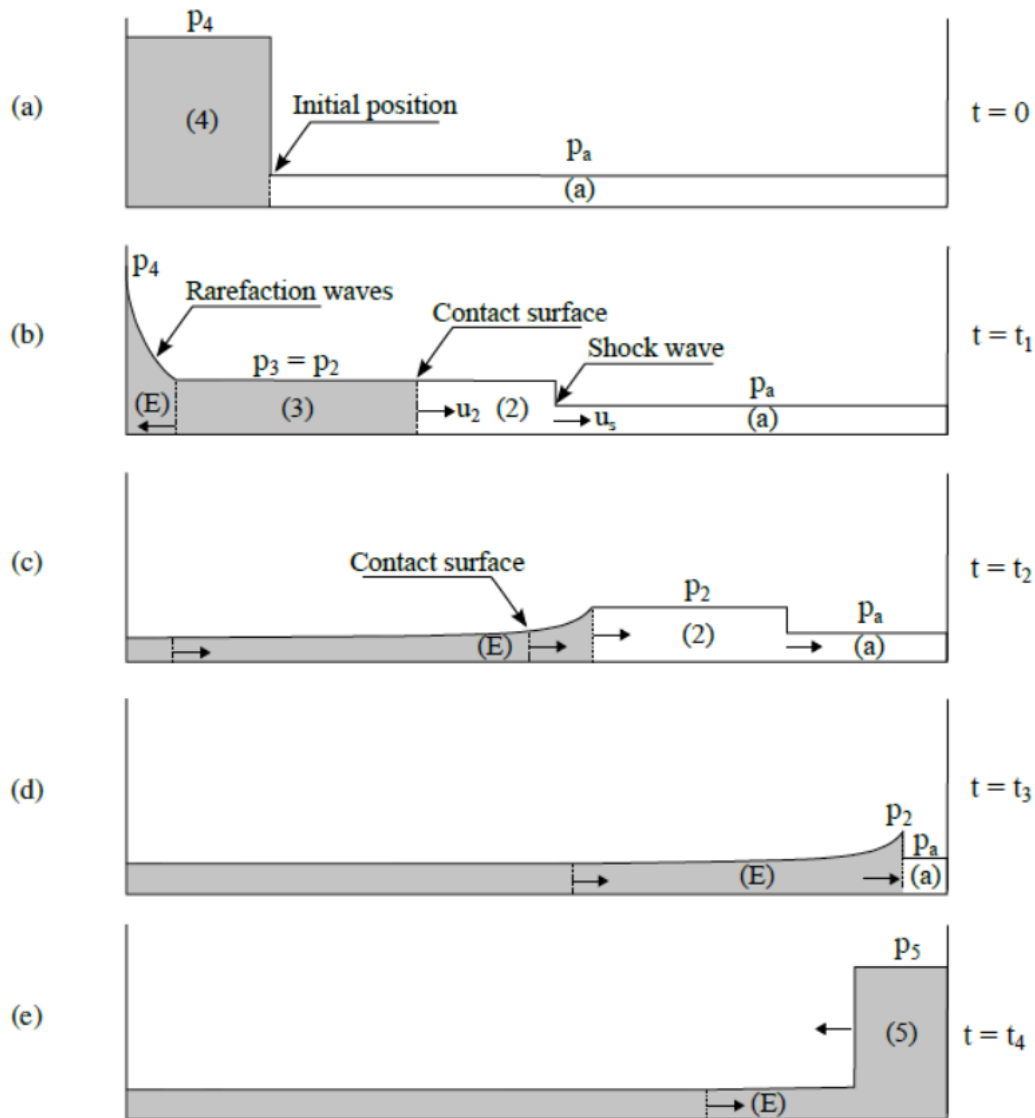


Figure 2.4: A schematic illustration of the idealized shock tube function. The illustration show how the pressure is distributed in the tube at different times: (a) initial configuration, (b) wave pattern immediately after bursting of membranes, (c) reflected rarefaction waves catch up with contact surface, (d) reflected rarefaction waves catch up with the shock wave, and (e) reflection of incoming shock wave when hitting the boundary. The figure is taken from [4].

When describing the function of the shock tube, it is important to keep in mind that this is an idealized shock tube behavior. It is assumed that the problem can be viewed as a 1D problem, that the rupture of the membranes results in an instantaneous release of pressure, that the air can be described as an ideal gas, and lastly the absence of any dissipation phenomenon.

With reference to Figure 2.4, the function can be described as follows [4]. Situation (a)

shows the initial configuration with a high pressure in the driver section and ambient pressure in the driven section, separated by the membranes. At $t=0$, the membranes rupture which generates a shock wave that propagates into the undisturbed air with ambient pressure p_1 . At the same time as the shock wave starts to propagate into the undisturbed air in region (1), rarefaction waves start to propagate in the opposite direction through the highly compressed air in the driven section (4). Immediately after the propagation has initiated, the situation is as illustrated in (b). The speed of the shock wave is supersonic and is denoted v_s . The shock wave induces motion in the air particles which moves with velocity v_2 and pressure p_2 immediately behind the shock front. The moving surface of particles is denoted as the contact surface. At this point, a system of refraction waves moves towards the end of the driver, denoted E. The velocity of these waves is higher than the velocity of the propagating shock front, and the speed is higher because they propagate in the air with higher density than the shock front. Dependent on the design of the shock tube, the refraction waves may catch up with the shock front before it reaches the test object. This causes the shock to decay in strength, increase in duration, and decrease its velocity but results in a pressure profile that is similar to what is found for a far field explosive detonation. When the shock front hits the mounting plate at the end of the tube, the pressure is reflected and reinforced.

2.3 Lagrangian and Eulerian description

In continuum mechanics, there are two common ways of describing a continuum undergoing deformations. These two are often referred to as the Eulerian and the Lagrangian description [5]. Since this is related to the numerical methods; explicit FEM and CFD, it is implied that the continuum is discretized into elements or computational cells.

In the Lagrangian description, each element of the mesh is used to represent a volume of the continuum. The same amount of mass remains associated with each element throughout the simulation, and the mesh deforms with the deformation of the continuum.

In the Eulerian description, the properties of the continuum are evaluated as functions of time and space, measured relative to a global reference frame. The mesh remains fixed, and the continuum moves through the mesh as it undergoes deformation.

It should be noted that it is also possible to combine these two approaches in what is called an arbitrary Lagrangian-Eulerian description, but this is not applied in the numerical work in this thesis.

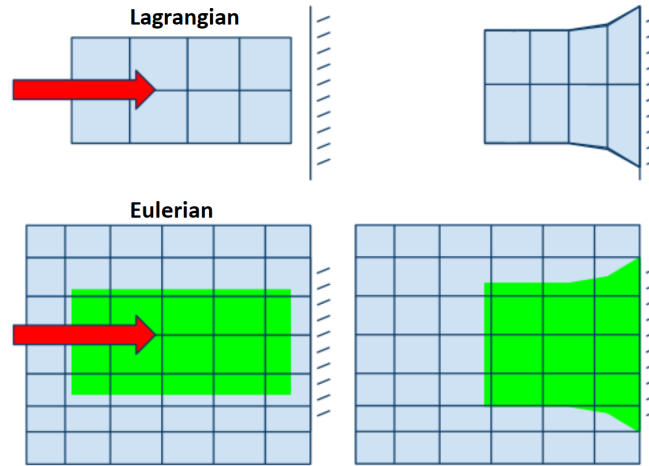


Figure 2.5: Lagrangian and Eulerian discretization of a continuum undergoing deformation. Figure taken from [6].

2.4 Explicit finite element methods

Explicit finite element method is based on the principle of virtual power (PVP) and solves the weak form of this equation for the discretized geometry, using a Lagrangian description[7]. The method is suited for highly nonlinear problems because the iterations are done explicitly in time, and do not take into account any equilibrium iterations. In contrast to the implicit approach, this removes the problem with convergence when encountering bifurcation in the solution. Although the method always produces an answer, solutions can be prone to energy imbalance, and the analysis may require very small time steps. Because small time steps often result in a huge amount of iterations, numerical round-off error can be severe if the total time in the simulation is large. This makes the method suitable for transient dynamic problems. If applied to quasi-static problems, mass scaling is a well known numerical maneuver to overcome the problem with small time steps.

The PVP states that for a solid body in dynamic equilibrium, the virtual power of the internal forces, the inertia forces and the virtual power of external forces are balanced. Using matrix notation this can alternatively be formulated as

$$\underbrace{\int_V \delta \dot{\boldsymbol{\varepsilon}}^T \boldsymbol{\sigma} dV}_{\text{VP internal forces}} + \underbrace{\int_V \delta \mathbf{v}^T (\rho \mathbf{a}) dV}_{\text{VP inertia forces}} = \underbrace{\int_V \delta \mathbf{v}^T \mathbf{b} dV}_{\text{VP body forces}} + \underbrace{\int_{S_t} \delta \mathbf{v}^T \bar{\mathbf{t}} dS}_{\text{VP surface forces}} \quad (2.1)$$

Here $\boldsymbol{\sigma}$ and $\boldsymbol{\varepsilon}$ represent the six independent components of the stress and strain tensors σ_{ij} and ε_{ij} respectively. The volume of the body is notated as V , $\bar{\mathbf{t}}$ is the prescribed traction vector on the surface S_t . Further \mathbf{u} , \mathbf{v} and \mathbf{a} represent the displacement, the velocity and the acceleration vectors. The δ symbol states the virtual quantities, meaning that they are considered infinitesimal and arbitrary, but still satisfy the compatibility conditions.

To arrive at the finite element formulation, the kinematic fields are interpolated over the entire body as:

$$\begin{aligned}\mathbf{u} &= \mathbf{N}\mathbf{r}, \quad \mathbf{v} = \mathbf{N}\dot{\mathbf{r}}, \quad \mathbf{a} = \mathbf{N}\ddot{\mathbf{r}} \\ \dot{\boldsymbol{\epsilon}} &= \boldsymbol{\nabla}\mathbf{v} = \boldsymbol{\nabla}\mathbf{N}\dot{\mathbf{r}} = \mathbf{B}\dot{\mathbf{r}}\end{aligned}$$

Here \mathbf{r} , $\dot{\mathbf{r}}$ and $\ddot{\mathbf{r}}$ is the global nodal displacement, velocity and acceleration. \mathbf{N} is the global shape function matrix and $\boldsymbol{\nabla}$ is the gradient operator.

By inserting the interpolated kinematic fields into the principle of virtual power, one arrive at the semi-discrete form of the equation of motions:

$$\mathbf{M}\ddot{\mathbf{r}} = \mathbf{R}^{\text{ext}} - \mathbf{R}^{\text{int}} \quad (2.2)$$

where

$$\begin{aligned}\mathbf{R}^{\text{int}} &= \int_V \mathbf{B}^T \boldsymbol{\sigma} dV, \quad \mathbf{R}^{\text{ext}} = \int_V \mathbf{N}^T \mathbf{b} dV + \int_V \mathbf{N}^T \bar{\mathbf{t}} dS \\ \mathbf{M} &= \int_V \rho \mathbf{N}^T \mathbf{N} dV\end{aligned}$$

It should be noted that here, \mathbf{M} is the consistent mass matrix. In explicit FEM it is most common to use the lumped mass matrix, as this makes the inversion trivial. This derivation is based on work done in [8].

2.4.1 Mass scaling

The semi-discrete equations of motion are solved in time by using the explicit central difference integration scheme. To find a stable solution, one has to take into account the maximum stable time increment. Based on the solution of the longitudinal wave equation for an elastic material, it is found that the 1D wave speed is

$$c = \sqrt{\frac{E}{\rho}} \quad (2.3)$$

where E is the linear stiffness and ρ is the density of the material. If the time step is larger than the time it takes for a wave to pass the smallest element in the simulation, this could cause disruptions in the solution. Because of this, the upper boundary of the time step is governed by

$$\Delta t \leq \alpha \min \left(\frac{h_e}{c} \right) \quad (2.4)$$

Where h_e is the characteristic length of the smallest element and according to [9] typical values of α are in the range [0.8,0.98]. The upper bond of the time step can as seen in Eq.(2.4) be manipulated by applying large elements or artificially increase the

density of the material. In many cases, applying large elements is not an option, and mass scaling is a well-known maneuver for quasi-static analysis. Local mass scaling can be applied to dynamic models as well, and is normal in the automotive industry. If applied, caution must be taken so that the change in mass does not affect the dynamics of the problem.

2.4.2 Energy considerations

It is important to note that the threshold found with Eq.(2.4) only assure stability for the solution of the central difference scheme in the linear domain. When the response is highly non-linear the criterion is necessary but not sufficient. It is normal to apply elements with reduced integration schemes and to include different contact formulations. Many element formulations introduce the need for some artificial stiffness to reduce spurious deformation modes, and this stiffness gives rise to artificial energy. An example would be elements using reduced integration. Reducing the number of integration points may introduce zero-energy modes or deformation modes without any stiffness. These modes are commonly known as hourglass modes, and they need to be restrained. When modeling contact, it often introduces the need for contact stiffness, and this gives rise to contact energy. Because the first law of thermodynamics applies to the system, it is therefore important to consider the energy balance when running FEM simulations. In addition, it is important to check how large the contribution from artificial- and contact energy is for the total energy in the model. Abaqus suggests an amount of artificial energy less than 2% of the internal energy[10], while LS-DYNA suggests less than 10% as a rule of thumb [11].

2.4.3 Element erosion

To be able to model material fracture, two possible methods are elements erosion or splitting the mesh through nodes splitting [12]. The first approach is the most commonly implemented technique as finding a criterion for where to split the mesh is challenging. In both Abaqus and Europlexus the erosion technique is available.

In both solvers, the method is based on estimating the damage in each integration point, and to do this one need a damage criterion. The applied criterion in this thesis is the Cockcroft-Latham damage criteria and are thoroughly described in the chapter on material modeling. When the damage criteria are satisfied in an integration point, the stress tensor in this point is set to zero and the element is removed when failure is obtained in all points.

2.4.4 Adaptive mesh refinement

Damage and crack-propagation are generally very localized phenomena. It is evident that a satisfactory fine mesh is required to capture these effects when running simulations using FE codes. However, a finer mesh introduces more elements and is increasing the computational costs. Damage-based adaptive mesh refinement (AMR)

is a way of refining the mesh locally where it is needed while keeping the total number of elements to a minimum. For the models run using Europlexus, this feature has been applied. Through a parametric study for the refinement algorithm, performed by Aune et al. [13], the method was found to be very effective as long as the refinement is being carried out in an early stage of the local damage accumulation. It is important to note that the refinement can be related to any monitored parameter for the simulation, and not only the damage parameter as in this study.

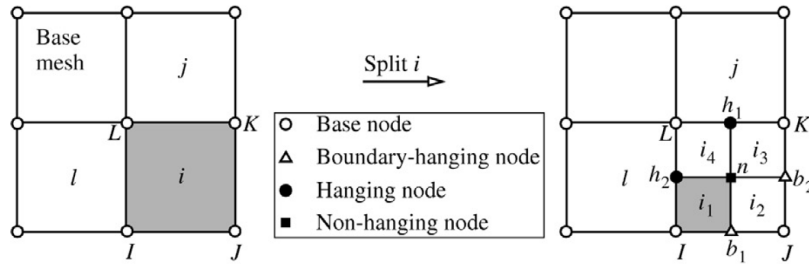


Figure 2.6: Showing one level of mesh refinement. The figure is taken from [13]

As seen for a shell element in Figure 2.6, the method is to split elements that satisfy the threshold damage into four elements for every cycle of refinement. This creates hanging nodes at internal element boundaries (h_1 and h_2). The movement of these nodes is constrained by the movement of the two neighboring base nodes through a link condition[14]. The hanging boundary nodes (b_1 and b_2) are automatically adopting the prescribed boundary condition for the rest of the boundary they are placed on. Further, the algorithm is programmed to erode refined elements when they reach the critical damage level. By going through a refinement process before eroding the elements, the resulting loss of mass from the erosion is reduced compared to eroding unrefined elements.

2.4.5 Contact formulations

To handle contact in numerical models, one needs both a tracking algorithm and a constraint formulation. The tracking algorithm handles the geometries that are interacting, and the constraint equation is the formulation that prevents geometries from non-physical penetration. When modeling solid to solid contact in a finite element analysis, several tracking algorithms and constraint criteria are generally available. However in an explicit analysis, the two most commonly applied constraint criteria are the penalty and the augmented Lagrangian method, but only the penalty method will be described in detail.

Abaqus

All models in Abaqus will apply the weighted penalty method, which is a modified version of the standard penalty method. In the standard method, the two contacting

surfaces are assigned a master and a slave role. The master role is assigned to the surface with the most coarse mesh.

For every iteration, a search algorithm finds slave surface nodes penetrating the defined master surface in the current configuration. As general contact is applied in all simulations[15], the default search algorithm is used. To resist the penetration, forces proportional to the penetration distance is applied to the penetrating slave nodes and opposite and equally large forces are applied to the surface points in the master surface where the penetration occurred. This force is further distributed in the nodes at the master surface.

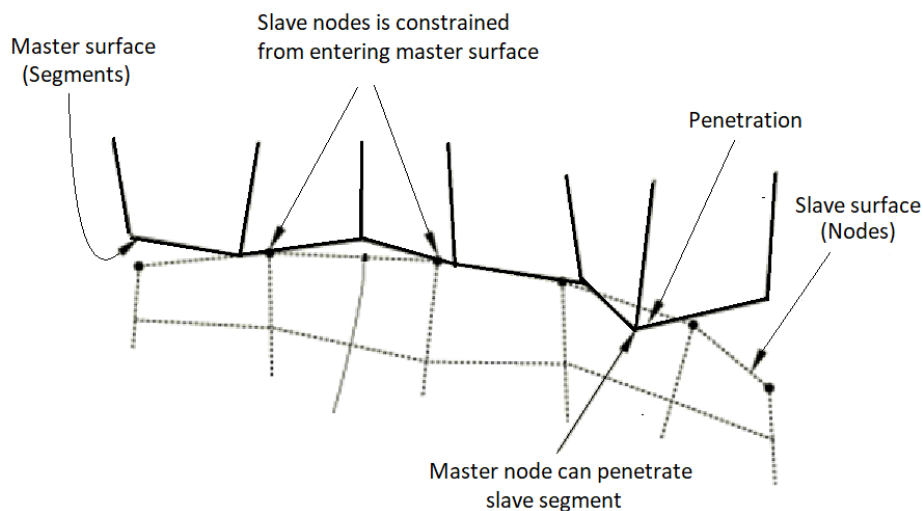


Figure 2.7: Illustrating the Master defined as a continuous surface, and the slave being discretized as nodal points through Abaqus general contact. Image is inspired by [15]

The standard penalty method does not take into consideration master surface nodes penetrating the slave surface. The weighted penalty method accounts for this by running two contact iterations, and alternate the master/slave role of the two surfaces. After calculating the two sets of nodal forces the average nodal force of the two situations is applied to the contacting surfaces.

Europlexus

Europlexus has allow a description of the constraint equation through both Lagrange multipliers and the penalty method[16]. For all models in this thesis, the standard penalty method, combined with the pinball method for tracking of interacting geometries is applied[17]. This is a method specially developed to handle contact in the case of complex geometries, such as a bullet penetrating a plate. It should be noted that this contact formulation is not ideal when modeling sliding contact between parallel surfaces. The basic principle is as follows:

The assembled surface normal algorithm by Belytschko and Lin[18] creates a normal to the outside surfaces. The surface elements are then assigned a pinball radius, and contact is detected if the distance between two pinballs is less than the sum of the two associated radiuses.

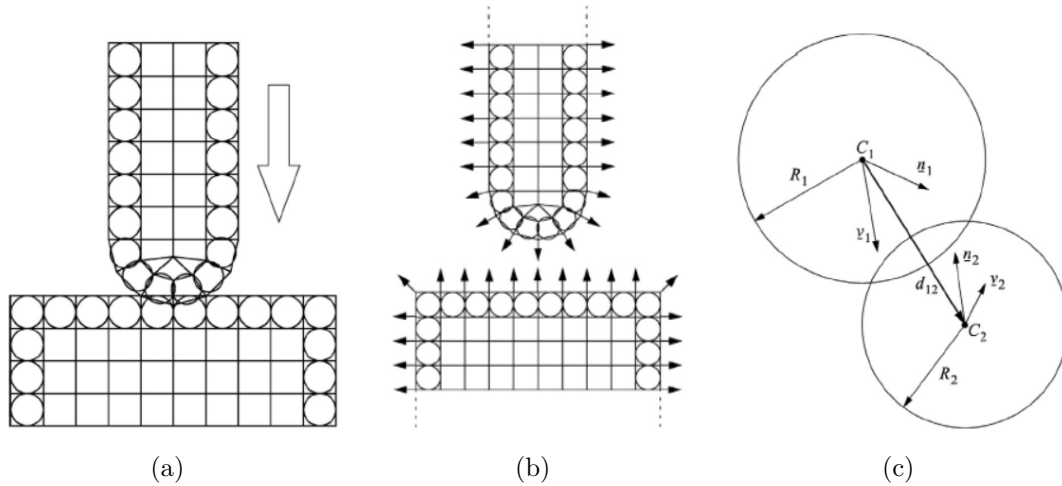


Figure 2.8: (a) Illustration of a incoming projectile interacting with surface. (b) Showing how the normal to the surfaces are oriented. (c) Illustration of two pinball spheres interacting. Images are taken from [19]

Friction

In both solvers, the simple Coulomb friction model is applied[20]. Both the static and the dynamic frictional coefficient is set to be equal. The Coulomb model assumes that the static and dynamic frictional force only depends on the frictional coefficient, normal force, and direction of slippage.

2.5 Computational fluid dynamics

Computational fluid dynamics (CFD) is a way to numerically describe problems related to fluid flows. CFD is a huge field consisting of complex theories extending way outside the scope of this study.

2.5.1 Conservation laws in fluid dynamics

The governing equations in fluid dynamics, and also the foundation for a CFD analysis are the conservation of mass, conservation of momentum and lastly conservation of energy. In contrast to what is normally done in solid mechanics, these conservation laws are most commonly described through an Eulerian description.

Conservation of mass

The conservation of mass can be expressed in differential form as

$$\frac{\partial \rho}{\partial t} + \nabla \cdot (\rho \mathbf{v}) = 0 \quad (2.5)$$

Where ρ represents the density of the fluid and \mathbf{v} is the velocity. In words, the equation states that for the mass to be conserved, the change of density with respect to time plus the mass flow divergence has to be equal to zero. If considering a control volume, this means that the difference in mass flow in and out has to be equal to the change in density.

Conservation of Momentum

Conservation of momentum implies that for a fluid particle, the sum of internal and external forces has to be equal to the mass times the acceleration. For a continuum, this statement yields

$$\rho \mathbf{a} = \mathbf{f}_{\text{body}} + \mathbf{f}_{\text{surface}} \quad (2.6)$$

Where \mathbf{f}_{body} are forces applied to the entire mass of the continuum, and $\mathbf{f}_{\text{surface}}$ are the forces acting on the surface of the evaluated continuum element. By replacing the acceleration with the material derivative of the velocity field for the fluid, and expressing the surface forces through the divergence of the Cauchy stress tensor, Eq. (2.6) may be rewritten as

$$\frac{D(\rho \mathbf{v})}{Dt} = \nabla \cdot \boldsymbol{\sigma} + \mathbf{f}_{\text{body}} \quad (2.7)$$

where the material derivative for a scalar field (ϕ) and for a vector field (\mathbf{v}) is defined by

$$\frac{D\mathbf{v}}{Dt} = \frac{\partial \mathbf{v}}{\partial t} + \mathbf{v} \cdot \nabla \mathbf{v} \quad (2.8)$$

$$\frac{D\phi}{Dt} = \frac{\partial \phi}{\partial t} + \mathbf{v} \cdot \nabla \phi \quad (2.9)$$

The Cauchy stress $\boldsymbol{\sigma}$ may further be decomposed into a hydrostatic and a deviatoric part through the relation

$$\boldsymbol{\sigma} = -p\mathbf{I} + \boldsymbol{\tau} \quad \text{where} \quad p = -\frac{1}{3}\text{tr}(\boldsymbol{\sigma}) \quad (2.10)$$

By inserting the relation obtained in Eq. (2.10) back into Eq. (2.7), we end up with

$$\frac{\partial(\rho \mathbf{v})}{\partial t} + \mathbf{v} \cdot \nabla(\rho \mathbf{v}) = -\nabla p + \nabla \cdot \boldsymbol{\tau} + \rho \mathbf{f}_{\text{body}} \quad (2.11)$$

Now a constitutive relation for the continuum has to be chosen in order to further rewrite the expression for conservation of the momentum. By assuming a Newtonian viscous fluid, the following relations may be applied for the deviatoric stress in the fluid

$$\boldsymbol{\tau} = 2\mu\mathbf{D}' \quad \text{where} \quad \mathbf{D}' = \mathbf{D} - \frac{1}{3}\text{tr}(\mathbf{D}) \quad (2.12)$$

Where μ is the viscosity and \mathbf{D} is defined as the symmetric rate of deformation tensor given by

$$\mathbf{D} = \frac{1}{2}(\nabla\mathbf{v} + (\nabla\mathbf{v})^T) \quad (2.13)$$

By putting Eq. (2.13) and (2.12) back into Eq. (2.11), and setting the body forces equal to the gravitational forces, we end up with the general Navier-Stokes equation for a compressible Newtonian viscous fluid

$$\frac{\partial(\rho\mathbf{v})}{\partial t} + \mathbf{v} \cdot \nabla(\rho\mathbf{v}) = -\nabla p + \mu\nabla^2\mathbf{v} + \frac{1}{3}\mu\nabla(\nabla \cdot \mathbf{v}) + \rho\mathbf{g} \quad (2.14)$$

To sum up, the left-hand side of Eq. (2.14) represents the mass times the acceleration, and the right-hand side represents the sum of all acting forces. The second term on the right-hand side is related to frictional forces, while the third term is describing the compressibility of the fluid. The equation applies for an infinitesimal fluid particle. The relevant theory for this derivation was found in [21] [22].

Conservation of Energy

Lastly, the conservation of energy has to be evaluated. This relation states that for an isolated system, the rate of change in total energy has to be equal to the sum of net heat flux through the system, and the work done by internal forces and body forces on the system, i.e.

$$\frac{DE}{Dt} = \nabla(\boldsymbol{\sigma}\mathbf{v} - \mathbf{q}) + \rho(\mathbf{f}_{\text{body}} \cdot \mathbf{v}) \quad (2.15)$$

where E is the total energy and is defined by

$$E = \frac{1}{2}\rho(\mathbf{v} \cdot \mathbf{v}) + \rho e = E_{\text{kinetic}} + E_{\text{internal}} \quad (2.16)$$

$\boldsymbol{\sigma}$ is again the Cauchy stress tensor. When evaluating an infinitesimal fluid element, these stresses may be referred to as the traction stresses or forces at the boundaries of the cubic element.

2.5.2 Equation of state

The conservation laws described in section 2.5.1 generally contain more unknowns than equations, and an additional relation is required to solve for all state variables. A thermodynamic equation of state (EOS) serves as a constitutive relation between a set of given state variables and physical conditions, i.e., to relate the density to pressure and temperature. The specific equation of state applied in this study is presented in section 3.2

2.5.3 Discretization of the flow regime

In a CFD analysis, the solution domain for the fluid is being discretized into a finite number of elements prior to the calculations, and several discretization methods are available. The most common methods are

- The Finite Volume Method (FVM)
- The Finite Element Method (FEM)
- The Finite Difference Method (FDM)

The FVM is the one applied for the numerical work in this thesis, and only this approach will be described in any detail.

When discretizing the fluid regime into finite volumes the conservation laws are applied to each discrete volume element, and hence, conservation of flux through each volume will be satisfied through the use of so-called Riemann Solvers [23]. The FV formulation is generally preferred when modeling problems with possible discontinuities in the solution and high Reynolds numbers, meaning high inertial forces relative to the viscous forces of the fluid.

2.6 Modeling of blast-loaded structures

As stated, the modeling of blast-loaded structures generally involves an interaction between both a solid and a fluid sub-domain. As this is considered a complex and also computationally costly issue to solve, different simplified modeling techniques may be applied depending on the problem. Generally, there are three different approaches; A pure Lagrangian approach, the uncoupled Euler-Lagrange (UEL), and lastly the fully coupled Euler-Lagrange (CEL) approach. For this thesis, only the pure Lagrangian and the fully coupled Euler-Lagrangian methods have been applied.

2.6.1 The Lagrangian approach

The idea behind the pure Lagrangian approach is to run the simulation as a structural FEM analysis, with a predefined loading. The estimation of the load and the response

of the structure is being considered completely separate. The load is applied to the structure as a pressure-time curve and a common approach is to represent the blast load through the Friedlander equation. This method is used in Chapter 4 and 5, and also for most of the models described in Chapter 7.

Friedlander curve fit

Based on estimating some key-parameters for the blast wave, the Friedlander method aims to describe the pressure experienced by the structure as a function of time [24]. The most straightforward way of doing this is through a curve fit on actual pressure measurements taken from experiments, which is the applied method in this thesis. Alternatively, it is common to find the parameters for the Friedlander curve by applying the semi-empirical approach derived by Kingery and Bulmash[25]. This method is based on extensive experimental work, including different scaled blast scenarios. The Kingery and Bulmash method accounts for the weight of the explosive and the distance from the source.

$$P(t) = P_a + P_r \left(1 - \frac{t}{t_+}\right) \exp\left(\frac{-bt}{t_+}\right) \quad (2.17)$$

Where t_+ is the positive time duration, t is the total time, P_r is the reflected pressure, P_a the atmospheric pressure and b is the exponential decay coefficient.

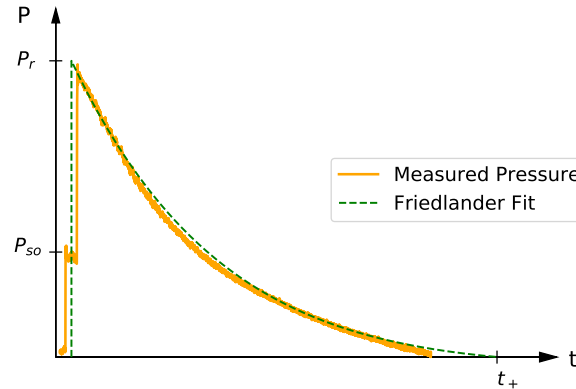


Figure 2.9: Plot showing measured pressure and the corresponding Friedlander fit, when only considering the positive phase of the pressure-time history.

In Figure 2.9 the pressure measured at a sensor close to the structure has been fitted to Eq. (2.17) for the positive phase of the event ($t < t_+$). The result is an analytic expression for the pressure-time relation experienced by the structure.

2.6.2 Euler-Lagrange methods

The main idea of a Euler-Lagrange approach is to separately describe the structure through a Lagrangian description, and the fluid sub-domain through a Eulerian (CFD) description. Now the Eulerian description of the shock propagation serves as a numerical prediction of the blast load experienced by the structure. At this point, there are two separate ways to go, i.e., the uncoupled and the coupled approach. For the uncoupled method the fluid and structure sub-domains are treated separately, and they are not allowed to interact. For the coupled methods, both the structural Lagrangian description and the Eulerian fluid description are put together in the same analysis. Here the two domains are allowed to interact, and the structural part will serve as a deformable boundary condition for the fluid sub-domain.

2.6.3 Loading regimes

In structural dynamics, the duration of a loading is often related to the response time, or natural frequency of the structure. By doing this, the loading may be classified into one out of three possible loading-regimes; an impulsive loading, a dynamic loading or a quasi-static loading. If the applied load has a duration significantly longer than the response time of the structure, meaning that the structure has reached its maximum deflection before the load has dissipated markedly, the load is said to be quasi-static. In this regime, the response is governed by the stiffness of the structure K and the maximum applied load, P_{\max} through the static equilibrium equation.

The loading is often categorized as quasi-static as long as the following inequality holds

$$\omega_n t_d > 40 \tag{2.18}$$

Where the ω_n is the natural frequency of the structure and t_d is the duration of the applied loading.

On the other hand, if the duration of the applied load is much shorter than the response time, meaning that the loading has been both applied and removed before the structure has experienced any significant displacements, the load is classified as impulsive. The resulting maximum displacement is now dependent on the impulse from the load, as conservation of momentum is the governing equation. The response is defined as being in the impulsive domain as long as the following inequality holds

$$\omega_n t_d < 0.4 \tag{2.19}$$

The dynamic regime is defined as the region in-between the impulsive and quasi-static regime, i.e. ($0.4 < \omega_n t_d < 40$). The displacements within this regime are dependent on the loading history and the behavior is far more complex to describe. Further derivations of the above criterion can be found in [1].

2.6.4 Fluid-structure interaction algorithms in Europlexus

There are several algorithms available when it comes to how to solve the mutual interaction between the solid and the fluid. The method applied in upcoming simulations will be a method often referred to as the embedded approach. This is the only approach that will be described in any detail. Aune[3] thoroughly describes and evaluates several methods in his Ph.D. thesis.

The main idea behind the embedded approach is to implement the interaction in a way that makes the fluid and the solid mesh independent of each other. This has significant advantages when it comes to modeling large deformation and failure in the plates, as many of the other methods encounter problems in these highly nonlinear cases. ALE methods where the fluid mesh is fitted to the structure imply that the fluid mesh need to deform with the structure, making the solution prone to distorted fluid elements and possibly introducing the need for re-meshing algorithms.

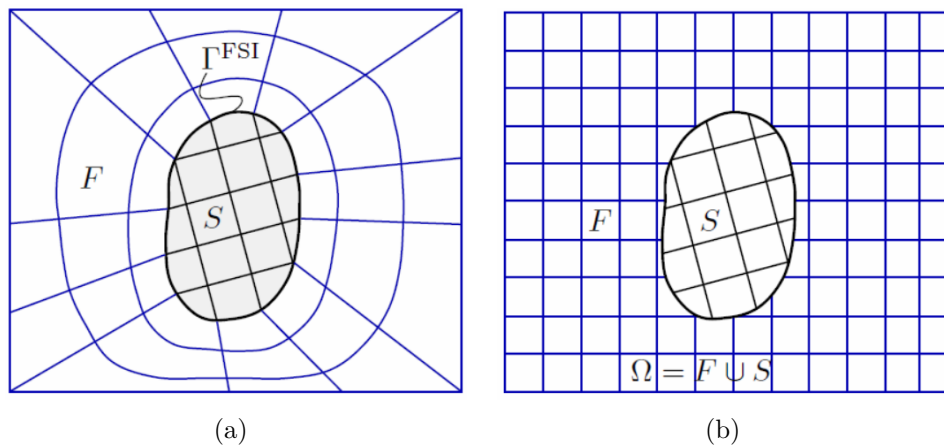


Figure 2.10: Illustrating mesh dependency in FSI techniques. Both images are taken from [3](a) Illustration of FSI techniques where the fluid mesh is fitted to the solid mesh is using ALE. (b) Illustration of the embedded approach. For this technique the two meshes are completely independent.

When using the embedded approach, the Lagrangian solid mesh is immersed in the Eulerian fluid mesh, but the two meshes are independent of each other. Because the meshes are independent, the embedded approach needs a tracking algorithm that searches for solid and fluid elements that are supposed to interact. This is done by the definition of an influence domain and is applied as a spherical influence radius around all surface nodes on the discretized solid structure. These spheres are further joined to cover the entire solid structure. It should be noted that choosing the influence domain can be challenging. A too small influence domain may introduce spurious flux across the solid structure, whereas a too big influence domain will link too much of the fluid to the motion of the structure.

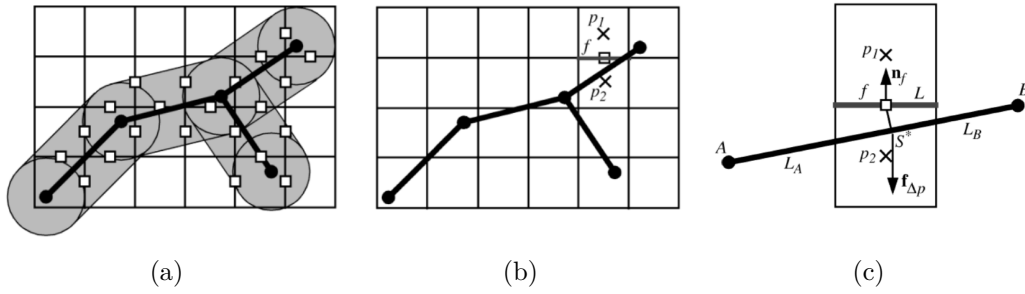


Figure 2.11: Illustrating a FSI algorithm in Europlexus[26](a) Illustration of the influence domain around the solid structure. (b) Calculating the pressure drop force that is imposed on the structure. (c) Detailed image of the coupling

Instead of imposing certain conditions on the particle velocities, the pressure force is calculated in the fluid mesh and transmitted to the structure. This is illustrated in Figure 2.11(b). With reference to this figure, the two volumes V_1 and V_2 , with pressures p_1 and p_2 are separated by the coupled face f . The pressure drop force is then calculated as

$$\mathbf{f}_{\Delta p} = (p_1 - p_2)L\mathbf{n}_f \quad (2.20)$$

Where L is the length/area of the face and \mathbf{n}_f is the face normal. The force is distributed from what is marked as point S^* in Figure 2.11(c) to the neighboring nodes at the structure. To prevent leakage, the flux of mass and energy is set to zero across the fluid elements that are separated by the structural element.

It should be noted that although this FSI formulation is robust when handling large deformations and potential failure, it can run into trouble if the fluid mesh is coarse relative to the shape of the deformed plate.

2.7 Previous work

Råkvåg et al.[27] investigated the effect of different pre-cut defects in thin square Docol 600 DL steel plates subjected to rapid pressure loading. The defect shapes tested was square, diamond, slit and circular. The plates had four symmetrically distributed defects, and the different defect configurations had equal extent. In their experimental work, it was found that the defect-shape and area had a great effect on the maximum deflection of the plates. The main trend observed was that the final deflection of the target plate decreased with an increase in hole area. However, no monotonic relation in hole area and deflection was found. Another result to point out is that none of the plates tested experiences failure during testing. It is important to note that the test rig used in these experiments has a different set up than the shock tube facility at NTNU. The Pulse Pressure Loading Rig (PPLR) consists of two separate chambers. These chambers are being pressurized equally, with the target plate

being the dividing wall. When both chambers have reached their desired pressures, a diaphragm in one of the chambers is melted along the circumference. As a result the pressure is evacuated rapidly, and the plate is loaded due to the disequilibrium between the chambers.

Baglo and Djupvik[28] investigated in their master thesis the effect from blast loading on thin aluminum and steel plates. The tested plates were 0.8 mm thick Docol 600 DL steel plates, and AW-1050A-H14 aluminum plates with thicknesses of 0.8 mm and 2 mm. The tests were conducted in the SSTF. Two of the aluminum plates experienced fracture at the supports, whereas none of the steel plates experienced fracture. In addition to the shock tube testing, tensile test specimens were cut from plates with two different thicknesses for each metal. The specimen orientation relative to the rolling direction of the plates was varied, and it was indicated that thinner plates were more exposed to directional anisotropy. Aluminum plates were more prone to this effect than steel. The FEM software Abaqus was used to model the experiment, and the loading was applied as the pressure time history measured in the experiments. It was concluded that the compliance between the simulations and the tests were satisfying.

Granum and Løken[29] investigated 0.8 mm thick Docol 600 DL steel plates subjected to blast loading. Plates with four square holes symmetrically distributed, reducing the blast-affected area by 16%, and non-perforated plates were tested and compared. The tests were conducted at the SSTF located at NTNU. The most heavily loaded perforated plates experienced collapse by radial fracture, initiating from the corners of the square perforations. The non-perforated plates did not experience fracture. A numerical study of the experimental setup was carried out using Abaqus and several simulation techniques were applied. Simulations using a purely Lagrangian formulation was compared to coupled and uncoupled Eulerian-Lagrangian simulations.

Stensjøen and Thorgeirsson [30] investigated the dynamic response of thin perforated aluminum plates subjected to blast loading both numerically and experimentally. A thorough preliminary numerical study was conducted to study the behavior of the plates and to find the pressure loading to be used in the experiments. Six different configurations with pre-formed defects were tested in this numerical study, one with four squared windows and five different slit setups. The overall performance of the preliminary study was found to be satisfactory when compared to experimental data obtained from tests in the SSTF. However, even after modifying the numerical models to better fit the experimental data, some of the slit configurations proved to be challenging regarding the crack propagation process. The numerical study also showed that solid elements with multiple elements across the thickness were needed in order to get a more detailed description of the failure mechanisms.

Li et al. [31] studied the response of Q345 steel plates with pre-formed holes exposed

to blast loading created by a TNT charge placed at a fixed distance, but with a varying amount of explosives. The pre-formed holes in this study were included to represent the effect of fragments perforating the plate prior to the shock wave. The different hole-shapes studied were circular, squared and diamond. They were all organized in a 3x3 matrix formation. Failure modes and deformation curves were identified experimentally and were later used to verify numerical simulations. The study indicated that the geometry of the holes has a noticeable influence on the overall strength and response to the blast load. For the smallest charges, no obvious difference in the response of plates containing circular and squared holes were found. When the loading was increased, the mid-point deflection also increased in a nonlinear manner. The deviation in response between the plates with squared and circular holes was shown to increase with the increased blast intensity. Due to the fact that fracture occurred in all plates with diamond-shaped holes, the ductile deformation curves was mainly compared for the plates with circular and squared holes.

Aune et al. [13] performed a study on the dynamic response of blast-loaded Docol 600 DL steel plates both numerically and experimentally using the SSTF at NTNU. Both massive and deformable plates with and without pre-formed was tested. The massive plates were used for comparison to evaluate the fluid-structure interaction effects, and to measure the load history for later numerical studies. For the deformable plates, special focus was given to the influence of pre-formed holes on the dynamic response of the plates and the failure characteristics. This study indicated a trend of reduced reflected pressure for plates with pre-formed holes. This study also indicated an increased mid-point deflection for the perforated plates compared to the full plates under similar loading conditions.

Aune[3] contributed with a thorough description of the theory of shock physics, and a description of various modeling techniques including FEM, CFD, and FSI. He also investigated the behavior of both steel and aluminum plates exposed to blast loading in the SSTF.

Aluminum plates made from the alloy EN AW 1050-H14 with thickness 0.8 mm was tested in the SSTF at NTNU by Aune et al.[32]. The purpose was to investigate the effect of FSI and to investigate the capacities of damage-based AMR techniques to predict ductile fracture in the aluminum plates. Several different numerical approaches were investigated, both coupling and uncoupling the fluid-solid behavior. Different boundary conditions were also tested. It was found that the fully coupled simulations were in very good agreement with the experimental results, and it was concluded that including FSI effects in the model was necessary. The damage-based AMR technique was promising in terms of predicting ductile failure in the blast-exposed plates.

Chapter 3

Material models

This chapter will introduce constitutive models for air and the Docol 600DL steel. Some of the previously conducted work regarding the material testing of the Docol steel will also be briefly presented. In later numerical work, constitutive models are needed to model the material behavior and this chapter aims to elaborate these models and their assumptions.

3.1 Docol 600DL steel

The Docol 600DL steel is produced by SAAB in Sweden and is a dual-phase, low-strength, and high-hardening steel developed mainly for the automotive industry. The plate material is processed through cold rolling and it is available in the thicknesses 0.5 mm - 2.1 mm. All plates evaluated in this thesis have a thickness of 0.8 mm. In the description of the constitutive models for the Docol 600DL steel, all derivations are based on the work presented in [33].

3.1.1 Previously conducted material testing

The material behavior of the Docol 600DL steel was studied by Gruben et al.[34][35] on 2 mm thick plates, by Holmen et al.[36] on plates with a thickness of 0.8 mm, and by Rakvåg et al.[37] on plates with a thickness of 0.7 mm. It should be noted that Rakvåg also performed Split-Hopkinson tests. In all studies, it was evaluated how isotropic the material behaved in quasi-static testing. This was carried out by cutting out dog-bone tests specimens from the plates with a known orientation relative to the known cold rolling direction. The dogbone tests specimens had in-plane dimensions as shown in Figure 3.1(a), and was cut out with orientations of 0° , 45° and 90° relative to the rolling direction. The finding from these studies is that the steel, in general, behaves tolerable isotropic and that thinner plates are more anisotropic than thicker plates.

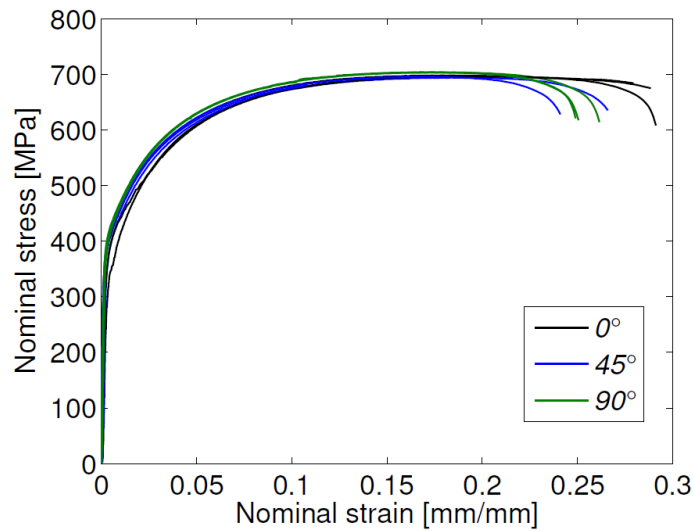
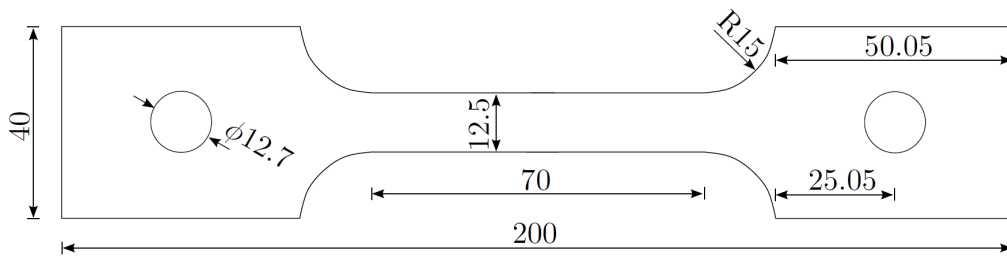


Figure 3.1: Both images are taken from[3], and is showing the test specimen and results from the experiments on the material behavior on Docol 600DL. (a) shows the dimensions of the dog-bone test specimen applied for material tests in [mm] and (b) is showing resulting stress strain curves obtained in[36]

The material data for the Docol 600DL steel applied in this thesis were taken from the PhD thesis written by Aune[3], and is given in Table 3.1.

Table 3.1: Initial material parameters used for the Docol 600DL steel. These material parameters are taken from [3].

| A | Q_1 | C_1 | Q_2 | C_2 | c | m | \dot{p}_0 | W_c |
|-------|-------|-------|-------|-------|------|-----|--------------------|-------|
| [MPa] | [MPa] | [-] | [MPa] | [-] | [-] | [-] | [S^{-1}] | [MPa] |
| 325.7 | 234.5 | 56.2 | 445.7 | 4.7 | 0.01 | 1.0 | 5×10^{-4} | 555.0 |

3.1.2 Model assumptions

The material is expected to act elastic-thermoviscoplastic and to be exposed to large plastic deformations. Strain-rates are expected to be moderate and the steel experience strain- and strain rate hardening as well as temperature softening. Ductile fracture is the expected fracture mechanism.

When modeled, the behavior will be assumed as perfectly isotropic for both the elastic and the plastic domain. The transition from idealized elastic behavior to plastic behavior is assumed to be governed by the Von Mises yield criteria. In the plastic domain, incompressible conditions apply to the plastic deformation, and the plastic flow stress is assumed to be independent of the hydrostatic stress. The total strain is assumed to be an additive combination of a pure elastic strain and a pure plastic strain. To describe hardening and softening of the material, it is assumed that this can be expressed explicitly as a function of strain, strain rate, and temperature.

3.1.3 Elastic behavior

The stress-strain relation for linear elastic materials can be expressed through the Generalized Hooke's Law on the form

$$\sigma_{ij} = C_{ijkl}\varepsilon_{ij} \quad (3.1)$$

Where σ_{ij} contains all nine stress components, ε_{ij} contains all nine strain components and C_{ijkl} is a 4th order tensor of elastic constants.

Further, the material is assumed to behave in an isotropic manner, i.e., the material has the same properties in all directions. This makes it possible to simplify Eq.(3.1) in terms of strains on the form

$$\varepsilon_{ij} = \frac{1 + \nu}{E}\sigma_{ij} - \frac{\nu}{E}\sigma_{kk}\delta_{ij} \quad (3.2)$$

Or in terms of stresses

$$\sigma_{ij} = \lambda\varepsilon_{kk}\delta_{ij} + 2\mu\varepsilon_{ij} \quad (3.3)$$

Where λ and μ are the Lamè elastic constants, related to the Youngs modulus, E , and Poisson's ratio, ν through the relations

$$\mu = \frac{E}{2(1 - \nu)} = G \quad (3.4)$$

$$\lambda = \frac{\nu E}{(1 + \nu)(1 - 2\nu)} \quad (3.5)$$

3.1.4 Yield criteria

In terms of material modeling, the yield criterion is the relation that separates the elastic domain from the plastic domain. The material is said to behave elastically until the yield criterion is satisfied and the behavior enters the plastic domain where a new set of rules are governing the stress-strain relation. The von Mises yield criterion is derived by assuming the material to be isotropic, yielding is independent of hydrostatic pressure, plastic deformations are isochoric, yield behavior is rate independent, and that the loading is quasi-static. The result is a criterion that relates yield to the second invariant of the deviatoric stress tensor, J_2 .

The relation between the stress tensor, the hydrostatic stress tensor, and the deviatoric stress tensor is given by

$$S_{ij} = \sigma_{ij} - \sigma_H \delta_{ij} \quad \text{and} \quad \sigma_H = \frac{1}{3} \sigma_{kk} \quad (3.6)$$

Where S_{ij} represents the deviatoric stress tensor, σ_H is the hydrostatic stress tensor, σ_{ij} is the stress tensor. The second invariant of the deviatoric stress matrix is given by

$$J_2 = \frac{1}{2} S_{ij} S_{ij} \quad (3.7)$$

The von Mises yield criterion states that yield will occur when J_2 reaches a critical value. To derive the expression for the yield function, this value will first have to be determined. This is done by considering the state of uni-axial stress at initial yield. The obtained result is that yield will occur when

$$J_2 = k^2 = \frac{1}{3} \sigma_Y^2 \quad (3.8)$$

Now, the relation between the current stress state and the initial yield of the material has been defined. It is now convenient to rewrite the equation in Eq.(3.8) in terms of a yield function of the current stress state, σ_{ij} . This function should take a value less than zero if the behavior is elastic, and the value zero when yield is initiated.

$$f(\sigma_{ij}) = \varphi(\sigma_{ij}) - \sigma_Y = \sqrt{3J_2} - \sigma_Y = \sqrt{\frac{3}{2} S_{ij} S_{ij}} - \sigma_Y \leq 0 \quad (3.9)$$

3.1.5 Strain hardening and flow stress

To describe strain hardening, the yield function has to be modified in such a way that it can accumulate plastic strains, and adjust the current yield stress accordingly. If the material is being further deformed after initial yield, the strains can now be decomposed into an elastic part and a plastic part.

$$\varepsilon_{ij} = \varepsilon_{ij}^e + \varepsilon_{ij}^p \quad (3.10)$$

Where ε_{ij}^e represents the pure elastic strain tensor and ε_{ij}^p the pure plastic strain tensor. Writing these tensors on increment form gives

$$d\varepsilon_{ij} = d\varepsilon_{ij}^e + d\varepsilon_{ij}^p \quad (3.11)$$

The yield criteria, $f(\sigma_{ij}) = 0$, results in a yield surface for the material. To model strain-hardening, the yield surface must be allowed to expand/move. The material is assumed to behave equally in both tension and compression, hence the isotropic hardening model is assumed.

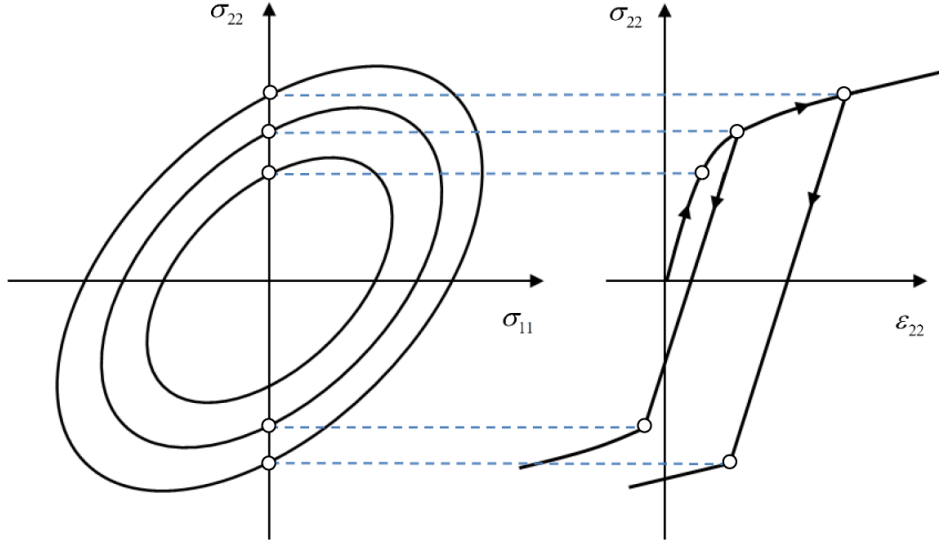


Figure 3.2: Expansion of the yield surface when assuming isotropic hardening. The figure is taken from [33].

The yield function may now be modified to include the work-hardening and allow for the yield surface to expand. This is done by including an isotropic work-hardening parameter to the function on the form

$$f(\sigma_{ij}, R) = \varphi(\sigma_{ij}) - (\sigma_0 + R) \quad \text{and} \quad \sigma_Y = \sigma_0 + R \quad (3.12)$$

Where σ_0 denotes the initial yield stress, σ_Y is the current yield stress and $R = R(p)$ is the isotropic work-hardening variable which is a function of the equivalent plastic strain p . The equivalent plastic strain is given by the formula;

$$p = \int dp \quad \text{and} \quad dp = \sqrt{\frac{2}{3} d\varepsilon_{ij}^p d\varepsilon_{ij}^p} \quad (3.13)$$

The last missing piece is the function $R(p)$, i.e., it has to be decided what hardening rule to apply. Two of the most common hardening rules are the Power Law and the Voce/Extended Voce hardening. In this material model, the extended Voce hardening is chosen and it is given by

$$R(p) = \sum_{i=1}^2 Q_i (1 - e^{-C_i p}) \quad (3.14)$$

Where Q_i and C_i are calibrated constants.

3.1.6 Viscoplasticity

So far, the equivalent stress only depends on the plastic strain. The evaluated material behavior is assumed to be both strain-rate and temperature dependent as well. To account for rate dependency, the yield function is expanded to include the rate dependent stress term σ_v . This result in

$$f(\sigma_{ij}) = \varphi_{ij} - \sigma_{eq} \quad \text{and} \quad \sigma_{eq} = \sigma_0 + R(p) + \sigma_v(\dot{p}) \quad (3.15)$$

Where \dot{p} is the plastic strain rate and σ_v is the rate-dependent work-hardening. By applying the Norton creep law, the viscous stress can be expressed as

$$\sigma_v = (\sigma_0 + R) \left[\left(1 + \frac{\dot{p}}{\dot{p}_0} \right)^c - 1 \right] \quad (3.16)$$

Where \dot{p}_0 is a pre-defined reference strain rate, and c is a material-specific constant related to the strain-rate sensitivity that will have to be determined through a calibration process. The equivalent stress, σ_{eq} , may now be rewritten as [8]

$$\sigma_{eq} = (\sigma_0 + R) \left(1 + \frac{\dot{p}}{\dot{p}_0} \right)^c \quad (3.17)$$

It is important to note that this modification allows the stress to move outside the yield surface, i.e. the yield function f may now take values greater than zero. This result in new boundaries for elastic-plastic behavior

$$\begin{aligned} f &\leq 0 && \text{elastic} \\ f &> 0 && \text{plastic} \end{aligned}$$

3.1.7 Thermal softening

When steel is subjected to rapid plastic deformation, heat is generated. This heating process is assumed to be adiabatic, and high temperatures generally have a softening effect on both the elastic stiffness, E , and the plastic behavior for most metals. In

this material model, the effect on and from the elastic behavior will be neglected, resulting in the following differential equation

$$dT = \frac{\beta_{TQ}}{\rho c_\varepsilon} dW_p = \frac{\beta_{TQ}}{\rho c_\varepsilon} \sigma_{eq} dp \quad (3.18)$$

Where dT is an incremental temperature change, ρ is the density of the material, c_ε is the specific heat capacity, dW_p is the incremental plastic work per unit volume and β_{TQ} is the Taylor-Quinney coefficient. The latter determines the percentage of plastic work that is dissipated as heat.

The temperature softening effect may be added to the yield function or the equivalent stress in the same manner as the viscous stress term described in section 3.1.6. To write the expression more compact it is convenient to introduce the homologous temperature T^*

$$T^* = \frac{T - T_0}{T_m - T_0} \quad (3.19)$$

Where T is the current temperature, T_0 is a reference temperature, typically $25^\circ C$, and T_m is the melting temperature of the material. The temperature contribution to the equivalent stress may now be expressed as

$$\sigma_{eq} = (\sigma_0 + R(p))(1 - (T^*)^m) \quad (3.20)$$

Where m is a material constant describing the temperature sensitivity that can be found through a calibration of several tension tests at different temperatures.

3.1.8 Modified Johnson-Cook

By considering the von Mises yield criterion, combined with the work-hardening, rate dependency, and the temperature softening, all these contributions may now be collected to one expression for the equivalent stress. The result is the Modified Johnson-Cook (MJC) constitutive model. The equivalent stress expressed through MJC reads

$$\sigma_{eq} = \varphi(\sigma_{ij}) = (\sigma_0 + R(p))(1 + \dot{p}^*)^c (1 - (T^*)^m) \quad \text{for} \quad f > 0 \quad (3.21)$$

Where

$$\dot{p}^* = \frac{\dot{p}}{\dot{p}_0} \quad (3.22)$$

3.1.9 Ductile fracture

When a ductile metal alloy is being stretched, voids around second phase particles may occur. As a result of increased plastic strains and hydrostatic tension, these voids grow and eventually cause failure. As the voids grow, the metal accumulates damage. The Cockcroft-Latham fracture criteria aims to model the nature of ductile fracture[38], and is the applied fracture criteria throughout this thesis.

The Cockcroft Latham fracture criteria

Cockcroft and Latham suggested that a failure criterion should include both stresses and plastic strains. A way of doing this is to formulate the accumulated damage as a function of the plastic work per unit volume. They also suggested that the hydrostatic tension should be included. The result is a fracture criterion based on the plastic work found by integrating the major principal stress, σ_1 over the equivalent plastic strain p , and it is given by the equation

$$D = \frac{W}{W_c} = \frac{1}{W_c} \int_0^p \langle \sigma_1 \rangle dp \quad (3.23)$$

W_c is the amount of plastic work the material will experience when loaded to fracture and is considered a material parameter. W is the current amount of plastic work, meaning that the damage parameter D always will be in the range $[0,1]$. Fracture will occur when D has reached its critical value. Normally this is set to equal 1, but a certain percentage of maximum damage may also be applied, i.e. $D_{crit} = 0.9$. To only account for the accumulation of damage for hydrostatic tension, σ_1 is put inside Macaulay brackets, which is defined by the relation

$$\langle \sigma_1 \rangle = \frac{1}{2} (\sigma_1 + |\sigma_1|) \quad (3.24)$$

Eq.(3.24) assures that only hydrostatic tension will contribute to the accumulation of damage.

3.2 Shock wave propagation in air

The blast event in this thesis consists of a shock wave propagating in air. For the undisturbed air within the SSTF, atmospheric pressure and a temperature of 20° is assumed. In the particular case of shock or blast wave propagation, the viscosity may be neglected and the fluid is then incapable of transferring shear forces [39]. The fluid is further assumed to behave compressibly. This section on how to model the fluid is based on work done in [40] [3].

3.2.1 The Euler equations

The assumption of an inviscid flow allows for Eqs. (2.5), (2.14) and (2.15) presented in Section 2.5.1, to be rewritten as the Euler equations. For a compressible flow, these are given by

$$\frac{D\rho}{Dt} + \rho \nabla \cdot \mathbf{v} = 0 \quad (3.25)$$

$$\frac{D\mathbf{v}}{Dt} + \frac{1}{\rho} \nabla p = \mathbf{g} \quad (3.26)$$

$$\frac{\partial(E)}{\partial t} + \nabla \cdot (\mathbf{v}E) = \nabla \cdot (\rho \mathbf{v}) = \rho \mathbf{f}_{\text{body}} \cdot \mathbf{v} \quad (3.27)$$

where Eq.(3.25) represents the conservation of mass which is unchanged. Eq.(3.26) describe the conservation of momentum and Eq.(3.27) represents the conservation of energy. Eqs. (3.25) and (3.26) may be found in [39].

3.2.2 Equation of state for air

As mentioned in Section 2.5.2, an equation of state is applied to obtain a solvable system of equations. For this thesis, the air is assumed to behave as an ideal gas. The ideal gas law is commonly given as

$$pV = MRT \quad (3.28)$$

where p represents the pressure, V the volume of the fluid, M the mass, T is the temperature and R is a material-specific constant. Eq.(3.28) may be expressed in various forms and will in this thesis be applied on the form

$$p = \rho RT \quad (3.29)$$

$$p = \rho(\gamma - 1)e \quad (3.30)$$

where ρ is the density. The ratio of specific heats are given as $\gamma = c_p/c_v$, where c_p and c_v are given at constant pressure and constant volume respectively. Further, e represents the specific internal energy per unit mass.

The ideal gas law is suitable for most dynamics problems regarding gas, except for cases involving the combination of high pressures and low temperatures. Such conditions lead to small inter-particle distances relative to the size of the particles, and the inter-particle forces become more significant. To describe the gas in this state, the presented EOS is not sufficient.

3.2.3 Fluid parameters

All fluid parameters related to the equations given in Chapter 2 and 3 are well established in the literature and no experiments for identification or validation has been carried out in this thesis. The parameters presented in Table 3.2 are found in [41][42].

Table 3.2: Fluid parameters describing air at atmospheric pressure and room temperature. These data are taken from [41][42].

| Parameter | Description | Value | Units |
|-----------|----------------------------------|-----------------------|----------------------|
| ρ | Density | 1.2041 | [kg/m ³] |
| R | Gas constant | 287 | [J/kg·K] |
| c_v | Specific heat, constant volume | 716 | [J/kg·K] |
| c_p | Specific heat, constant pressure | 1005 | [J/kg·K] |
| μ | Dynamic viscosity | $1.848 \cdot 10^{-5}$ | [kg/m·s] |

Chapter 4

Preliminary study part I

Early in the work with this thesis, it was decided to conduct tests in the SSTF on 0.8 mm Docol 600DL steel plates. However, the geometry of these configurations was not decided. Based on the previous work, much was already known about the behavior of plates in the shock tube, and data from tests on Docol 600DL was available. This chapter is intended to discover what behavior to expect from the new plate configurations, and based on this a test matrix is to be decided.

To model the full shock tube problem was not the purpose of this initial study. Instead, the focus is placed on studying the structural response of the different plate configurations, using simple modeling techniques.

The preliminary study is divided into two parts, Preliminary study part I and Preliminary study part II, presented in this chapter and Chapter 5 respectively. The first part deals with models given very simple boundary conditions and the geometrical complexity is increased in Chapter 5. This division was considered convenient because more complex models are computationally expensive. This chapter is therefore intended to give as much insight into the numerical problem as possible before increasing the geometrical complexity.

4.1 Description

Through pure Lagrangian analyses, this chapter aims to explore the effects of different discretizations and element-formulations. All models will utilize symmetry by only modeling the quarter geometry, and the load is being idealized through pressure-time curves obtained by Aune [3]. These loading curves were determined by exposing a 5 cm thick steel plate to nominal firing pressures in the range 5 to 60 bar. The blast-exposed area of the plate was covered with sensors sampling the pressure, and a Friedlander curve was fitted to the data. Loading curves have been calibrated for a number of different driver lengths, but in this study, all experiments are using a fixed length of 77 cm.

To be in continuance with previous work done at SIMLab, NTNU, it was decided to focus on square perforations and slits. The perforations already tested by Aune [3] and Granum and Løken [29] resulted in a 16% reduction of the blast-exposed area. By keeping the total hole area constant, the new configurations divides the 16% area reduction into one single perforation and 16 perforations respectively. This was intended to change the structural response of the plates and to investigate fluid-structure interaction effects. The slit configurations studied are similar to the ones tested by Stensjøen and Thorgeirsson [30], but the plates are made of Docol 600DL instead of aluminum. In addition, the aluminum plates were 1.5 mm thick. In [30], it was found challenging to model the angled slit configurations, as it challenges the mesh geometry, and possibly the element-formulation. The configurations evaluated are shown in Figure 4.1(a) - 4.1(f), where the full plate (FP) and perforated configuration (P2) are the ones already tested at NTNU. The plate dimensions of 300 mm x 300 mm refer to the blast-exposed area of the plates.

The previously obtained test data for the Docol 600DL steel plates gave the opportunity of benchmarking numerical models prior to the experimental testing. With this opportunity, it was an absolute goal to come up with an accurate test matrix. This would be a series of tests that resembles the predicted behavior seen in the simulations. The plan was to test each configuration at three different nominal firing pressures. The first should result in large deformations and crack arrest. For the second test, it was intended to have mainly deformation and only minor or no cracking. Lastly, the goal was a firing pressure that resulted in complete failure of the plate.

The benchmark study applied the experimental work conducted by Granum and Løken [29] and aims to learn how the different modeling approaches represent the experiments and to explore the sensitivity of different parameters. An effort was made to qualitatively reproduce the results in [29], before modeling new plate configurations.

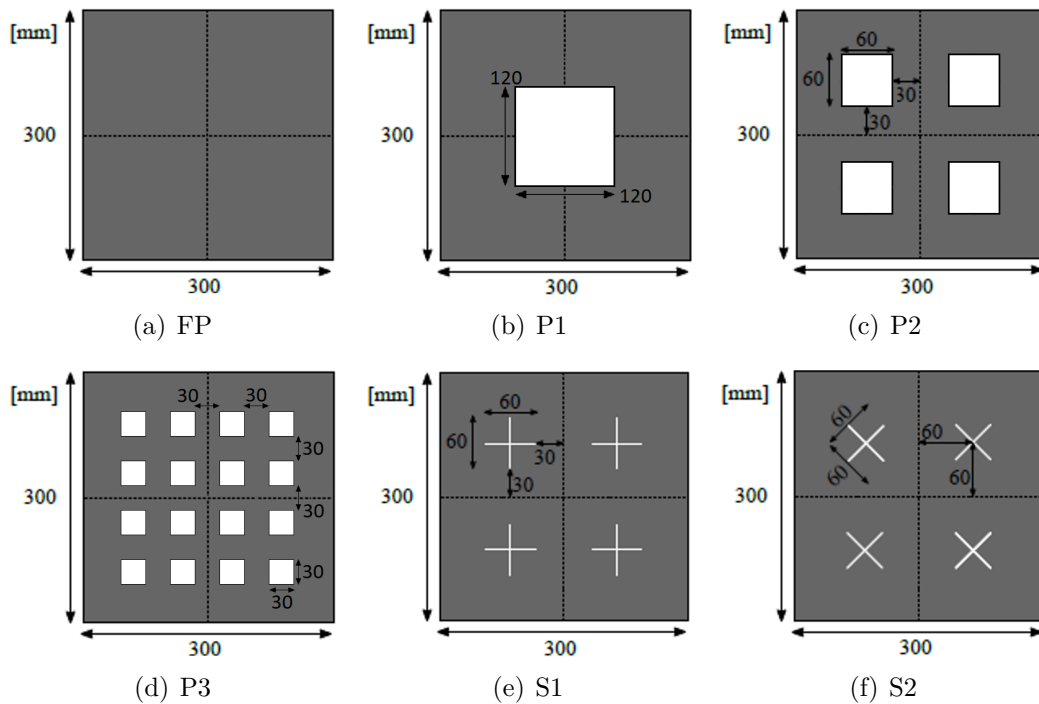


Figure 4.1: The configurations evaluated in this thesis, including both new configurations and the ones studied by Granum and Løken [29]. Configurations already tested at NTNU are the FP and P2.

4.2 Models

The models presented in this chapter include only the blast-exposed area of the plates and utilize symmetry about two axes. Since the models are geometrically simple and exclude the clamping frames that hold the blast-exposed plate in place, the outer boundaries are fixed. Only models that utilize symmetry about two axes will be run. It is shown in [29], [28], and [30], that symmetric models differ negligibly from full models for this specific problem. The perforations are modeled as perfect squares and the slits as stars with a center gap of 0.01 mm.

Different configurations, mesh sizes, and element types will be evaluated. To keep track of all parametric changes, a naming convention is introduced in Table 4.1. The naming convention states the applied element type, the approximate size of the elements, the geometrical configuration of the plate tested and the applied loading. This convention is applied throughout both this chapter and Chapter 5.

Table 4.1: Naming convention used to label different models in the preliminary numerical study. The labels will be used in plots and in tables.

General label name: XX_EE_ZZ_phh_tt

| Part of name | Possible configurations | Explanation |
|--------------|-------------------------|--|
| XX | FP | Full Plate |
| | PX | Perforated plate, geometry X |
| | SX | Slit plate, geometry X |
| EE | S4R | Shell element, reduced integration |
| | C3D8R | Brick element, reduced integration |
| ZZ | 0xx | Mesh size of 0.xx mm |
| | xx | Mesh size of x.x mm |
| phh_tt | p77_tt | hh = driver length in [cm] tt = nominal firing pressure [bar] |

4.2.1 Description of the shell element models

The shell element models apply quadratic S4R or triangular S3R shell elements with an approximate element size on the range 3.2 mm to 0.8 mm. These elements utilize reduced integration, built-in hourglass control, drilling stiffness, and are linear general purpose shell elements meant to handle both thin and thick shell problems [43].

Meshing of the shell models

When modeling fracture, the geometry of the mesh and the element size may be of great importance [44] [30]. To investigate this effect, a mesh study was conducted.

Several different discretizations of the S2 configuration has been evaluated and are given in Figure 4.2(e) - 4.3(f), referred to as M1 to M4. Due to the angular difference of 45° between the slits and the outer boundary, the mesh for the S2 configuration requires a transition zone to adjust. M1 and M2 apply only squared S4R elements across the entire plate. The two meshes are similar but differ in the mesh transition zone in front of the tip of the slit. The M3 mesh is constructed by using triangular S3R elements in a squared zone around the slit, and S4R elements in the rest of the plate. This mesh is regular but introduces a mesh with mixed element types. For M4, S4R elements are used for the entire plate and the medial axis meshing technique is applied [45]. All four meshes use an approximate size of 1.0 mm but some elements are smaller in the transition zones, which leads to higher computational costs.

For the S1, P1, P2, and P3 configurations, only regular meshes was applied. The different element sizes for the P1 configuration in presented Figures 4.2(a) to 4.2(d).

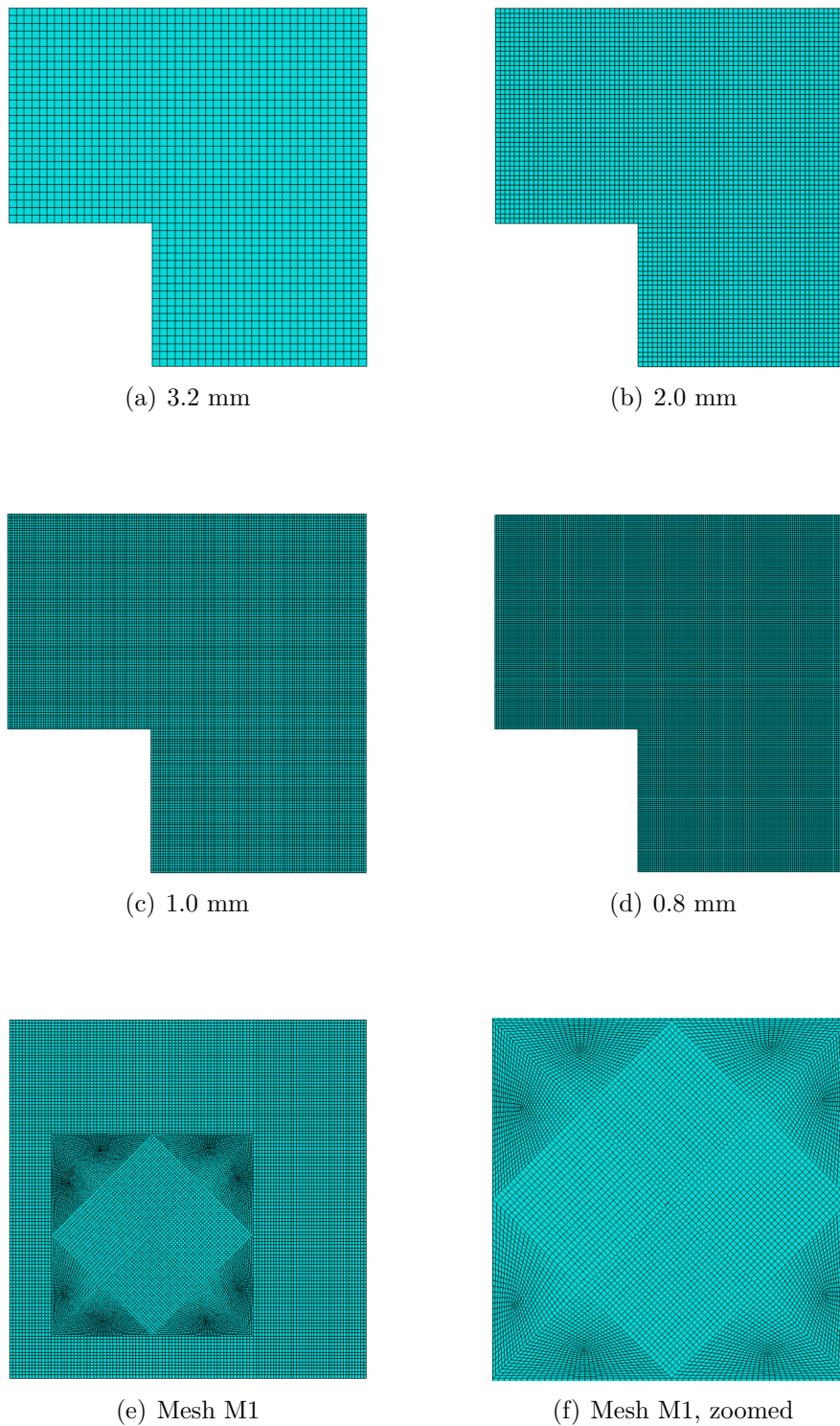
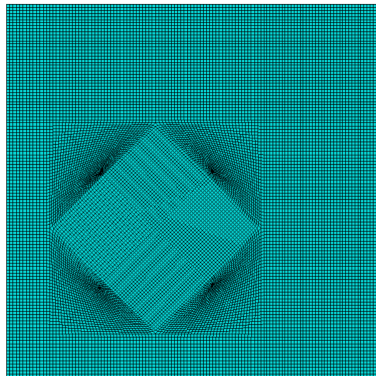
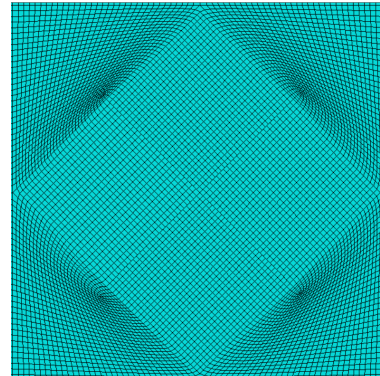


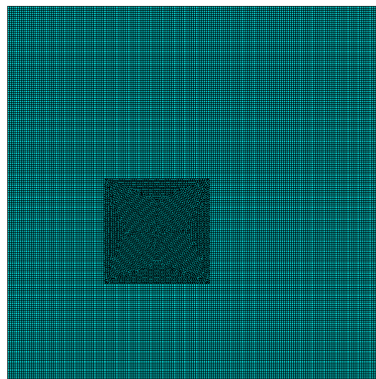
Figure 4.2: Meshes applied to the different configurations in the simulations in Abaqus. (a)-(d) Show different mesh sizes and geometries used in the simulations for the P1, P2, and the P3 configuration. (e) and (f) shows the M1 mesh for the S2 configuration.



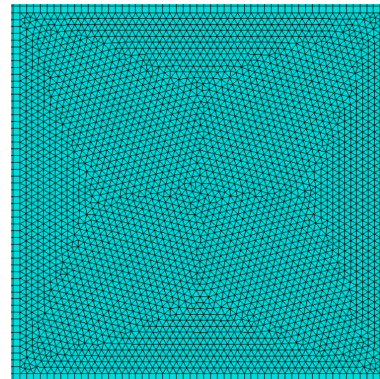
(a) Mesh M2



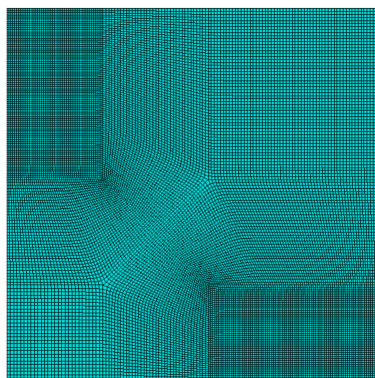
(b) Mesh M2, zoomed



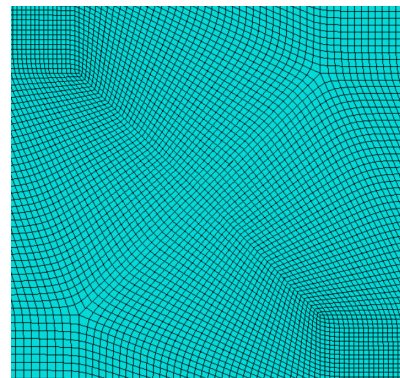
(c) Mesh M3



(d) Mesh M3, zoomed



(e) Mesh M4



(f) Mesh M4, zoomed

Figure 4.3: Meshes applied to the S2 configuration. (a),(c) and (e) shows the entire mesh, used for the meshing methods M2, M3 and M4 respectively. (b), (d) and (f) are showing zoomed images of the mesh around the slit for M2, M3 and M4.

4.2.2 Description of the solid element models

All models apply the C3D8R element. This is a linear 8-noded element with reduced integration and built-in hourglass control [46]. Simulations have been run with two, three, and four elements across the thickness of the plate. Three elements result in an approximate element size of 0.26 mm, and approximately 1 million elements. When modeled with two and four, the numbers are approximate 250 000 and 2 million elements respectively. The number differs slightly between the slit and perforated configuration as the perforations remove 16% of the total meshed area.

For P1, P2, P3, and S1, the models use regular mesh geometries similar to what is shown in figure 4.2(a). The S2 configuration is modeled slightly different for the solid models than for the shell models. Figure 4.4(a) shows the partitions made to construct the mesh for the S2 model. The green area is meshed using a structured mesh, while the yellow area applies the meshing algorithm sweep advancing front [47]. Figure 4.4(b) shows the corresponding mesh in the area close to the slit. The mesh is mostly uniform but there is a transition zone between the areas where the two different meshing techniques are used. Due to much higher computational costs when running the solid element model, no study on the mesh geometry was included.

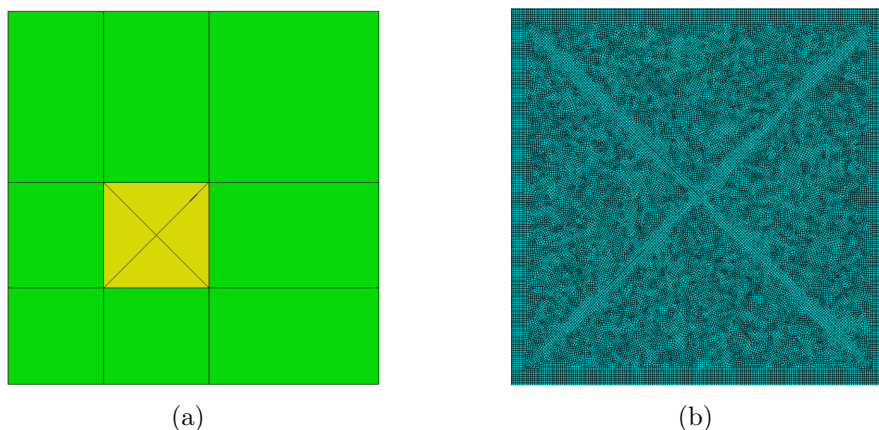


Figure 4.4: Partitioning and meshing of the S2 configuration. (a) shows the meshing algorithms applied in the simulations. Green represents the structured meshing algorithm and sweep advanced front meshing is represented with yellow [47]. (b) shows the result of sweep advanced meshing for the yellow area.

4.3 Results

The results obtained for this chapter will be presented in three main blocks. First the results from the benchmark study, where numerical results are compared to experiments done by Granum and Løken in [29]. The two following parts are evaluating the new slit and perforated configurations separately.

4.3.1 Benchmark study

In their experiments, Granum and Løken[29] reported the observed midpoint displacement and pictures of the crack arrest in the plates among other observations. To evaluate the numerical approach chosen in this thesis, these two parameters will be compared for different numerical models. Midpoint displacement data obtained in their work will be included, labeled as -GL. The midpoint displacement data was obtained using 3D-DIC. When applicable, pictures of the crack arrest from the actual test will be compared to the crack propagation found in the simulations. Further details regarding their experimental work can be found in their master thesis [29]. Some results obtained by Aune [3] are also included and labeled -VA.

Simulations of the full plate configuration, using shell elements

Only shell element models were applied for the full plate configuration. These simulations were among the first in this study, and plots of the midpoint displacement for different mesh sizes are presented in Figures 4.5(a) to 4.6(b). Plots of artificial- and total energy are also included for some representative simulations to evaluate the analyses, presented in Figures 4.6(c) and 4.6(d).

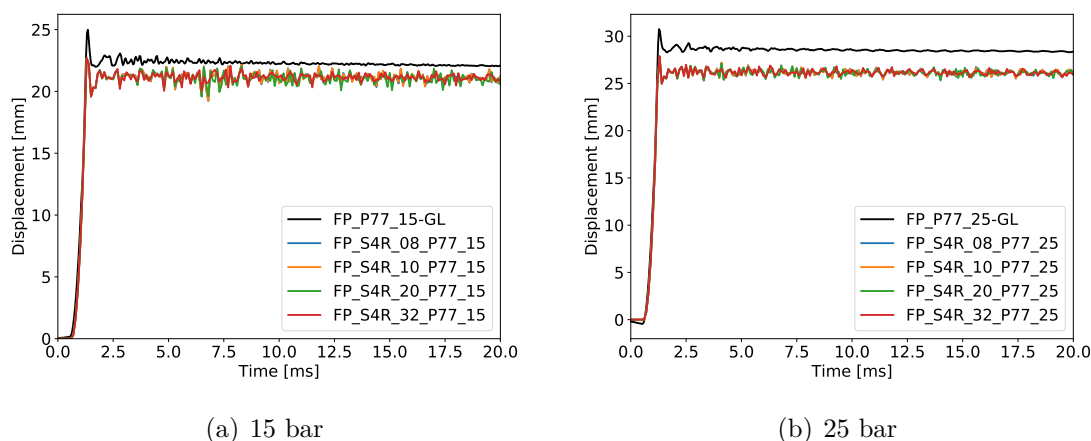


Figure 4.5: Midpoint displacement vs. time for the full plate configuration exposed to firing pressures of 15 and 25 bar. Experimental results by Granum and Løken are included and labeled as -GL.

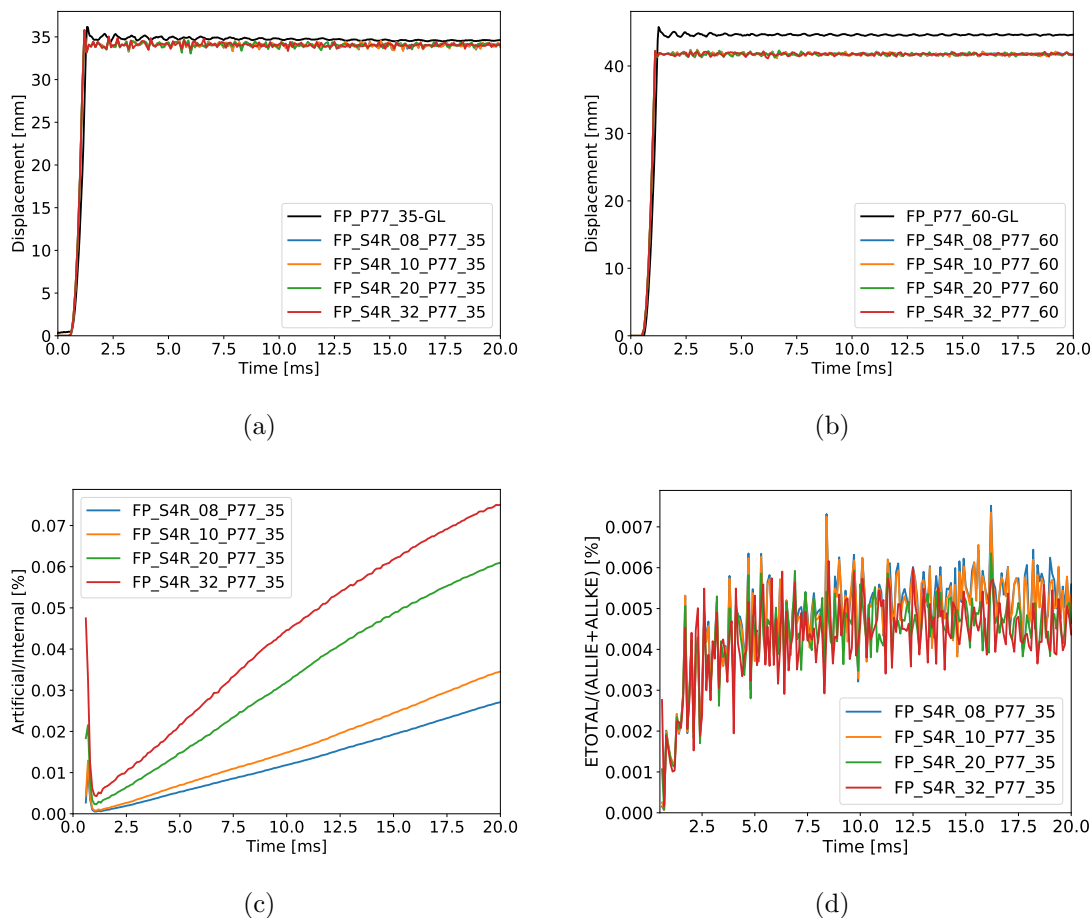


Figure 4.6: Displacement and energy plots for the full plate configuration exposed to different loading curves indicated in each plot. (a) and (b) are showing the midpoint displacements vs. time at 35 and 60 bar. Experimental results obtained by Granum and Løken[29] are included and labeled as -GL. (c) is showing the artificial energy vs. time at 35 bar, and (d) is showing the conservation of energy at 35 bar.

As seen in Figure 4.5(a) to 4.6(b) the measured midpoint displacements qualitatively responds in a similar way as the experiments. However, it is important to note that the simulated response is consistently stiffer than the experimental results, and the deviation is varying for the different firing pressures. The simulation at 35 bar is the one closest to predict the experimental results. Further, the displacement response does not change noticeably on the range of element sizes tested.

Figure 4.6(c) shows that the ratio of artificial energy divided by the internal energy in the model is consequently below 0.08%. As mentioned in Section 2.4.2, the artificial energy is typically related to the resistance of hour-glassing and the added drilling stiffness to the elements. ETOTAL is the total energy balance in the model [48], and should remain constant as no energy is to be created during the analysis. The total energy in the simulation divided by the sum of kinetic- and internal energy is oscillating around 0.004 to 0.005%, as seen in Figure 4.6(d).

Perforated plates, P2

The midpoint displacements for the P2 configuration, presented in Figure 4.7, shows noticeable oscillations for the simulations at 5 bar compared to higher pressures. A plausible explanation might be that higher firing pressures lead to more energy being dissipated as plastic work, resulting in a damped behavior. In addition, the increased pressure force might also contribute to the damping.

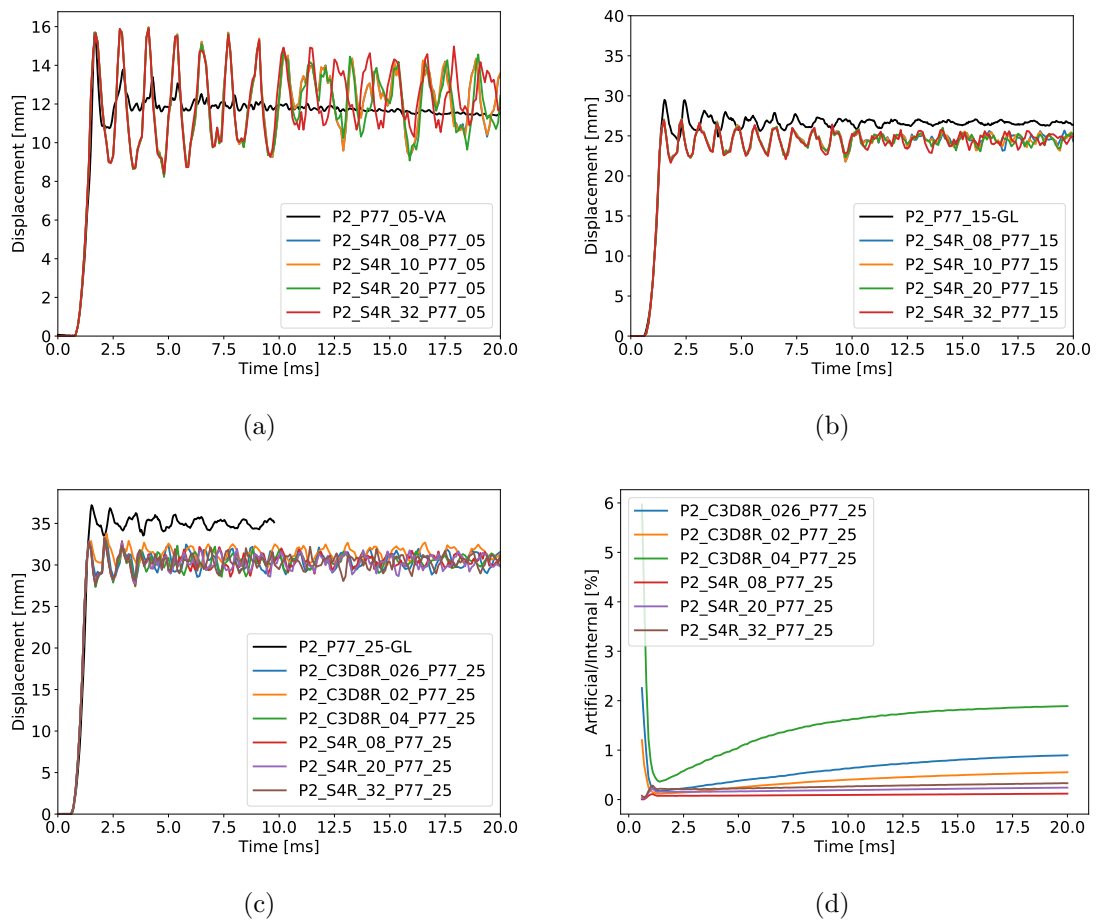


Figure 4.7: For the P2 configuration, experimental data and the simulated response for nominal firing pressures of 5, 15, and 25 bar is given. (a) to (c) shows the midpoint displacements vs. time for 5, 15 and 25 bar. (d) shows the artificial energy for simulations at 25 bar.

Results for the firing pressure of 35 bar are excluded as this led to failure in the experiments. The simulated midpoint displacements for the P2 configuration shows the same trend as the full plates, giving too stiff solutions. The exception is for the 5 bar test, where the initial peaks are captured identically. The 25 bar test was run with both shell elements applying different element sizes and with two, three and four solid elements across the thickness of the plate. All models are capturing the first 3 ms of the response almost identically, except the solid element analysis with four elements through the thickness. This model results in a slightly softer solution than the others. It should be noted that this simulation experiences the largest crack propagation, which may explain the reduced stiffness.

The artificial energy for the analyses on P2 is magnitudes higher than for the Full plates, but still below the suggested value of 10% [11]. For the conservation of energy, the total energy divided by the kinetic and internal energy is comparable to observations for the full plates.

In addition to the midpoint displacement, it was considered important to compare the simulated crack propagation to what was found experimentally by Granum and Løken[29]. They reported the crack arrest when testing their perforated plates with a nominal firing pressure of 25 bar, as shown in Figure 4.9(a) and 4.9(b). The crack lengths were not explicitly stated, and the length of the cracks are crudely measured relative to known dimensions in the pictures.

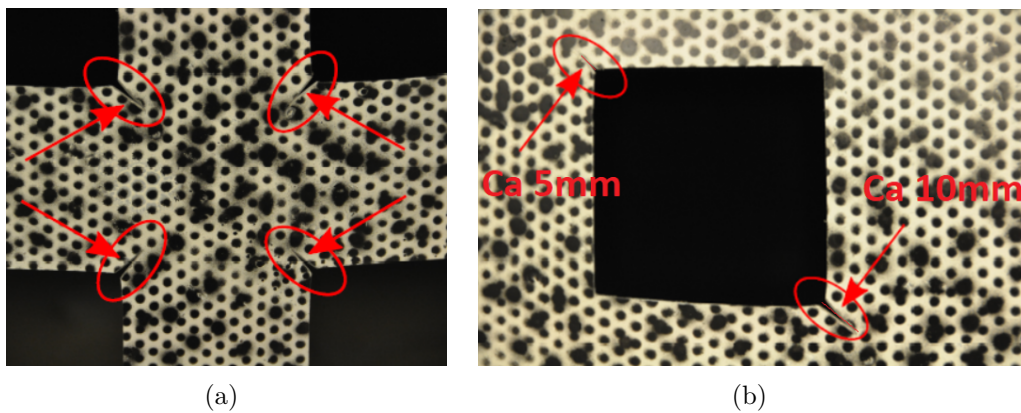


Figure 4.9: Crack arrest for nominal firing pressure of 25 bar. Both images are from the same test. (a) Shows the four cracks propagating towards the center and (b) is showing the upper left perforation of the P2 plate. Both images are taken from [29].

To compare the numerical results with the reported cracks, the accumulated Cockcroft-Latham damage (SDV_W) for different element sizes is shown in Figure 4.10. All simulations are run with reduced integration. For the 8-node solid elements, C3D8R, this means only one single integration point located at the volume center for each element. For the shell elements, S4R, the consequence is one integration point across the area, and five integration points across the thickness. Remember from Section 2.4.3 that elements are eroded if the damage accumulated in all integration point

exceeds 555.0 MPa. The fields presented in Figure 4.10 are taken at 20 ms. Larger elements are observed to lower the value of accumulated damage in the corner of the perforation.

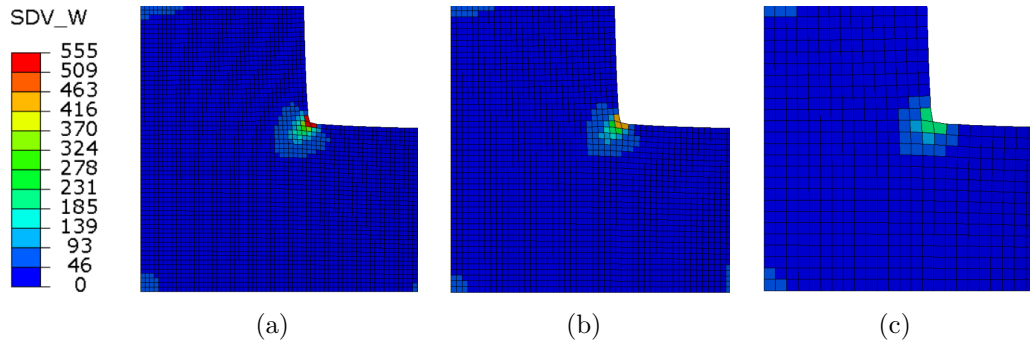


Figure 4.10: Damage accumulation in lower left corner of the perforation of P2 at 25 bar using S4R elements with an approximate size of (a) 0.8 mm, (b) 1 mm and (c) 2 mm.

Figure 4.11 shows the crack propagation at 20 ms for solid element simulations using two, three and four elements across the thickness. The field output shows the SDV_W field. However, the interesting observation in this figure is the relative length difference of the arrested crack for the different element sizes.

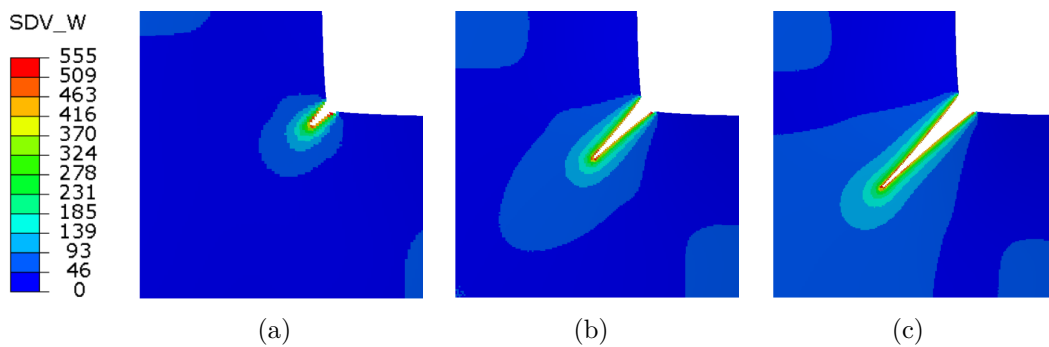


Figure 4.11: Showing the longest crack, propagating towards the center of the plate for P2 at 25 bar using C3D8R elements with an approximate size of (a) 0.4 mm, (b) 0.26 mm and (c) 0.2 mm.

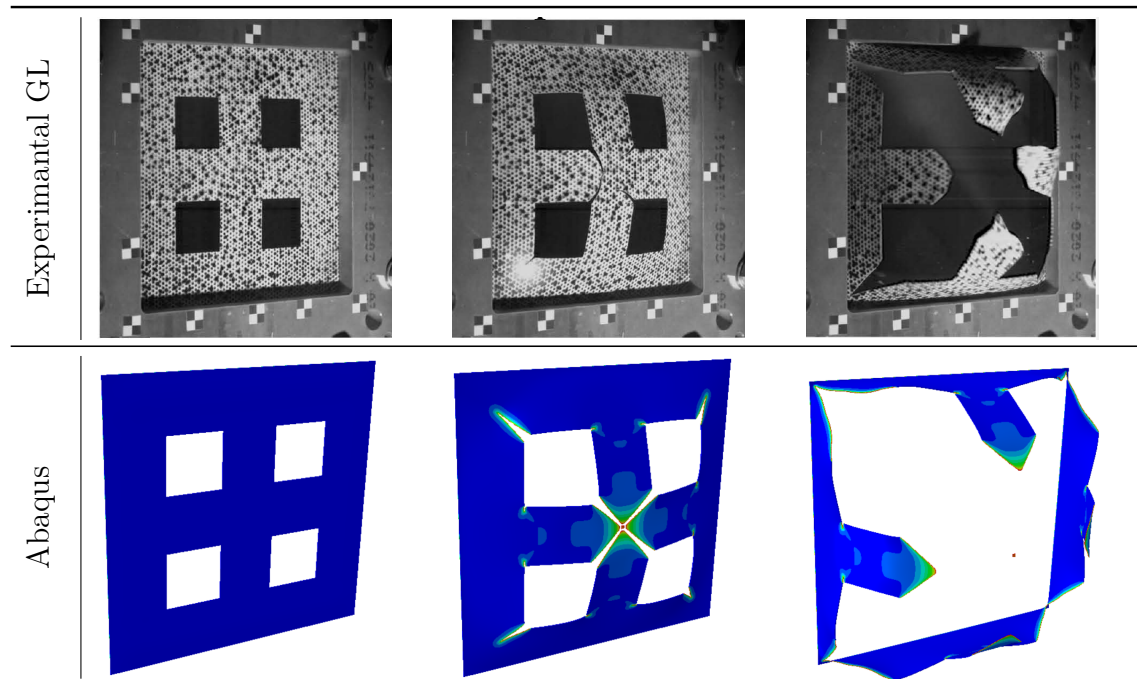
In Table 4.2 the arrested crack length for the different solid element models are listed. Estimated crack lengths from Figure 4.9 are also included for comparison.

Table 4.2: Crack lengths for the P2 configuration at 25 bar. Comparison between the simulated response when using different solid-element sizes and the experimentally obtained data by Granum and Løken [29].

| Model | Long Crack [mm] | Short Crack [mm] |
|---------------------------------|-----------------|------------------|
| Experiments by Granum and Løken | 10 | 5 |
| C3D8R, 0.20 mm | 19 | 8 |
| C3D8R, 0.26 mm | 11 | 6 |
| C3D8R, 0.40 mm | 5 | 3 |

Experimentally, the nominal firing pressure of 35 bar resulted in complete failure for the P2 configuration. None of the shell element analyses reproduced failure at 35 bar, neither did any crack initiate at 25 bar. The solid element model with three elements across the thickness showed promising results for the 25 bar test and predicted complete failure at 35 bar. The numerically obtained failure mode is compared to experimental results in Table 4.3. The times at which the images from the test and the simulations are collected are not synchronized, and the figures are only intended to illustrate the two failure modes.

Table 4.3: P2 configuration with 35 bar firing pressure. Test compared to solid element analysis applying three elements across the plate thickness. Images of experiments are taken from [29].



It is evident in Table 4.3 that the solid element simulation was able to predict the

same kind of crack propagation pattern as observed in the test.

A summary of all the relevant simulations run for the FP and P2 configurations are given in Table 4.4. This table contains the model name, mean midpoint displacement in the time interval 15-20 ms and cracks length. The crack lengths given are the measured diagonal cracks from the center corner in the perforation towards the center of the plate. For the simulations resulting in failure, both the midpoint- and the crack length column will only contain the word Failure.

Table 4.4: Mean midpoint displacement measured between 15 and 20 ms, and obtained crack lengths for the FP and the P2 configuration are presented. The measured crack length for the P2 configuration is for the crack illustrated in Figure 4.11. For the FP configuration no cracking was initiated in any of the simulations.

| Model | Mean displacement [mm] | Crack Length [mm] |
|---------------------|------------------------|-------------------|
| FP_S4R_08_P77_15 | 21.08 | No crack |
| FP_S4R_10_P77_15 | 21.10 | No crack |
| FP_S4R_20_P77_15 | 20.98 | No crack |
| FP_S4R_08_P77_25 | 26.14 | No crack |
| FP_S4R_10_P77_25 | 26.13 | No crack |
| FP_S4R_20_P77_25 | 26.09 | No crack |
| FP_S4R_08_P77_35 | 33.99 | No crack |
| FP_S4R_10_P77_35 | 33.98 | No crack |
| FP_S4R_20_P77_60 | 41.65 | No crack |
| FP_S4R_08_P77_60 | 41.75 | No crack |
| FP_S4R_10_P77_60 | 41.74 | No crack |
| FP_S4R_20_P77_60 | 41.75 | No crack |
| P2_S4R_08_P77_05 | 12.14 | No crack |
| P2_S4R_10_P77_05 | 12.14 | No crack |
| P2_S4R_08_P77_15 | 24.64 | No crack |
| P2_S4R_10_P77_15 | 24.59 | No crack |
| P2_S4R_08_P77_25 | 30.55 | No crack |
| P2_S4R_10_P77_25 | 30.55 | No crack |
| P2_C3D8R_02_P77_25 | 31.41 | 18.67 |
| P2_C3D8R_026_P77_25 | 30.99 | 11.38 |
| P2_C3D8R_04_P77_25 | 30.32 | 4.53 |
| P2_S4R_08_P77_35 | 40.86 | 11.74 |
| P2_S4R_10_P77_35 | 40.54 | 2.82 |
| P2_C3D8R_02_P77_35 | Failure | Failure |

4.3.2 New plate configurations

By comparing the reference point displacements for the P1 configuration to the mid-point displacements obtained for P2, it is observed that P1 consequently exhibits the largest displacements. Although the different sampling points make a direct comparison challenging, it qualitatively illustrates the effect of removing the load carrying capacity in the middle of the plate. By removing the mid square, membrane forces can not be transmitted across the free boundary, resulting in large deformation.

The artificial energy and the the energy balance in the models are observed to be considerably larger for the solid element models than for the shell element models. This is observed in Figure 4.12(c). A plausible explanation may be the larger crack propagation obtained in the solid element models. However, the artificial energy is lower than the suggested limit of 10% [11].

The final crack arrest for the firing pressure of 10 bar using both shell and solid elements is presented in Figure 4.13. As observed in Section 4.3.1, the shell element formulation under-predicts the crack propagation compared to solid elements. In the solid-element analysis at 10 bar, the final crack length is 10.49 mm while the shell element model applying an element size of 0.8 mm gives a crack length of 2.25 mm. When using larger shell elements than 0.8 mm no cracks were initiated in the analyses.

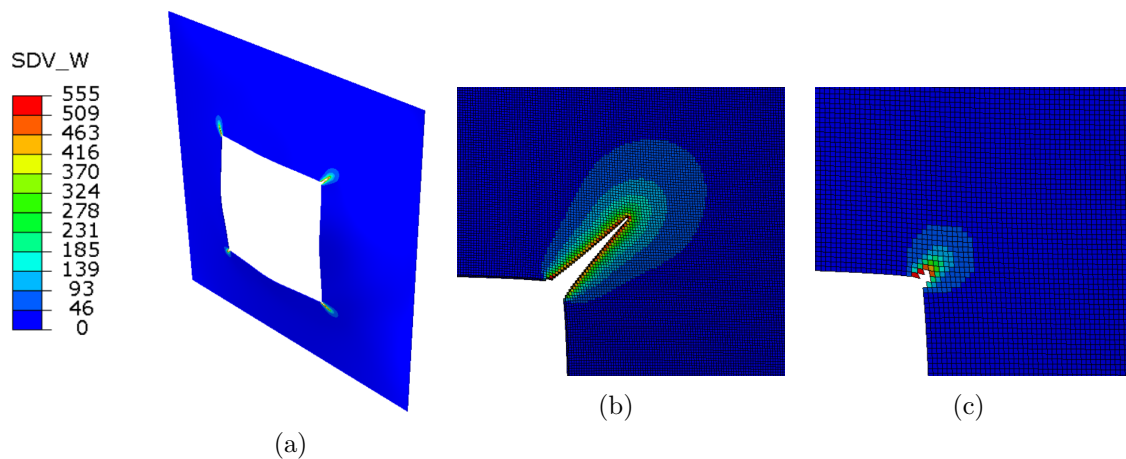


Figure 4.13: Crack arrest for P1 at 10 bar. (a) 0.8 mm S4R elements, (b) 0.26 mm C3D8R elements and (c) 0.26 mm C3D8R elements.

When exposed to a firing pressure of 15 bar, the model using 0.26 mm C3D8R elements experienced a complete failure. The entire plate opens up by folding outwards as shown in Figure 4.14. However, none of the shell element analyses resulted in complete failure at 15 bar.

In this section, the four new plate configurations will be evaluated. The results will be presented in the same manner as in the benchmark study, i.e., plots describing midpoint displacement, artificial energy, conservation of energy followed by an evaluation of crack arrest, failure mode and required firing pressure to achieve failure. As this numerical work has been conducted to plan the test matrix, only the most relevant results will be presented.

The Perforated P1 configuration

An alternative reference point for displacements has been chosen for P1 as it has its perforation at the centre of the plate. An illustration is presented in Figure 4.12, together with the corresponding displacements, and energy plots.

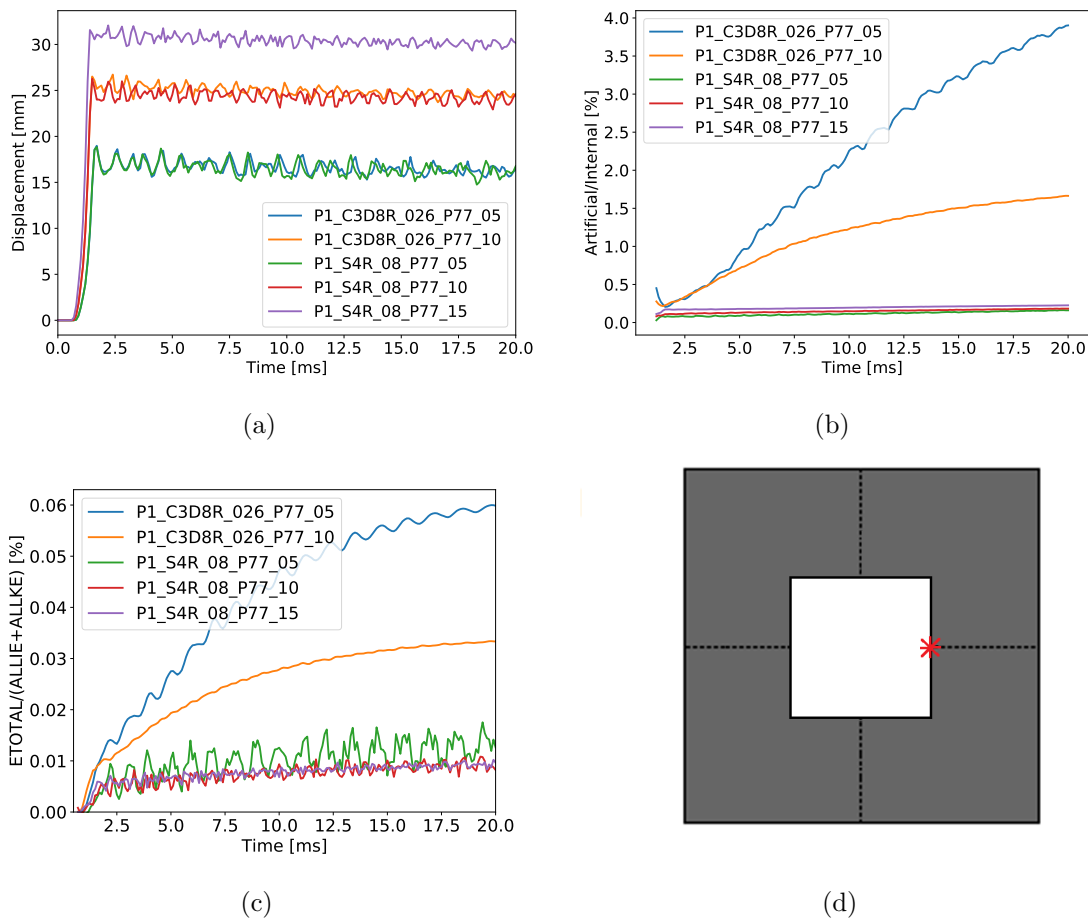


Figure 4.12: Numerical results for the P1 configuration. (a) reference point displacement vs. time, (b) artificial energy vs. time, (c) the energy balance, and (d) indicates the reference point for displacements.

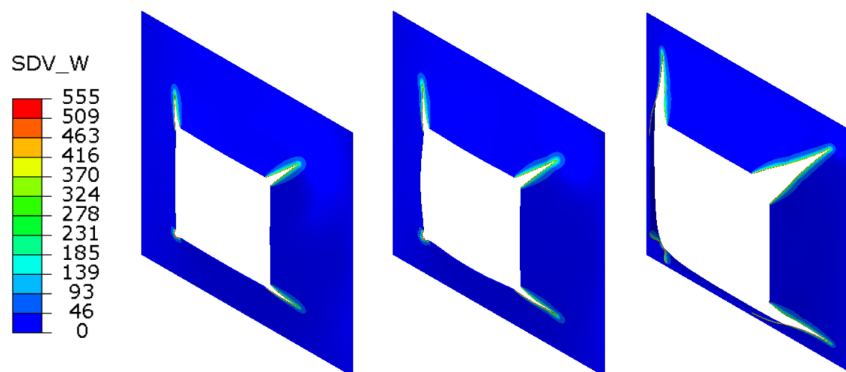


Figure 4.14: Illustrating the failure mode for P1 at 15 bar using 0.26 mm C3D8R elements.

The Perforated P3 configuration

When comparing all simulations on perforated and slit configuration in this chapter, P3 is the configuration undergoing the largest midpoint displacement without experiencing failure. As pointed out in Section 4.3.1, the midpoint displacement does not vary significantly with respect to element size and formulation. The difference between using shell and solid elements are less than 1%. Both midpoint displacements and artificial energy are given in Figure 4.15. The artificial energy follow the same trend as observed for the other configurations.

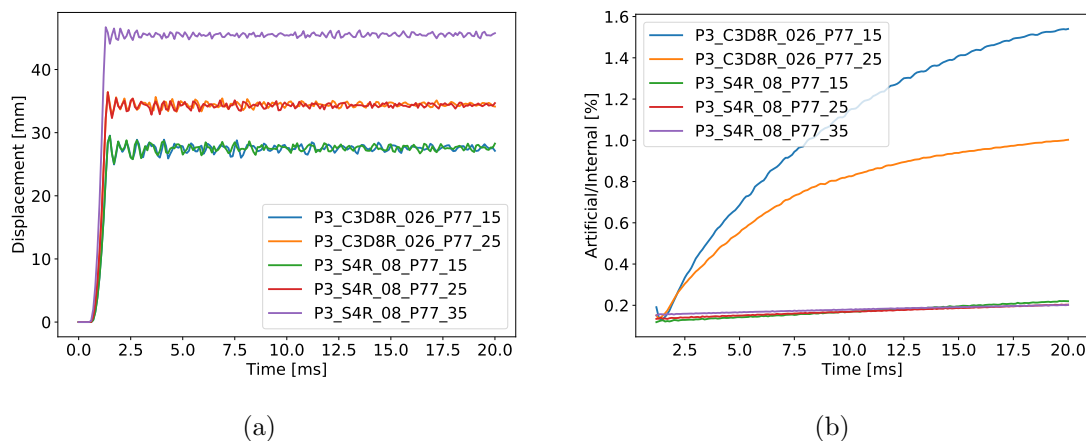


Figure 4.15: Numerical results for the P3 configurations. (a) midpoint displacements vs. time, (b) artificial energy vs. time.

When applying a firing pressure of 25 bar, the 0.26 mm C3D8R element model is predicting crack arrest in all four corners of the perforation closest to the center of the plate. This is shown in Figure 4.16. The longest predicted crack is the one running towards the midpoint of the plate with a length of 2.91 mm. At a firing pressure of 35 bar, the 0.26 mm C3D8R model is experiencing complete failure as illustrated in Figure 4.17(a) and 4.17(a).

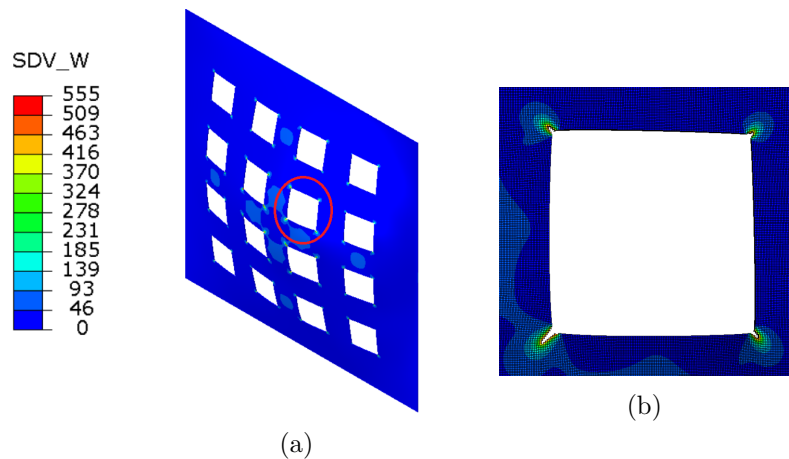


Figure 4.16: Crack arrest for P3 at 25 bar. (a) indicates the evaluated perforation and (b) show crack arrest using 0.26 mm C3D8R elements.

It is observed in Figure 4.17(a) and 4.17(b), that the predicted failure is unsymmetrical. This is strange as the models utilizes symmetry, the loading is uniform, and the material is perfectly isotropic. Hence, the failure should evolve in a symmetrical manner. A numerical round off error, or element erosion patterns has been discussed as possible explanations.

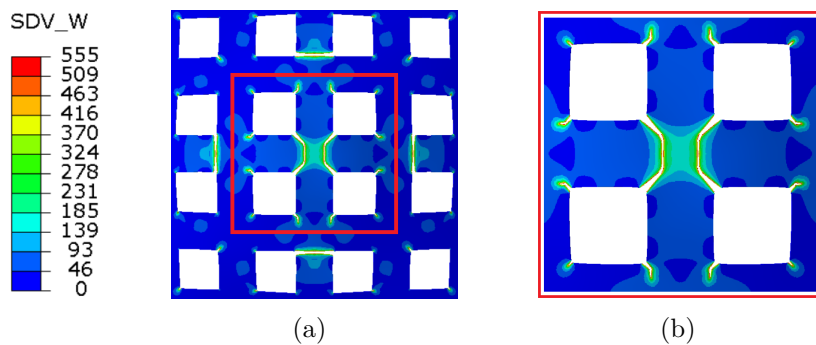


Figure 4.17: Showing the failure mode for the P3 configuration at 35 bar. (a) failure mode at using 0.26 mm C3D8R elements and (b) show a zoomed image of the failure mode.

In Table 4.5 all relevant simulations regarding the P1 and P3 configurations are listed. The crack length given for the P3 configuration is the crack propagating diagonally towards the center of the plate, illustrated in Figure 4.16.

Chapter 4.

Table 4.5: Mean midpoint displacement and obtained crack lengths for the P1 and the P3 configurations. The measured crack length for the P1 configuration is the one illustrated in Figure 4.13. For the P3 configuration it is the crack propagating diagonally towards the center of the plate, illustrated in Figure 4.16.

| Model | Mean displacement [mm] | Crack Length [mm] |
|---------------------|------------------------|-------------------|
| P1_S4R.08_P77_05 | 15.79 | No crack |
| P1_C3D8R.026_P77_05 | 16.41 | 1.1 |
| P1_S4R.08_P77_10 | 24.08 | 2.25 |
| P1_S4R.10_P77_10 | 23.93 | 1.41 |
| P1_S4R.20_P77_10 | 23.57 | No crack |
| P1_C3D8R.026_P77_10 | 24.53 | 10.49 |
| P1_S4R.08_P77_15 | 30.08 | 11.26 |
| P1_S4R.10_P77_15 | 29.43 | 6.4 |
| P1_S4R.20_P77_15 | 29.01 | No crack |
| P1_C3D8R.026_P77_15 | Failure | Failure |
| P3_S4R.08_P77_10 | 21.88 | No crack |
| P3_S4R.08_P77_15 | 27.57 | No crack |
| P3_C3D8R.026_P77_15 | 27.57 | 0.57 |
| P3_S4R.08_P77_25 | 34.36 | No crack |
| P3_S4R.10_P77_25 | 34.41 | No crack |
| P3_S4R.20_P77_25 | 34.27 | No crack |
| P3_S4R.32_P77_25 | 34.18 | No crack |
| P3_C3D8R.026_P77_25 | 34.48 | 2.92 |
| P3_S4R.08_P77_35 | 45.54 | No crack |
| P3_C3D8R.026_P77_35 | Failure | Failure |

The slitted S1 configuration

The midpoint displacements for the S1 configuration responds quite similar to the P2 configuration, and the energy plots follow the same trend as seen previously. Both midpoint displacements and artificial energy is given in Figure 4.18.

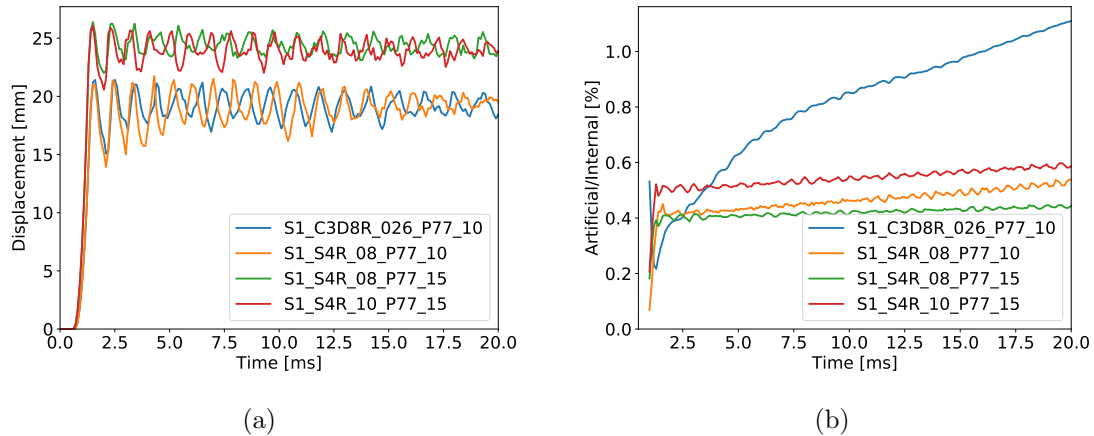


Figure 4.18: Numerical results for the S1 configurations. (a) midpoint displacements vs. time and (b) artificial energy vs. time.

Compared to the other configurations evaluated, S1 and P1 are the only two configurations experiencing crack initiation for both 0.26 mm C3D8R elements and 0.8 mm S4R elements at a firing pressure as low as 10 bar. The crack arrest for the 10 bar simulation is seen in Figure 4.19.

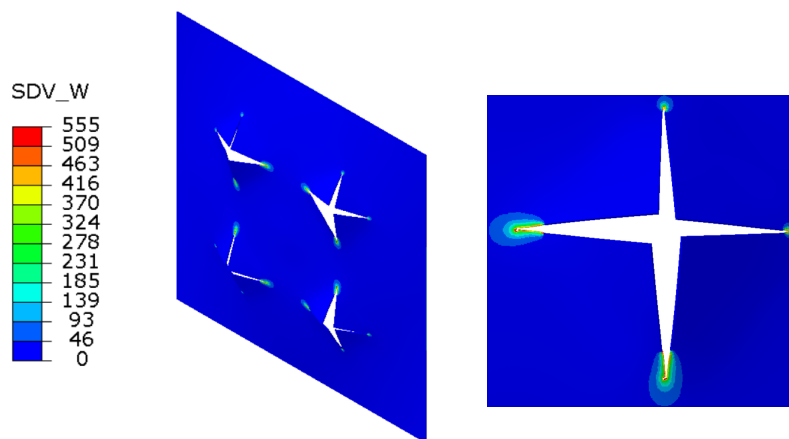


Figure 4.19: Crack arrest for the S1 configuration at the firing pressure of 10 bar.

The failure mode obtained with solid elements at 15 bar seems to qualitatively behave in the same manner as what was found in the masters thesis written by Stensjøen and Torgeirsson [30] and is shown in Figure 4.20. However, it is important to note that the plates evaluated were made of aluminum and had a different thickness.

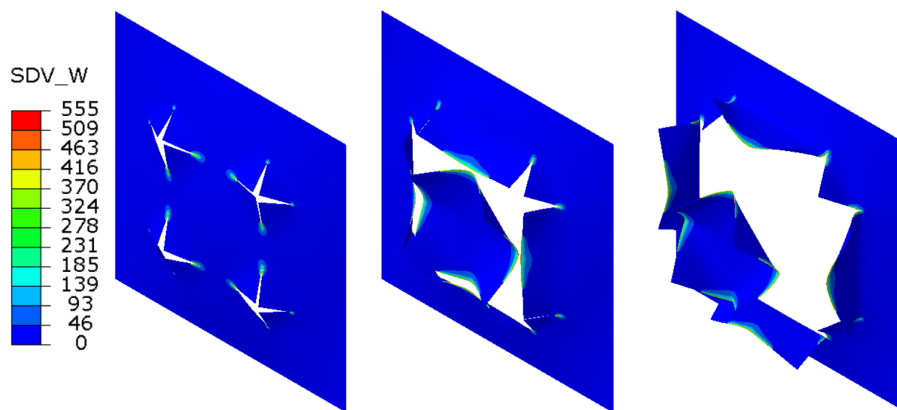


Figure 4.20: Showing the failure mode for the S1 configuration at 15 bar using 0.26 mm C3D8R elements.

The slitted S2 configuration

The midpoint displacements and development of artificial energy for the S2 configuration, seen in Figure 4.21, obeys the trend observed for other configurations. For S2 it is especially evident that oscillations are increased as the pressure load is decreased.

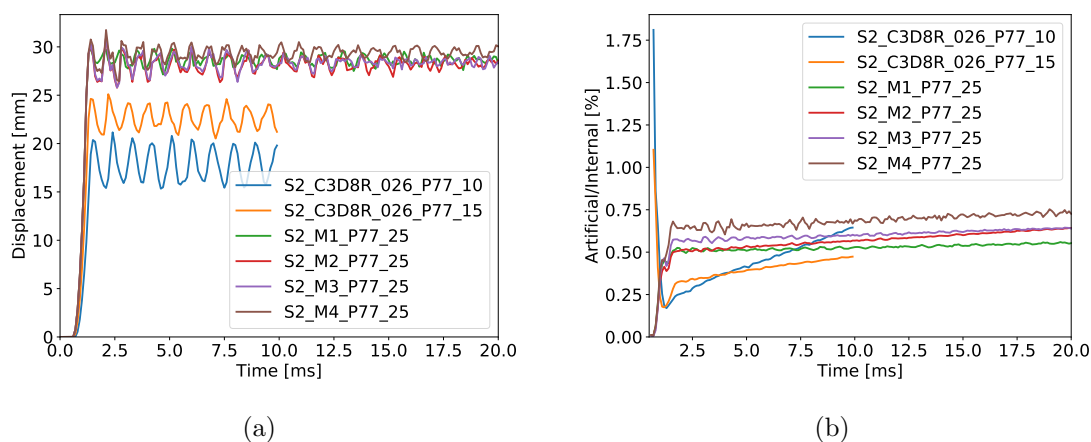


Figure 4.21: Numerical results for the S2 configuration. (a) midpoint displacements vs. time, and (b) artificial energy vs. time.

Although the different shell element meshing techniques do not affect the midpoint displacement in any noticeable degree, it has a great effect on the propagation of the cracks. This is illustrated in Figure 4.22. The images of the slit perforation and zoomed in images of the crack propagating towards the center of the plate is shown. These images indicate that the propagation of the crack is guided by the mesh. This is especially evident for the M2 mesh, as the crack is bending in the same way as the mesh.

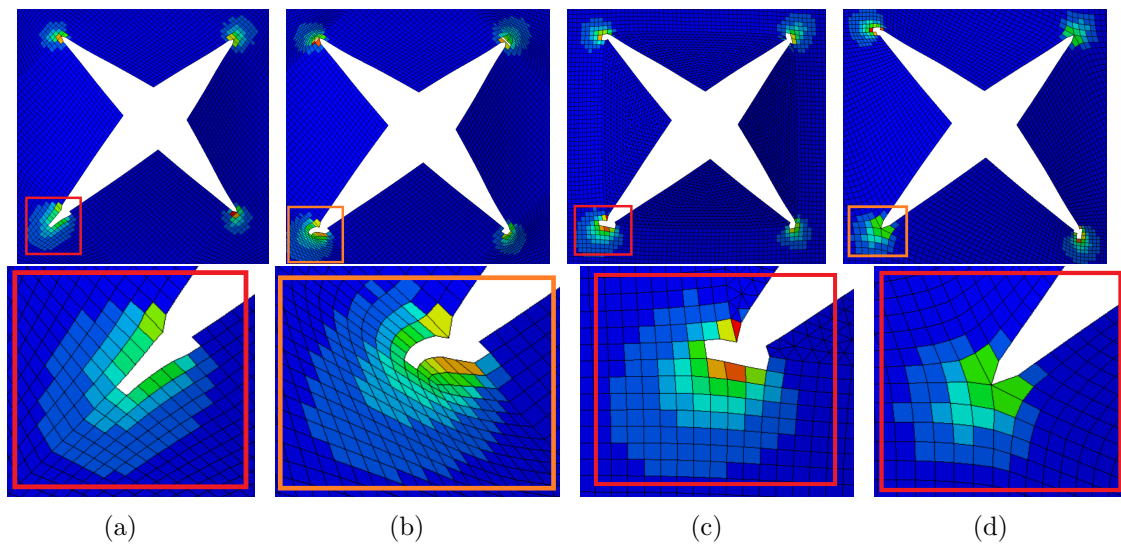


Figure 4.22: Mesh study for crack arrest at 15 bar for the S2 configuration. (a) M1, (b) M2, (c) M3, (d) M4. See Figure 4.2(e) to 4.3(f) for the different mesh geometries.

The different crack propagation patterns obtained through the use of solid and shell elements are deviating noticeably, both in crack-lengths and crack shape. Figure 4.23 shows the crack arrest for the solid-element simulation using three elements through the thickness of the plate. The solid analysis results in considerable cracks in all four corners of the slit. It is important to note that a different mesh geometry was used for the solid analysis, where the mesh is oriented parallel to the outer boundaries.

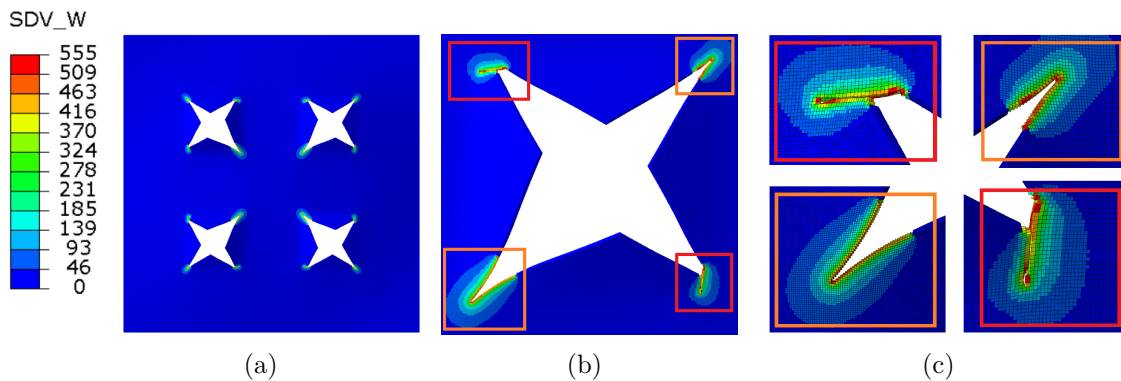


Figure 4.23: Crack arrest at 15 bar firing pressure for S2 configuration using C3D8R elements with an approximate size of 0.26 mm. (a) Shows the entire plate, (b) shows a zoomed image of the modelled slit, and (c) show a collection of all four cracks.

When applying a firing pressure of 25 bar to the simulation using three C3D8R elements across the thickness, the S2 configuration is experiencing complete failure. The propagation initiates as indicated in Figure 4.23. By further crack growth the upper left crack in the symmetric model shown in Figure 4.23(b) is running across

the plate and is responsible for the collapse. The crack propagation until complete failure is shown in Figure 4.24

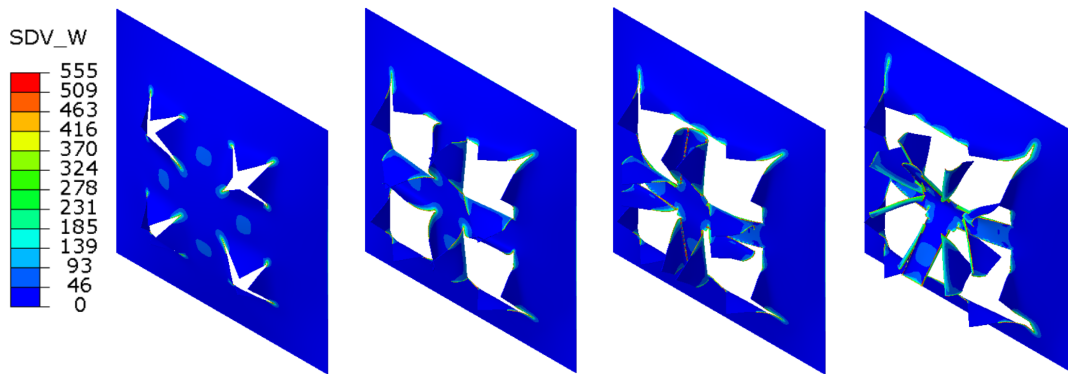


Figure 4.24: Failure mode for S2 at 25 bar using 0.26 mm C3D8R elements.

The simulation results regarding the slit configurations are summarized in Table 4.6. The measured crack length for the S1 configurations is the horizontal crack illustrated in Figure 4.19. For the S2 configurations it is the crack propagating diagonally towards the center of the plate, illustrated in Figure 4.23.

Table 4.6: Mean midpoint displacement and obtained crack lengths for the S1 and the S2 configuration. The measured crack length for the S1 configurations is the horizontal crack illustrated in Figure 4.19. For the S2 configurations it is the crack propagating diagonally towards the center of the plate, illustrated in Figure 4.23.

| Model | Mean displacement [mm] | Crack Length [mm] |
|---------------------|------------------------|-------------------|
| S1_S4R_08_P77_05 | 11.82 | No crack |
| S1_C3D8R_026_P77_05 | 12.04 | 0.79 |
| S1_S4R_08_P77_10 | 19.39 | 0.79 |
| S1_S4R_10_P77_10 | 19.48 | No crack |
| S1_C3D8R_026_P77_10 | 19.24 | 7.30 |
| S1_S4R_08_P77_15 | 24.23 | 12.63 |
| S1_S4R_10_P77_15 | 23.95 | 8.00 |
| S1_S4R_10_P77_15 | 24.02 | No crack |
| S1_C3D8R_026_P77_15 | Failure | Failure |
| S2_M1_P77_10 | 18.08 | No crack |
| S2_C3D8R_026_P77_10 | 17.85 | 5.73 |
| S2_M1_P77_15 | 22.66 | 5.17 |
| S2_M2_P77_15 | 22.73 | 2.95 |
| S2_M3_P77_15 | 22.72 | 2.22 |
| S2_M4_P77_15 | 22.98 | No crack |
| S2_C3D8R_026_P77_15 | 22.58 | 12.16 |
| S2_M1_P77_25 | 28.64 | 19.66 |
| S2_M2_P77_25 | 28.23 | 4.36 |
| S2_M3_P77_25 | 28.42 | 5.07 |
| S2_M4_P77_25 | 29.44 | No crack |
| S2_C3D8R_026_P77_25 | Failure | Failure |

4.3.3 Resulting test matrix

Based on the simulations presented in this chapter, the test matrix seen in Table 4.7 was made. This test matrix is based on the solid element models applying three elements across the thickness, and provides nominal firing pressures associated with three distinct responses; complete failure, crack arrest, and deformation with limited to no cracking.

Table 4.7: Test matrix based on the simulations in the preliminary study. All nominal firing pressures refer to a driver length of 77 cm.

| Configuration | Firing Pressure [bar] | Planned response |
|---------------|-----------------------|--------------------|
| P1 | 5 | Mainly deformation |
| | 10 | Arresting crack |
| | 15 | Total failure |
| P3 | 15 | Mainly deformation |
| | 25 | Arresting crack |
| | 35 | Total failure |
| S1 | 5 | Mainly deformation |
| | 10 | Arresting crack |
| | 15 | Total failure |
| S2 | 10 | Mainly deformation |
| | 15 | Arresting crack |
| | 25 | Total failure |

4.4 Discussion

4.4.1 Element size and formulation

When comparing midpoint displacements for models applying shell elements with a size on the range 0.8 mm to 3.2 mm, no significant changes are observed. The same trend is seen when evaluating solid element models with two, three and four elements across the thickness of the plate. This shows that convergence is reached with respect to midpoint displacements for both element formulations when using element sizes on the given intervals.

Because experimental work conducted by Granum and Løken [29] was available for comparison, the nominal firing pressure needed to obtain failure in the P2 configuration and the corresponding crack lengths was known. With these experimental results as a benchmark, the ability to capture cracking and failure was evaluated for models

using both shell and solid elements. None of the shell element models were able to predict the crack initiation at the critical firing pressure, whereas the solid element models qualitatively reproduced the crack lengths seen in the test. Regarding the failure load, the solid element model applying three elements across the thickness was able to predict complete failure of the plate. For the equivalent loading, the shell element model with 0.8 mm predicted only minor cracking. It was found that shell elements give an idea of the capacity, but to verify it is necessary to apply a solid element analysis.

Based on the findings in the benchmark study, it was decided to use an iterative technique to identify nominal firing pressures for the test matrix. The first step was to run simulations on all new configurations using 0.8 mm S4R elements. If the result contained elements close to the limit for the Cockcroft-Latham damage parameter, the second step was to re-submit the simulation using 0.26 mm C3D8R elements. The solid element analysis determined whether to expect complete failure or not. By applying this procedure, it was possible to cost-efficiently determine the critical pressures for all new configurations.

An important observation was the lack of convergence in crack-length with respect to element size when using solid elements. At the critical firing pressure analyses applying two, three and four elements across the thickness resulted in observed crack-length of 4.5 mm, 11.38 mm and 18.7 mm respectively. In general, cracking is a very local and small-scale phenomenon. To describe the crack propagation properly, four elements across the thickness is probably not a sufficiently fine discretization. However, a further refinement of the mesh was considered computationally too costly. A comprehensive study of crack behavior is considered to be outside the scope of this thesis as the main goal was to learn how different element types, combined with the Cockcroft-Latham fracture criterion affected the results.

By comparing the experimentally obtained crack-lengths to the numerical results for the P2 configuration, the model applying three elements across the thickness gave the best results. The implementation of a fixed boundary does not allow any sliding or rotations, which is assumed to be too strict and reduce the capacity of the plates. In addition, the applied loading curves are taken from measurements on rigid plates[3]. This results in a higher loading than what is found for a deformable plate at a corresponding nominal firing pressure. It might be that these two effects are compensated for by the coarse discretization of the structure.

4.4.2 Structural response

Perforated configurations

The P1 configuration is found to have a greatly reduced failure capacity compared to the P3 and P2 configuration. Placing the perforation in the center of the plate makes the corners of the perforation exposed to high strains as the plate lose the ability to

transfer membrane forces across the center of the plate.

In contrast to P1, the P3 configuration distribute the damage over a larger area in the plate because of its evenly spread perforations. This increase the capacity by allowing the midpoint to experience large displacement before the plate fails. Compared to P2, the P3 configuration responds with larger displacements for all applied pressures, but as both configurations fail for the same maximum pressure it is hard to distinguish the capacities due to the limited selection of available pressure-time curves.

Regarding the failure mode predicted for the P3 configuration, the expected failure mode could be highly sensitive to geometrical- and material imperfections. Because there are as many as 16 perforations in the P3 configuration, there are many areas of stress concentration where crack propagation can initiate.

Slitted configurations

For the S1 and S2 configurations, no direct comparison was available, but the models have been compared to the results obtained for the similar slit geometries using aluminum instead of steel, in [30]. Note that the aluminum plates had a thickness of 1.5 mm. When compared, the failure modes show good agreement. The greatest challenge for the slit geometries was the angled slits of the S2 configuration. The 45° difference in orientation between the slits and the outer boundary makes it possible to mesh the plate in different ways. The mesh study carried out in this configuration showed that both the initiation and propagation of the cracks are highly dependent on element size and mesh orientation. When using shell elements, four different meshes gave four different crack-arrest shapes. Due to the high computational costs for solid element analyses, only one mesh orientation was tested. The latter implies that there is still some uncertainty related to the mesh dependency in this model.

4.4.3 Comparison to other numerical studies

The simulated midpoint displacement, using the simple model, is lower than the experimentally obtained values by Granum and Løken. When comparing with equivalently simplified studies done in the master thesis by Granum and Løken[29] and by Aune[3], the trend is the opposite. A plausible explanation for this observation may be that these studies applied slightly different material properties Aune [3].

Chapter 5

Preliminary study part II

Based on the knowledge obtained in Chapter 4, this chapter aims to investigate more realistic Lagrangian models of the problem. This is done by replacing the fixed boundary conditions of the blast-exposed area with a numerical model of the clamping frames in the SSTF. The effect of varying the strain rate sensitivity and include adiabatic heating will be investigated. This part is further intended to act as a final benchmark study, before applying the most complex model to the new configurations.

5.1 Description

This part of the thesis includes two different models. The first is a continuance of the simplest models described in Chapter 4, with the only modifications being changes in the strain rate sensitivity parameter and the inclusion of adiabatic heating. The second model is geometrically more complex, including the clamping frame and bolts. The loading is modeled in the same way as in Chapter 4. By including more parts in the assembly, a higher number of elements are required as well as the modeling of contact. This results in a significant increase in computational costs.

As stated in Chapter 4, the strain rate sensitivity study is included as the numerical results differed slightly between this thesis and previous work done at NTNU. Work done by Aune[3] showed that both introducing perforations, and allowing for deformations in the plates reduce the pressure build-up when compared to the massive steel plates. This finding indicates that the loading applied in the pure Lagrangian simulations are conservative. It is therefore expected that the response will be overestimated in the pure Lagrangian simulations when comparing to experimental observations. It is considered important to find a combination of friction and strain rate sensitivity that obey the findings from Aune.

Tuning of parameters to obtain the desired results is a bad habit when doing FEM-analysis. This being said, the modeling of friction is a challenging task if doing it accurately. The same goes for the strain rate sensitivity for the Docol 600DL steel.

Rakvåg [27] investigated the strain rate sensitivity experimentally for this steel in conjunction with his PhD thesis by performing split Hopkinson tension bar tests at different strain rates. The tests were conducted on 2 mm thick plate material and suggest that the strain rate sensitivity parameter c , described in Eq.(3.21), was dependent on the level of plastic strain. By fitting the modified Johnson-Cook equation to the experimental data for plastic strain levels of 5%, 8% and 12% it resulted in three different values of the strain rate sensitivity parameter; 0.026, 0.015 and 0.01 respectively.

The parameters applied in the models of the new configurations will be based on the parametric study in this chapter. The results when running these models are included in Chapter 7, and only the FP and the P2 configuration are considered in this chapter.

5.2 Models

In addition to the general naming format presented in Chapter 4, some additional information regarding the models is added. For the complex models, the name label will include CX. These models introduce the need of modeling friction, and the applied friction coefficient is added as fxx. Here xx is the friction coefficient, and the notation f03 refers to a coefficient of 0.3. For simplicity, it is assumed that one single frictional coefficient is valid for all parts interacting in the entire assembly. For both the simple and the complex model the strain rate sensitivity parameter c is given at the end of the name as cxxxx, where c0001 refers to this parameter being set to 0.001. The initial value used for this parameter in the first part of the study was 0.01, and when cxxxx is not part of the legend, it implies that the initial value was used. The last addition to the naming format is a T at the end of the label if adiabatic heating were included in the simulation.

5.2.1 Complex model

Figure 5.1 shows an illustration of the modeled assembly. The assembly has two clamping frames, a red side, and the blue side. The loading is applied to the blast-exposed area of the plate on the blue side, and it is the clamping frame marked with blue that is the thickest. In the actual experimental setup, the blue plate would have consisted of two separate plate structures with a thickness of 25 and 50 mm. For simplicity, it is modeled as a single plate with a thickness of 75 mm. This is done to exclude one set of contacts from the simulation. The assembly consists of four bolts, where the grey bolts are split in half for symmetry reasons. The assembly is held in place by fixing all degrees of freedom at the surface marked in egg-white. Initially, it was planned to create the model without fixing the entire backside of the thick plate, and to use the built-in bolt-load-feature in Abaqus to pre-load the bolts. Unfortunately, this feature is only available for the implicit solver, and transferring results between jobs with different solution algorithms was found cumbersome. The

possibility of using a temperature gradient to shrink the bolts, giving the desired pre-tension was also considered. It was decided not to use this method as the model contain a large number of elements, and that this approach calls for an iterative technique to reach exact force levels.

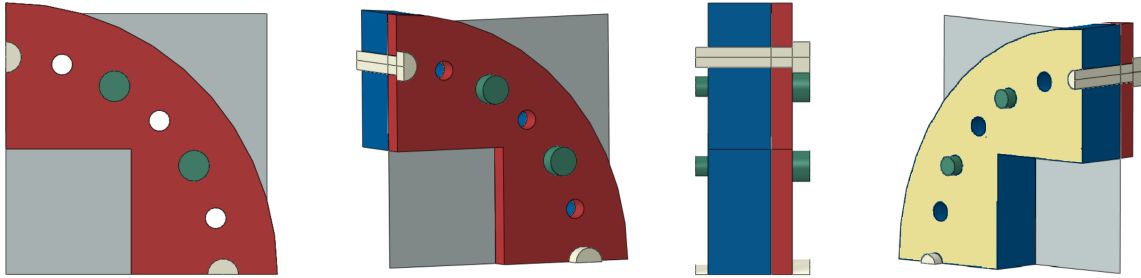


Figure 5.1: Illustration of the complex model

The advantage when fixing the back side of the thick fastening plate is that it allows for the bolt force to be applied directly to the side of the bolt opposite to the bolt head. This implies the assumption that the clamping plates with the combined thickness of 75 mm are considered magnitudes stiffer than the 0.8 mm steel plate that is exposed to the shock wave.

The analysis was therefore divided into two separate steps. First a bolt tightening step, and second the pressure loading of the blast-exposed area. The bolt tightening step applied mass scaling with a factor of 100 to speed up the simulation and was doable because this part of the behavior does not include any important dynamic effects. The bolt traction was applied as a smooth step function to further minimize any dynamic effects. At the beginning of the loading step, the free ends of the now elongated bolts were fixed, and the bolt load was turned off. This was done to ensure that the bolts now held the plates in place by its elastic deformations only and that the contact force was governed by the pre-tension load in the bolts.

To calculate the pre-tension in the bolts, previous work by Aune [3] [49] was considered. The calculation is based on measuring the approximate torque at which the bolts are tightened, and estimating of the effect of friction based on material parameters and thread geometry. This calculation estimates the pre-tension force in each bolt to be 46.5 KN and is the force applied as a surface traction to the end of the bolts in the model.

To model the friction, the simple Coulomb frictional model, as described in [20] will be applied. Both the static and the dynamic frictional coefficient will take the same value. Generally, these two values differ, but no experimental data regarding the frictional behavior is available for comparison. Because of this, it is considered cumbersome to include both in the parametric study.

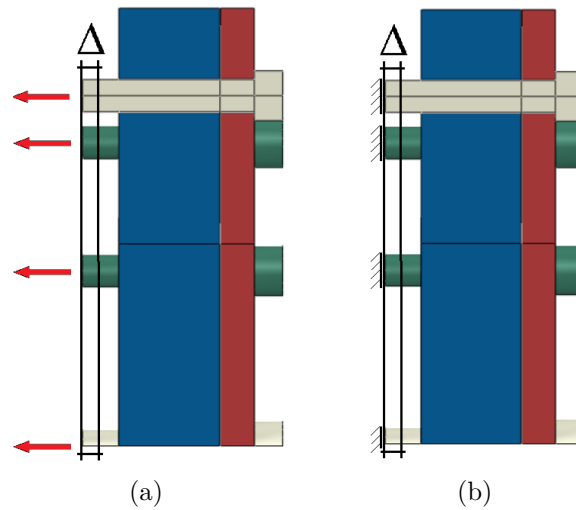


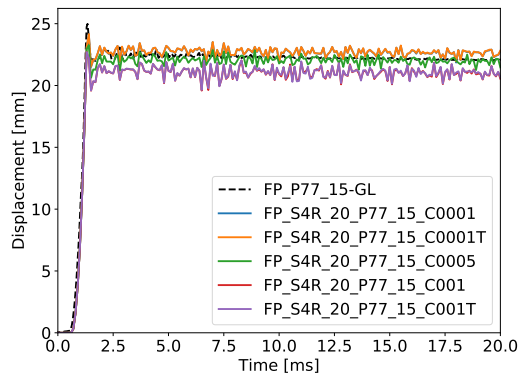
Figure 5.2: The bolts being tightened and fixed in the two steps. (a) showing the load being applied and (b) shows the fixing of the bolt ends.

5.3 Results

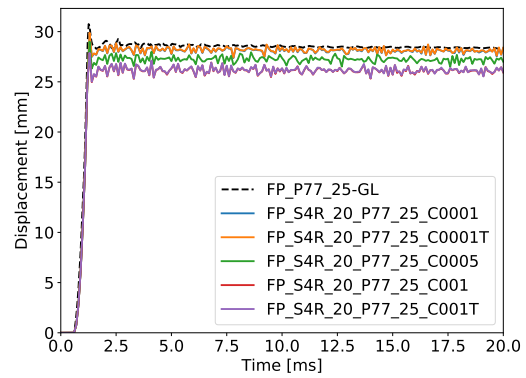
In this section the results of varying the strain rate sensitivity, including adiabatic heating, and varying the friction coefficient is presented. For the models investigating the strain rate sensitivity, only the geometrically simple boundary conditions are applied.

5.3.1 Effect of rate dependency and thermal softening

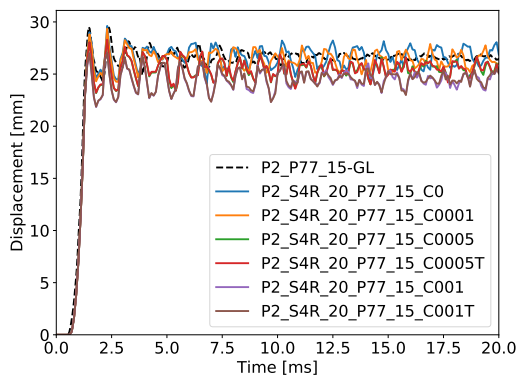
From the plots given in Figure 5.3 it is observed that a change of the strain rate sensitivity parameter c is affecting the behavior of the plates noticeably. As expected, a reduction of the strain rate sensitivity gives a softened material behavior. When comparing the average midpoint displacement for the results obtained in this section, the greatest change is found for the P2 configuration when exposed to a firing pressure of 25 bar as seen in Figure 5.3(d). Here the average midpoint displacement is experiencing an increase of 9.75% when changing c from 0.01 to 0.001. For the FP configuration exposed to both 25 bar and 15 Bar, and the P2 configuration exposed to 15 bar the change of c from 0.01 to 0.001 gives an increase of midpoint displacement in the range 7.59 to 7.78%. The effect of including adiabatic does not affect the results noticeably.



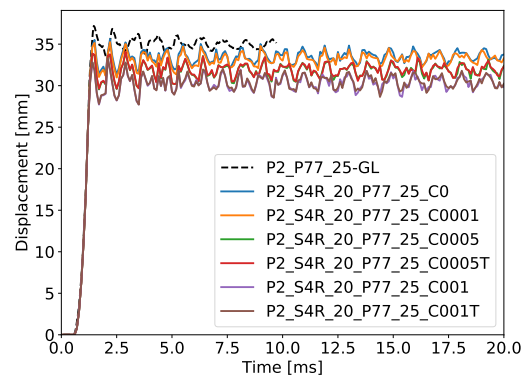
(a)



(b)



(c)



(d)

Figure 5.3: Midpoint displacement response vs. time is plotted for changes in strain-rate sensitivity and by including adiabatic heating. (a) FP at 15 bar, (b) FP at 25 bar, (c) P2 at 15 bar and (d) P2 at 25 bar

The results also suggest that the fracture behavior is dependent on the strain rate dependency parameter c . Figure 5.4 are obtained by running three clamped solid element analyses using 0.26 mm C3D8R elements, a firing pressure of 25 bar, and varying the strain rate dependency as $c=0.01$, $c=0.005$ and $c=0.001$. A decrease in c from 0.01 to 0.005 increases the crack-length at the center from 11.08 mm to 17.36 mm and the midpoint displacement from 30.55 mm to 32.54 mm. When running the analysis using $c=0.001$ the model is experiencing a complete failure. It is also worth noting that none of the 2 mm S4R shell element analyses with a decreased strain rate sensitivity are experiencing any crack initiation at the firing pressure of 25 bar.

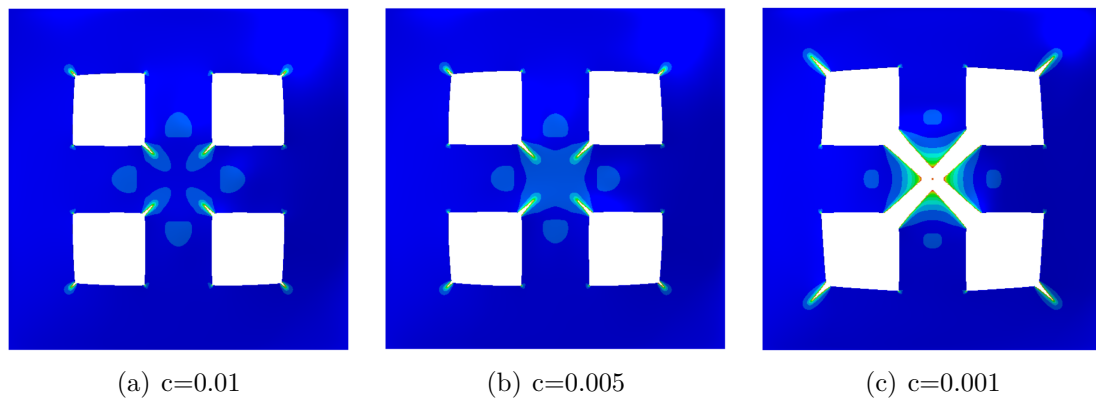


Figure 5.4: Crack propagation at 2 ms for the simple solid element model with an element size of 0.26 mm at the strain rate sensitivities given in (a) to (c).

5.3.2 Effect of friction

The effect from varying the frictional number seems to effect the response for the full plates more than the P2 configuration, as indicated in Figure 5.5 and 5.6. The FP configuration shows a softer behavior for all simulations, except for one, while P2 only overestimates the response for the friction-less analysis. For the firing pressure of 15 bar, a change in the friction coefficient from 0.16 to 0.3 for P2, results in an increase in midpoint displacement of 9.31%. The same change for the full plate gives an increase of 18.97%.

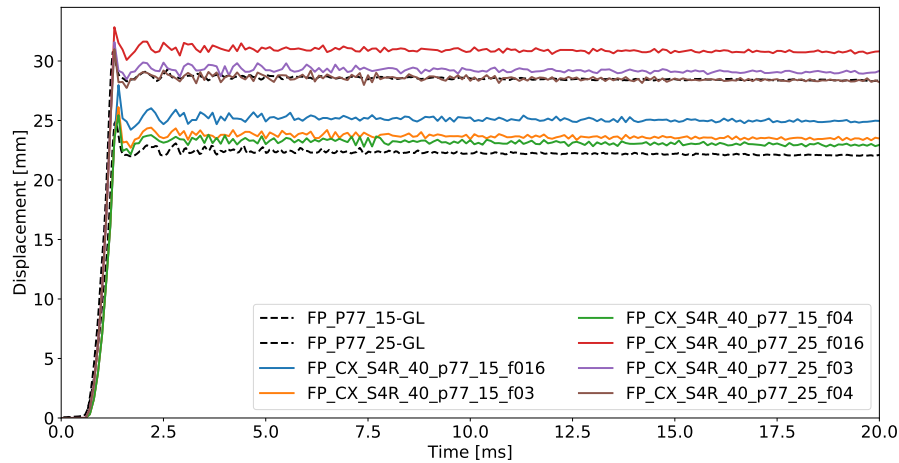


Figure 5.5: The resulting midpoint displacements from varying the friction coefficient for the FP configuration.

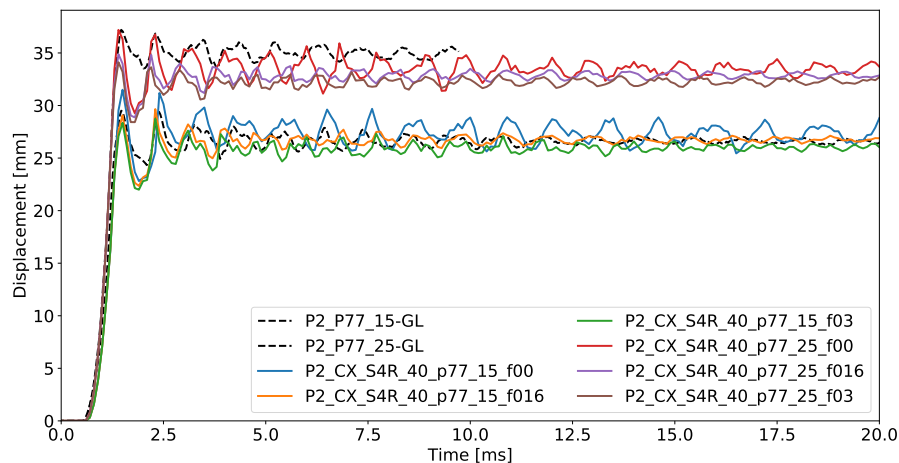


Figure 5.6: The resulting midpoint displacements from varying the friction coefficient for the P2 configuration.

From Figure 5.5 and 5.6 it is seen that the geometrically more complex models experience less oscillations than the models applying fixed boundary conditions. However, this is only the case for a non-zero frictional coefficient.

Regarding the energy calculations in the model; the contact energy, total energy, and the artificial energy are included in the appendix. For all models, these energies were within the acceptable range, but are included for consistency.

5.4 Concluding remarks

When investigating the effect of lowering the strain rate sensitivity parameter, it is evident that this noticeably changes the response. A lower value both increase the obtained midpoint displacement and increase the crack lengths. In his numerical work, Rakvåg chose to neglect the strain rate sensitivity [27]. This was justifiable because a parametric study on this parameter showed marginal effect, probably due to lower strain rates in his experiments. Neglecting it in this study is not an option as it clearly affects the results. When it comes to introducing or excluding adiabatic heating the effect is negligible, due to low temperature development. This is in compliance with the previous work done at NTNU.

To settle on a friction coefficient turned out to be complicated as the FP and the P2 configurations responded quite differently to the changes in this parameter. Although the two configurations responded differently, it was decided to choose a friction coefficient that worked well for the P2 configuration. This was done because all the new configurations include either slits or perforations, and in that sense, differ more from the full plate configuration than the P2 configuration.

For the coming models, the strain rate parameter is chosen to be $c=0.005$. This is the same value as Granum and Løken apply in their thesis [29], which makes comparison easier. Based on the parametric study, the frictional coefficient is chosen to be 0.16. This is a typical value seen in engineering handbooks for steel-steel friction [50], applying to lubricated or greased surfaces. In the tests, the surfaces interacting are indeed not clean due to spray-painting for 3D-DIC, but it is important to be aware that the chosen coefficient is not determined by actual testing.

Chapter 6

Experimental work

In this chapter, the experimental setup and results will be presented. The experiments conducted and presented are the test matrix presented at the end of Chapter 4.

6.1 Experimental setup

The experimental setup will include a description of the shock tube and the equipment used to document the experiments. This includes the DIC technique, laser scanning equipment and the setup of pressure sensors.

6.1.1 The SIMLab shock tube facility

All experiments are performed in the SIMLab Shock Tube Facility (SSTF) at CASA, NTNU. This test facility is thoroughly described and validated by Aune [3], but will be presented briefly in this section for completeness. The SSTF is designed to create shock waves in air and allows for both the shock wave phenomenon and the corresponding response of structures to be studied. To monitor experiments, the facility is equipped with two high-speed cameras and several pressure sensors for a synchronized sampling of data.

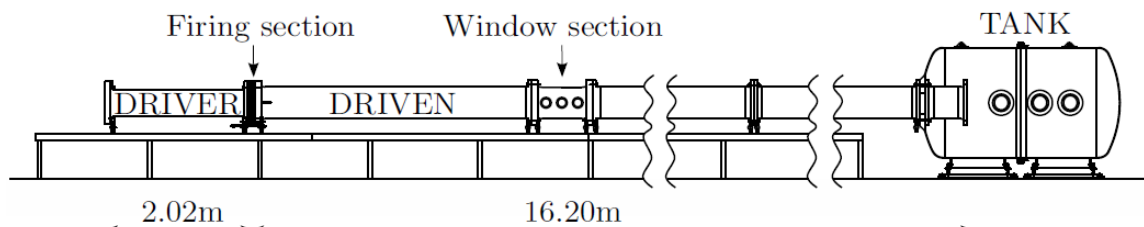


Figure 6.1: Illustration the SSTF. The different sections, as well as the dimensions is shown. Image is taken from [3].

When including the tank, the total length of the tube is 20 m. It consists of four main sections: the driver section, the firing section, the driven section, and a dump tank.

Driver section

This is a high-pressure chamber, with a inner diameter of 31.1 cm and is pressurized prior to the release of the shock wave. The total length of this section is 2.02 m and by the use of aluminum inserts, the length of the driver may be varied. All experiments in this study apply a driver length of 77 cm.

Firing section

This section is located downstream the driver and has a length of 14 cm. The firing section serves as the divider between the high-pressure side (driver) and the low-pressure side (driven). In order to get a stepwise transition from high to low pressure in the firing mechanism, this section allows for three separate membranes giving two intermediate pressure chambers between the high- and low-pressure side. Different firing pressures are obtained by varying the rupture strength of the membranes in this section.

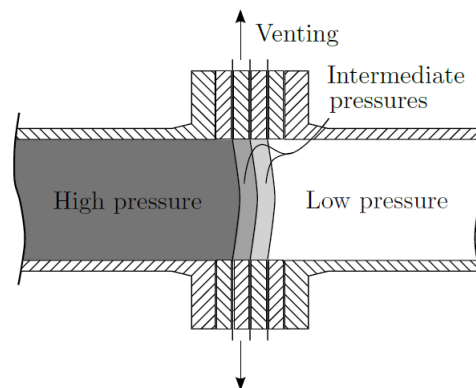


Figure 6.2: Illustration showing the driver, firing section and driven section. The image is taken from [3].

Driven section

The cross-section of both the driver and the firing section are circular, while the cross-section in most of the driven section is squared. The driven section has a total length of 16.2 m and the first 0.6 m of this section serves as a transition between the two different cross-sections. The blast-exposed plates are mounted in the downstream end of this section. This part of the shock tube also contains an area with windows,

where it is possible to mount test objects, but this feature has not been utilized in this work.

Dump tank

The dump tank encapsulates the end of the driven section where the blast-exposed plates are being mounted. The tank has a large volume, and the significant increase in volume from the driven section to the dump tank ensure a drop in pressure. The tank act as a protection from dust and fragments, furthermore windows are installed to enable view for the high-speed cameras.

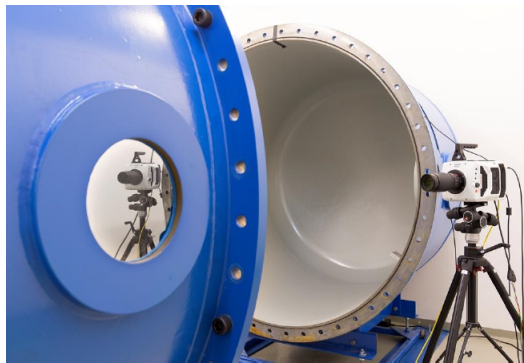


Figure 6.3: Showing the two high-speed cameras outside the dump tank. The image is taken from [3].

Initiation of the shock wave

The process starts by gradually filling the driver section and the intermediate pressure chambers with compressed air until the desired firing pressure is obtained. The mechanical explosion is set off by manually releasing the pressure in the intermediate chambers, causing the membranes to rupture. First, the wave is transformed from the circular cross-section to the squared cross-section. By the time the shock wave hits the blast exposed plate, the rarefaction waves have caught up with the shock wave, which results in a uniform shock front very similar to what is found for an far field detonation. This has been verified by Aune in [4].

6.1.2 Measuring equipment and calibration

During the blast event, the two Phantom v2511 high-speed cameras placed outside the windows of the dump tank are sampling pictures of the plate at a frequency of 37 kHz. The pressure is sampled in several sensors along the inside of the tube at a frequency of 500 kHz. The pressure data is also extracted at the same rate as the pictures taken by the high-speed cameras, so each image pair is linked to a pressure level. The synchronization of the pressure data and pictures makes it possible to define a common time axis when post-processing the results. Since the distance between each sensor is known it is also possible to calculate the velocity of the shock

wave propagating towards the testing plate. The two pressure sensors closest to the plate is placed 24.5 cm and 34.5 cm upstream of the plate, respectively.

6.1.3 Plate setup

All plates have a total area of 0.625 m x 0.625 m and a blast-exposed area of 0.3 m x 0.3 m, which corresponds to the cross-sectional area of the driven section. All plates tested has a thickness of 0.8 mm and are made of the material Docol 600DL. The plates are mounted between two thick steel plates with dimensions given in Figure 6.10. The clamping frames are fastened using 12 M24 bolts evenly distributed. All bolts are tightened using a torque wrench at 200 Nm.

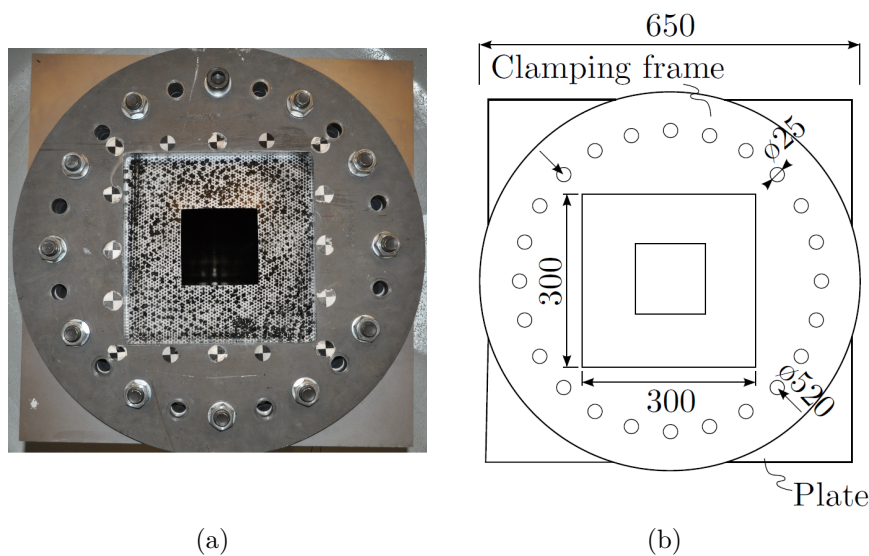


Figure 6.4: Illustrating the clamping frame used for clamping of plates in the shock tube. (a) Showing the P1 configuration mounted in the clamping frame and (b) dimensions of the clamping frame.

Prior to testing, all plates are spray painted with a random speckle pattern to enable post-processing with 3D-DIC. This technique is described further in the section below. When spray painting the plates, it is desired to keep the area covered by the supports as clean as possible for a more predictable friction in the system. The painting is being done manually with spray cans. This cause the amount of paint covering the plates inside the clamped area to vary quite a lot, implying that the friction in the system possibly differs between tests.

6.1.4 Three-dimensional digital image correlation

Digital Image Correlation (DIC) is a technique used to measure displacements and strains or to track points and edges. The method is based on tracking points on the outer surface of an object, and the points are tracked in a series of images of

the deformation process. For the blast-exposed plates, this is done through tracking the random speckle pattern. The DIC-analysis is run in the eCorr software, which is developed at NTNU, and a detailed documentation is available at [51]. In order to obtain 3D-fields, at least two cameras are needed, and both cameras need to capture the same point at the same time. Each tracked point is described by two coordinates, one for each camera. By taking the angles between the cameras and the plates into account, these four coordinates can be translated into three spatial coordinates (X , Y , Z). To obtain field data, a mesh is paired with the two first images of the undeformed geometry. Throughout the deformation process, the eCorr-software is using the grey scale values of the new images to adapt the original mesh to the images of the deformed geometry. To describe the fields, an FE formulation using Q4 elements are being applied. When applied to the experimenters, both the clamping frame and the blast-exposed plate is tracked. This is done because the entire shock tube setup is free to move, and it is the relative displacement between the plate and the clamping frames that are of interest. To track a chosen set of points on the surface of the clamping frame, it is covered with the checkerboard stickers seen in Figure 6.5(a).

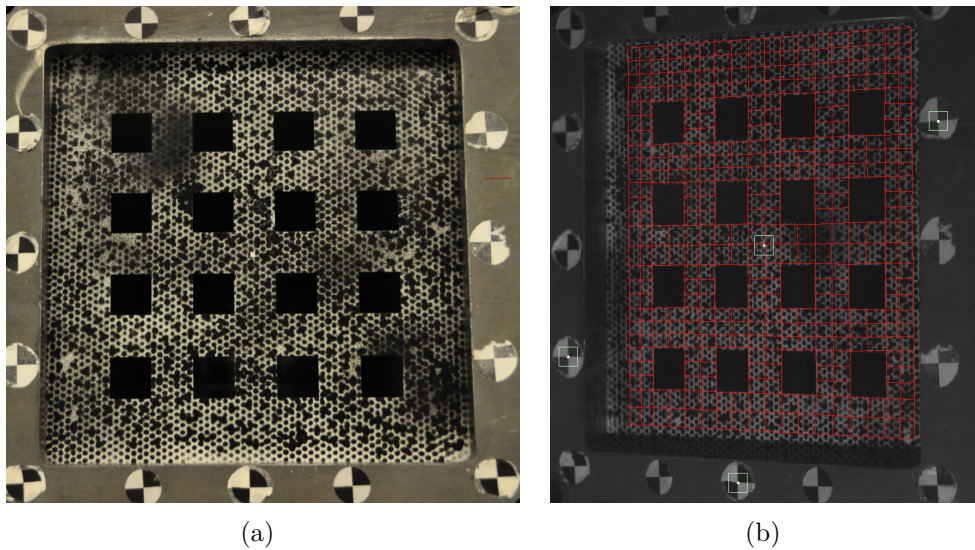


Figure 6.5: The P3 plate clamped in the SSTF prior to testing. (a) shows the applied speckle pattern for 3D-DIC analysis and (b) shows the applied mesh, and subsets for point tracking in 3D-DIC.

6.1.5 Laser scanning

In addition to the DIC measurements of the blast-loaded plates, laser measurements of both the deformed and undeformed plates have been performed. For these measurements, the Romer Absolute Arm 7525SI delivered by Hexagon Manufacturing Intelligence was used. The Absolute Arm is a portable laser measuring arm which allows for the blast loaded plates to be measured while they are still mounted in the shock tube after the test, and the measuring conditions will, therefore, be as similar as possible to the results obtained from DIC. The first step in the measuring procedure is to manually define a zero-plane for the measurements. When this plane is determined the plate is scanned and the surface of the deformed geometry is being discretized into a point cloud which can be extracted as a .txt-file for further processing. The technical specifications for the Absolute Arm 7525SI state that it has a point repeatability of 0.02 mm. The point repeatability is defined by measuring one single point from multiple directions. More technical details can be found in [52]. The laser scanning process conducted after each test is illustrated in Figure 6.6.

The point-clouds obtained from the laser measurements were post-processed in MATLAB. A filtering script was used to remove unnecessary points and to visualize the data, the cloud is plotted for a 1 mm x 1 mm mesh using second order interpolation.

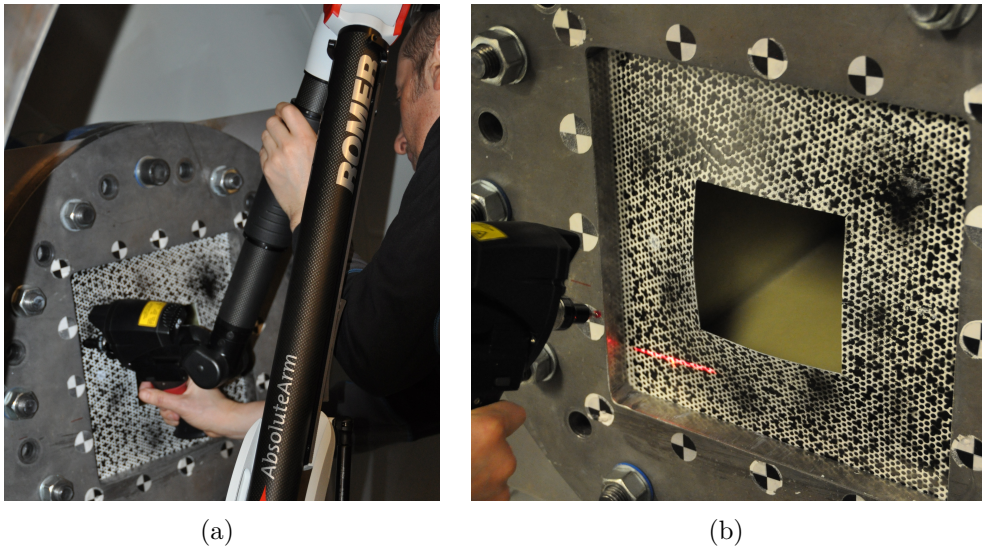


Figure 6.6: The scanning process of a P1 plate after testing. (a) shows the Romer Absolute Arm and (b) shown the probe while scanning a plate.

6.2 Experimental results

The obtained experimental results will be presented in the following order:

- Post test images
- Pressure-time curves
- Midpoint displacements
- Deformation profiles
- Laser scanning and final deformation profiles by DIC and laser
- Failure modes
- Cracking

In Table 6.1 the executed test matrix is given. This matrix differs slightly from the pre-planned test matrix as it contains one additional nominal firing pressure for the P1 configuration at 25 bar. The inclusion of one extra test for the P1 configuration was possible as a misunderstanding resulted in extra plates being produced for this configuration. The exclusion of the P3 configuration at 15 bar is due to a premature firing of the system, leaving no usable test data. Table 6.1 together with the images taken after the tests, presented in Section 6.2.1, gives a compact summary of the structural response observed experimentally.

Table 6.1: The experimentally executed test matrix with a short summary of the experimental response of the tested configurations. All nominal firing pressures refers to using a driver length of 77cm.

| Configuration | Firing Pressure [bar] | Summary of Response |
|---------------|-----------------------|---------------------|
| P1 | 5 | No crack initiation |
| | 10 | Crack initiation |
| | 15 | Crack initiation |
| | 25 | Total failure |
| P3 | 25 | Crack initiation |
| | 35 | Total failure |
| S1 | 5 | Crack initiation |
| | 10 | Crack initiation |
| | 15 | Total failure |
| S2 | 10 | Crack initiation |
| | 15 | Crack initiation |
| | 25 | Close to failure |

6.2.1 Post test images

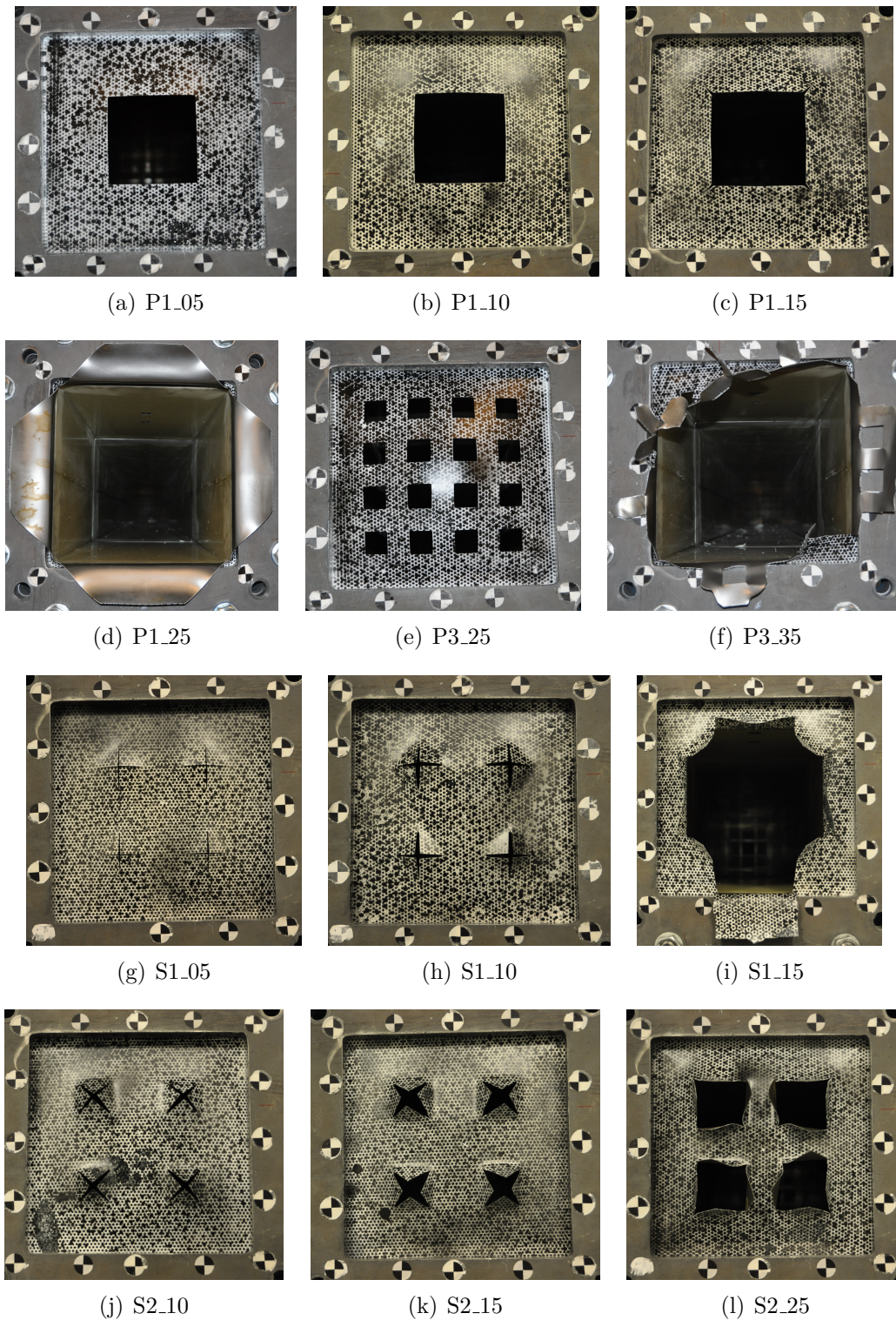


Figure 6.7: Post test images of all successfully conducted experiments in this thesis. For every image, the configuration and the nominal firing pressure applied in the experiment is given. All nominal firing pressures refers to using a driver length of 7.7cm, and firing pressure is given i bar.

6.2.2 Pressure-time data

Pressure-time plots for all experiments conducted in this study are given in Figures 6.8(a) - 6.9. In addition to the data obtained through work with this, older test data are included as a basis for comparison. Data included are from the calibration experiments conducted with the massive steel plate [3] and from experiments with the FP and the P2 configuration [29]. The only new addition to the naming convention is: Cal, used for the calibration experiments.

In the pressure-time plots, only the positive part of the pressure phase is included. The measurements are taken from the closest pressure sensor, 24.5 cm upstream the plate. The presented data is filtered using a moving average approach, as this makes the data easier to visually inspect.

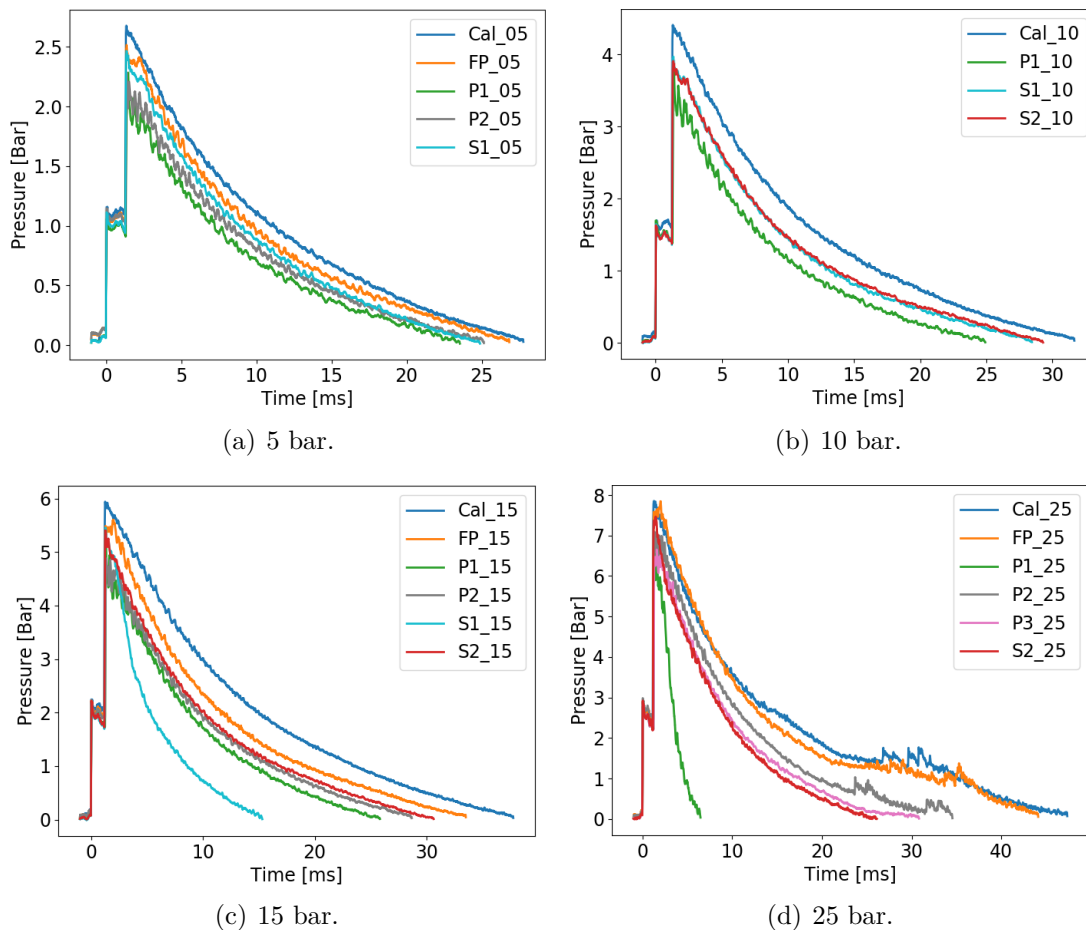


Figure 6.8: Reflected pressure measured at the pressure sensor 24.5 cm upstream the plates in the SSTF.

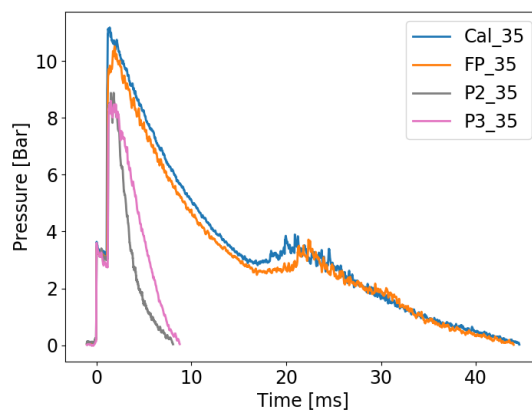


Figure 6.9: Reflected pressure measured at the pressure sensor 24.5 cm upstream the plates in the SSTF. Included are all test with nominal firing pressure of 35.

Important note: all curves are shifted to define time equal to zero as the incoming pressure wave passes the sensor closest to the plate. This point is seen as the first sudden peak in the pressure, which keeps approximately constant until the reflected pressure arrives at the sensor seen as the maximum peak in the plots. This is important because the displacement data and the pressure data are synchronized for each individual test, resulting in the displacement data to be shifted equally much as the corresponding pressure-time curve, and that the two sets of data are related to the same reference point in time.

From the pressure-time data, it is seen that for the experiments experiencing collapse, the reflected pressure experience a drop in pressure after the initial peak as the air is released into the dump tank. This is observed for the following tests: S1.15, P1.25, P2.35, and P3.35.

As a tool to inspect the pressure-time data, Table 6.3 is given. With this table, it is easy to inspect and compare the peak reflected pressures. It is evident that different plate configurations give a noticeable change in the pressure build-up in front of the plate, compared to the calibration experiments. The table is sorted by nominal firing pressure, and within these groups, rows are sorted by the value of measured peak pressure. The two columns named Deviation contain the deviation between the measured peak pressures for different plate configurations compared to the calibration results for equal nominal firing pressures. This is an important comparison as it gives an indication of how the structural response of the tested plates reduces the pressure build up in front, compared to a nearly rigid surface. For experiments where the plates failed, data are written in italic in Table 6.3.

6.2. Experimental results

Table 6.3: Measured peak reflected pressure and the positive duration of the blast wave, measured at the sensor 24.5cm away from the blast exposed plate. The listed deviations are measured relative to the calibration plate experiments for equivalent firing pressures.

| Experiment | Peak reflected | Positive | Deviation [%] | Deviation [KPa] |
|--------------|-------------------|------------------|------------------|--------------------|
| | pressure [KPa] | duration [ms] | | |
| Cal_05 | 276.8 | 26.4 | - | - |
| FP_05 | 267.4 | 25.5 | -3.4 | -9.4 |
| S1_05 | 259.6 | 23.5 | -6.2 | -17.2 |
| P2_05 | 240.5 | 23.8 | -13.1 | -36.3 |
| P1_05 | 234.9 | 22.1 | -15.1 | -41.9 |
| Cal_10 | 456.2 | 30.3 | - | - |
| S1_10 | 415.9 | 27.1 | -8.8 | -40.3 |
| S2_10 | 411.9 | 28.0 | -9.7 | -44.3 |
| P1_10 | 399.7 | 23.6 | -12.4 | -56.5 |
| Cal_15 | 613.0 | 36.5 | - | - |
| FP_15 | 575.0 | 32.2 | -6.2 | -38 |
| <i>S1_15</i> | <i>574.0</i> | <i>14.0</i> | <i>-6.4</i> | <i>-39</i> |
| S2_15 | 570.7 | 29.4 | -6.9 | -42.3 |
| P1_15 | 520.0 | 24.5 | -15.2 | -93.0 |
| P2_15 | 498.2 | 27.3 | -18.7 | -114.8 |
| Cal_25 | 817.8 | 46.1 | - | - |
| FP_25 | 789.6 | 42.1 | -3.4 | -28.2 |
| S2_25 | 746.5 | 24.7 | -8.7 | -71.3 |
| P2_25 | 732.2 | 33.2 | -10.5 | -85.6 |
| <i>P1_25</i> | <i>702.3</i> | <i>5.2</i> | <i>-14.1</i> | <i>-115.5</i> |
| P3_25 | 673.7 | 29.2 | -17.6 | -144.1 |
| Cal_35 | 1137.1 | 43.3 | - | - |
| FP_35 | 1055.9 | 42.0 | -7.1 | -81.2 |
| <i>P2_35</i> | <i>901.5</i> | <i>6.6</i> | <i>-20.7</i> | <i>-235.6</i> |
| <i>P3_35</i> | <i>873.0</i> | <i>7.4</i> | <i>-23.2</i> | <i>-264.1</i> |

When inspecting Table 6.3, it is evident that the S1 and S2 configuration are consistently closest matched to the results from the calibration experiments. This when considering the new plate configurations tested in this thesis. Not surprisingly the experiments regarding the full plates are closest to the calibration plate experiments for all tests. From Table 6.3 it is seen that the order of the different configurations is not consistent between the groups of nominal firing pressure. For the 5 bar tests, P2 deviate less from the calibration tests than the P1 configuration, but for the 15 bar tests, P1 deviate less than P2. At 25 bar, it changes again. When evaluating the two highest firing pressures, the P3 configuration is consistently deviating most from the calibration experiments. Unfortunately, data for this configuration are missing for the 15 bar test due to the premature firing of the system.

In Table 6.2, the mean value of the group deviations from the calibration experiments are given, and also the variance within the groups. The variation in the S1, S2 and the P1 group takes very similar values and are low compared to the other groups. The group with the P2 configuration tests stand out as the group with the highest variation. For all the perforated configurations, the mean value of deviation is considerably high, when compared with the slitted perforations.

Table 6.2: Variance and mean value of the deviation in reflected peak pressure for each configuration group. The deviation is calculated relative to the calibration experiments at equivalent loading pressures.

| Group | Variance [KPa] ² | Mean [KPa] |
|-------|--------------------------------|---------------|
| FP | 2.7 | 5.0 |
| P1 | 1.3 | 14.2 |
| P2 | 16.9 | 15.8 |
| P3 | 7.8 | 20.4 |
| S1 | 1.4 | 7.1 |
| S2 | 1.3 | 8.4 |

6.2. Experimental results

In Table 6.4, the shock wave velocities for the different experiments are given. The exception is for the S2 configuration at 25 bar, due to poor data sampling. Grouped after nominal firing pressure, the mean shock wave velocity and the time it takes for the wave to reach the plate after passing the closest sensor is also given. The velocity calculations are based on knowing the distance between the two pressure sensors closest to the plate. Based on the velocity estimate, the time consumed by the wave before reaching the plate is calculated. It is seen that higher nominal firing pressures result in higher supersonic wave speed, an observation that obeys the theory elaborated in the PhD thesis by Aune[3]. The wave speed is of importance as all experiments are chosen to have the same reference on the time axis, namely the point in time when the incoming wave passes the pressure sensor closest to the plate. This will be further discussed in the section on midpoint data.

Table 6.4: The shock wave velocity, mach number and an estimate of the time it takes the wave to travel the 24.5cm between the closest pressure sensor and the blast exposed plate.

| Experiment | Velocity [m/s] | Mach number [-] | Mean velocity [m/s] | Δt [ms] |
|------------|-------------------|--------------------|------------------------|--------------------|
| P1.05 | 458.7 | 1.34 | 460.9 | 0.53 |
| S1.05 | 463 | 1.35 | | |
| P1.10 | 510.2 | 1.49 | 510.2 | 0.48 |
| S1.10 | 510.2 | 1.49 | | |
| S2.10 | 510.2 | 1.49 | | |
| P1.15 | 561.8 | 1.64 | 557.7 | 0.44 |
| S1.15 | 555.6 | 1.62 | | |
| S2.15 | 555.6 | 1.62 | | |
| P1.25 | 602.4 | 1.76 | 602.4 | 0.41 |
| P3.25 | 602.4 | 1.76 | | |
| S2.25 | - | - | | |
| P3.35 | 649.4 | 1.89 | 649.4 | 0.38 |

6.2.3 Midpoint displacements data

Figures 6.10(a) to 6.11(b) presents the experimentally obtained midpoint displacements. Due to air passing through the perforations/slits and into the dump tank, oscillations occur in the plexiglass in front of the high-speed cameras. This effect makes the pictures blurry and they cannot be used in the DIC-analysis. As a result, the DIC-analysis fails early for some of the experiments and leave little usable displacement data. The point where data is no longer usable is indicated with a black x in the figures. Experiments that led to failure of the plate is not included. As stated in Section 6.2.2, the displacement data is synchronized to have its time axis equal to zero as the incoming pressure wave passes the sensor in front of the plate.

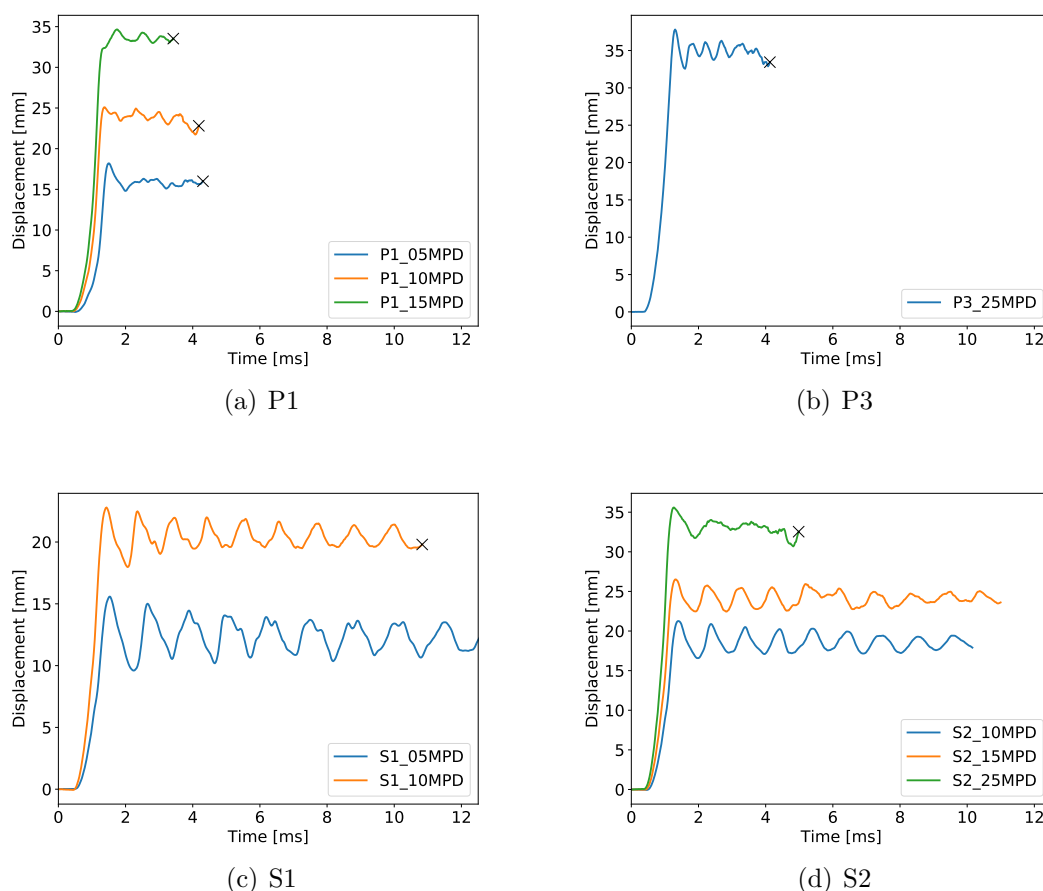


Figure 6.10: Midpoint displacements vs. time measured with 3D-DIC.

As seen in Figure 6.11(a) and 6.11(b), the initial response in midpoint displacement is very similar between configurations when grouped after nominal firing pressure. When grouped by configuration, the deviations are larger. A small fraction of this deviation can be explained by the fact that higher firing pressure results in increased wave speeds [3]. In Table 6.4, the estimates for how long it takes the shock front to travel from the closest sensor to the plate is given. The maximum time consume is

0.53 ms and the lowest is 0.38 ms, and the maximum time deviation due to this effect is therefor 0.15 ms. Between 10 and 15 bar, the deviation is only 0.04 ms.

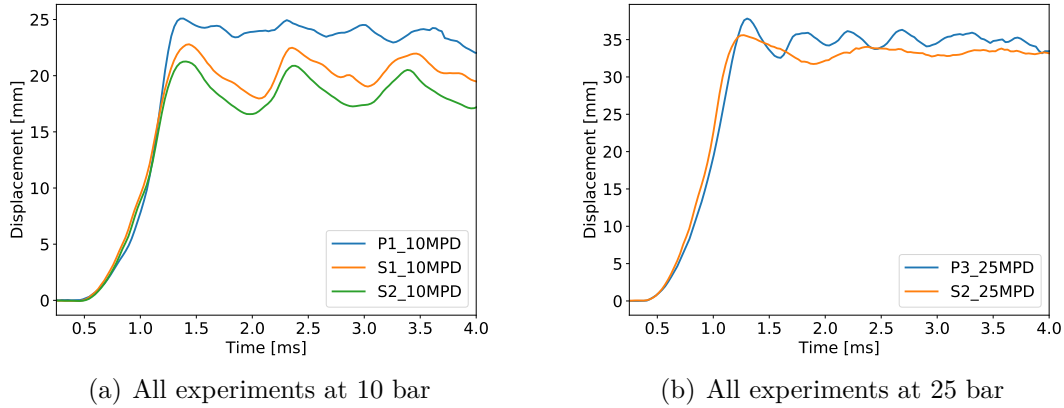


Figure 6.11: Midpoint displacements vs. time measured with 3D-DIC.

Qualitatively, all experiments respond in the same manner. First, a rapid increase of displacements, followed by a phase of oscillations. However, some tests stand out. When comparing the behavior of S2_25 with P3_25 in Figure 6.11(b), the S2 configuration experience noticeably slower oscillations with a lower amplitude. This is probably due to large plastic strains combined with cracking, as the plate was close to collapse in this test. Another result that stands out is the P1_15 which is the slowest test to reach its maximum displacement. When comparing all the P1 tests, seen in Figure 6.12, it is evident that the P1_15 initially deforms with the highest rate. However, the P1_15 only reach a local maximum at 1.35 ms. From this point, it slowly accumulates deformations until it reaches its maximum point at 1.74 ms. When looking at the synchronized images from the high-speed camera, it is observed that the cracks at the four corners of the perforation are growing considerably between 1.35 ms and 1.74 ms.

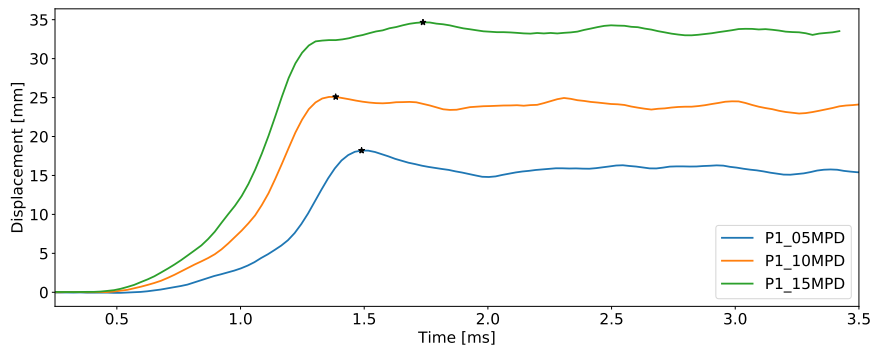


Figure 6.12: Midpoint displacement vs. time plotted until 3.5 ms for all P1 configurations tests

6.2.4 Deformation profiles

The deformation profiles corresponding to the maximum displacement, 80% of max, 60% of max, and 40% of max are presented in Figures 6.14(a) to 6.15(c). The experiments that resulted in total failure of the plates are excluded. It should be noted that extracting the displacement data for the profiles is associated with some uncertainty. This is done manually in eCorr by defining a vector that is suppose to be the center line, illustrated in Figure 6.13 for the P1 and the P3 configuration. To define the vector, it is drawn between what is suppose to be the centered nodes at each side of the plate. The point used to sample the midpoint displacements, plotted in Section 6.2.3, is always included. Because the mesh is fitted to the picture of the undeformed plate using only visual inspection, this represent the greatest uncertainty. Displacement data within the elements are extracted using interpolation of the kinematic fields.

Some of the DIC-analysis required a coarser mesh than others and the result is that the obtained profiles becomes less smooth. A course mesh is needed if the plate experience cracking or if the applied speckle pattern is too uniform.

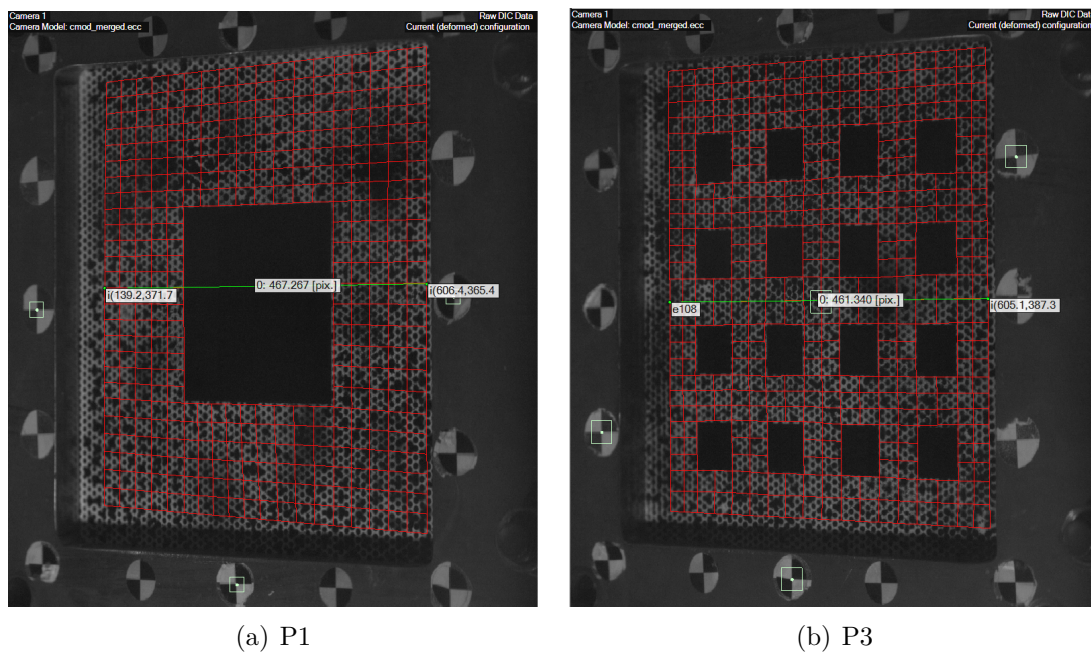


Figure 6.13: The images show the defined vectors used to sample the deformation profiles in the 3D-DIC analyses. (a) show how the center line and the DIC mesh is defined for the P1 configuration and (b) show how the center line and the DIC mesh is defined for the P3 configuration.

6.2. Experimental results

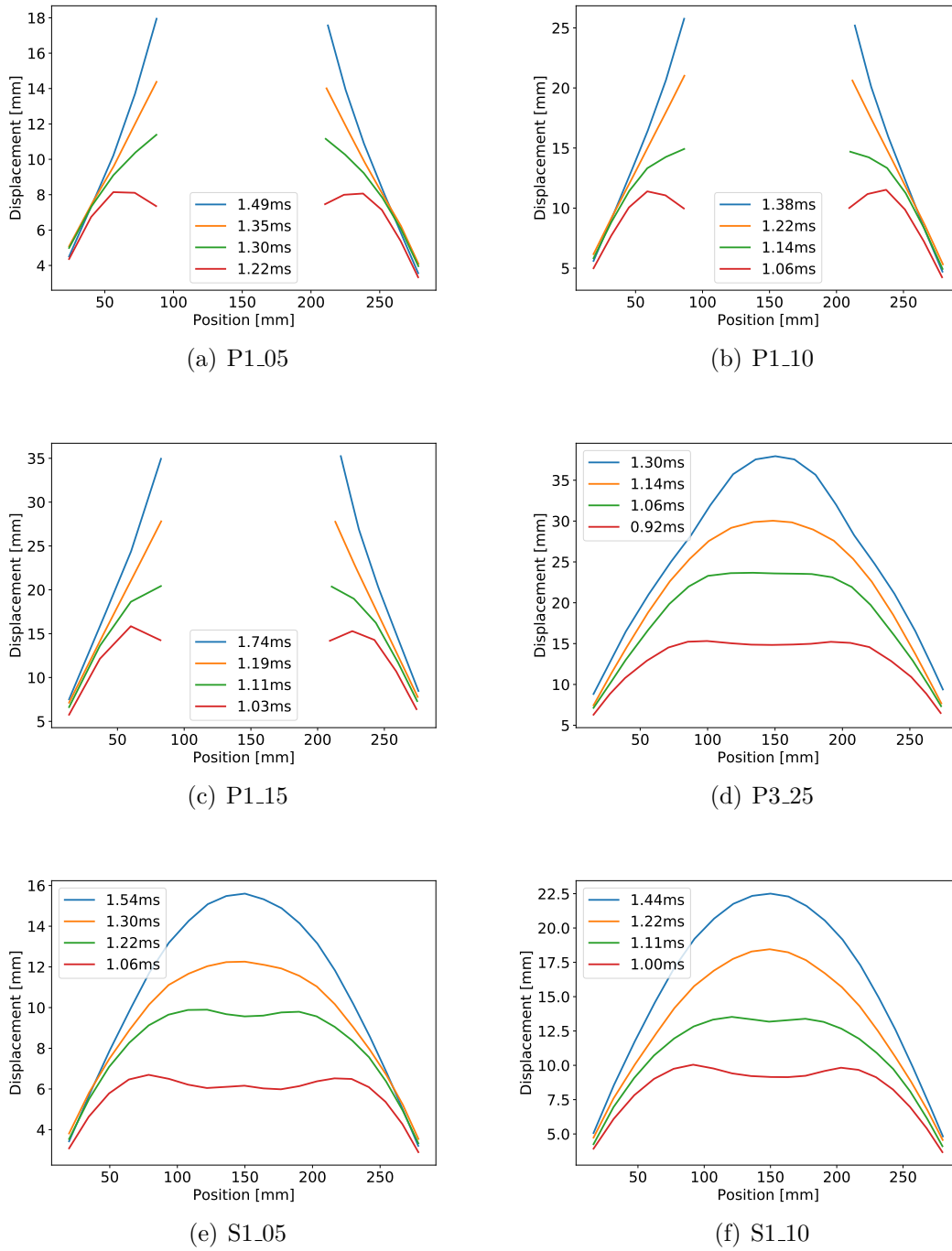


Figure 6.14: Deformation profiles obtained using 3D-DIC.

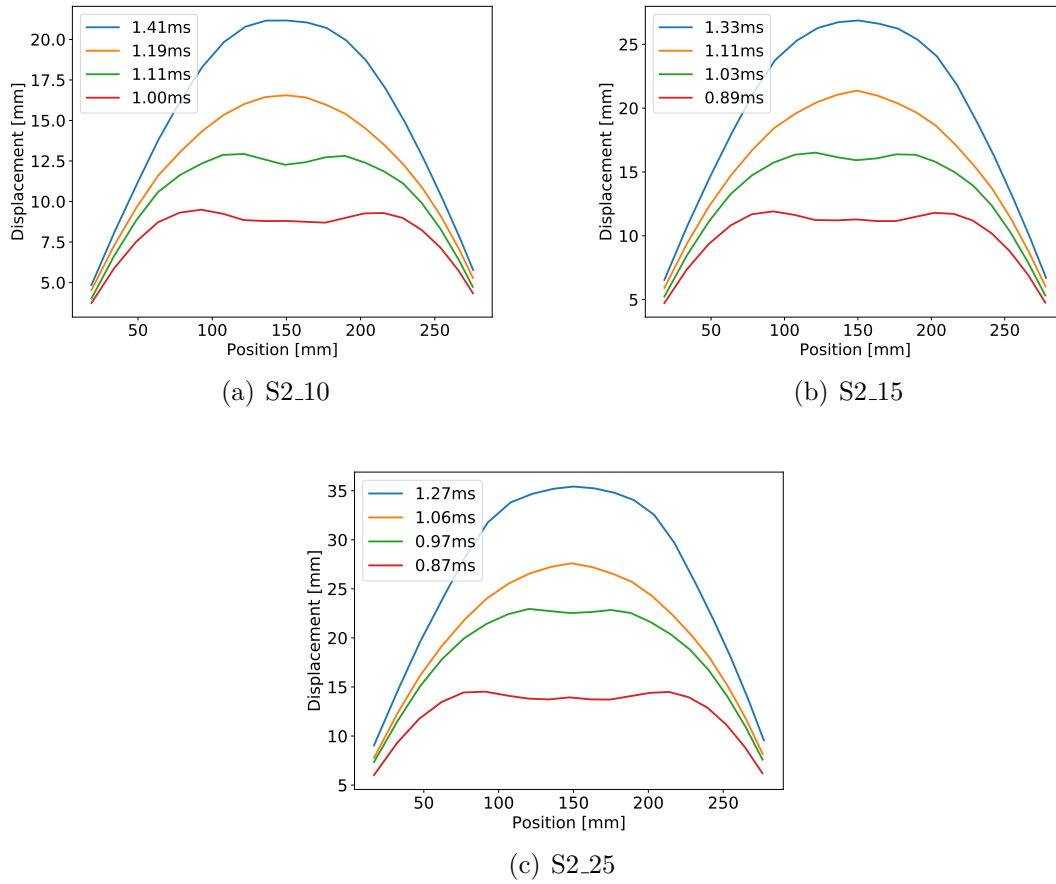


Figure 6.15: Deformation profiles obtained using 3D-DIC.

It is seen in Figures 6.14(a) to 6.15(c), that within each configuration group, the shape of the deformation profile have similar features for all firing pressures. The P3 configuration deviates from the two slitted configurations and although similar, the S1 and the S2 deformation profiles show distinguishable features.

6.2.5 Laser scanning and final deformation profiles

From the measurements using the laser scanning technique, the displacement profiles measured across both the horizontal and vertical center line is presented. All tests experiencing complete failure are excluded. The DIC-profiles are measured along the same axis as what is referred to as "...Lazer_X", and are included for comparison between the two methods. In addition to the comparative profile plots, the full 3D plots of the deformed are presented. These plots are the graphical representation of the obtained point clouds measured with the laser arm and post-processed with MATLAB. The profile and point cloud plots are given for the P1 and P3 configuration in Figures 6.16(a) to 6.19, and for the S1 and S2 configuration in Figures 6.20(a) to 6.22(f).

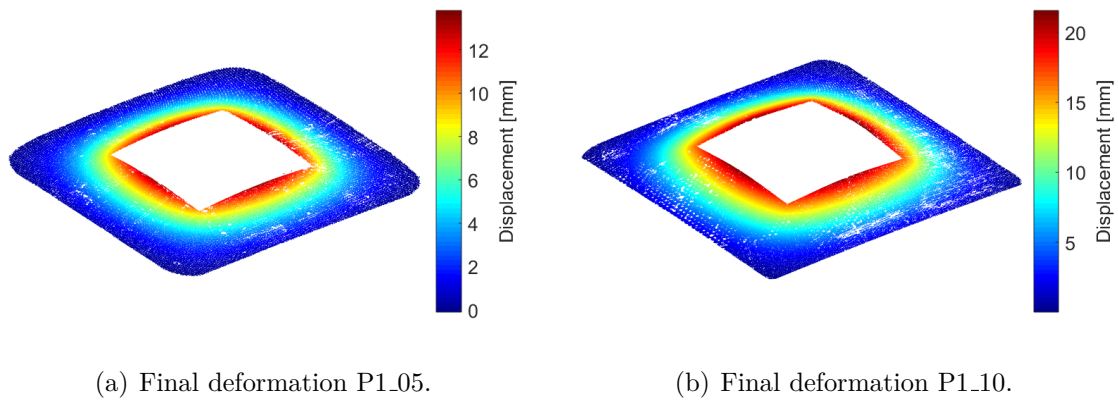


Figure 6.16: The point cloud representation of the final deformations obtained from the laser measurements.

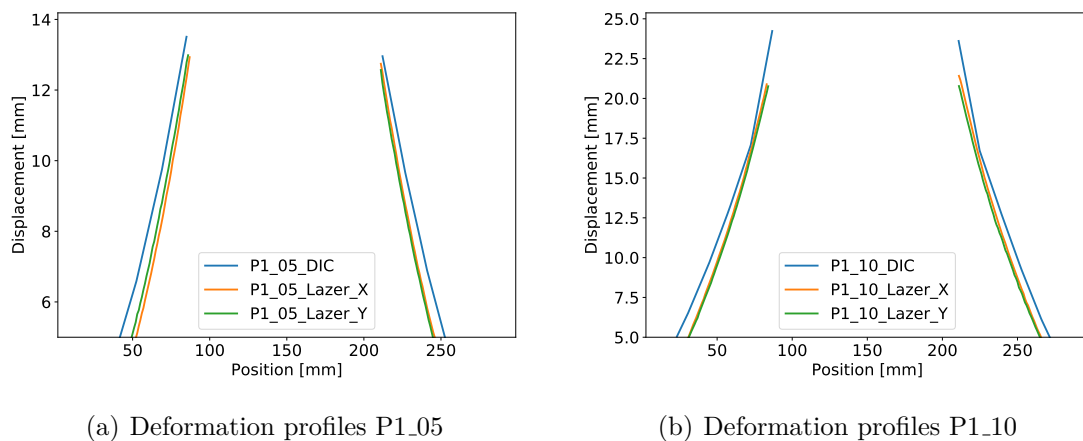


Figure 6.17: Deformation profiles obtained using the laser arm compared to using 3D-DIC.

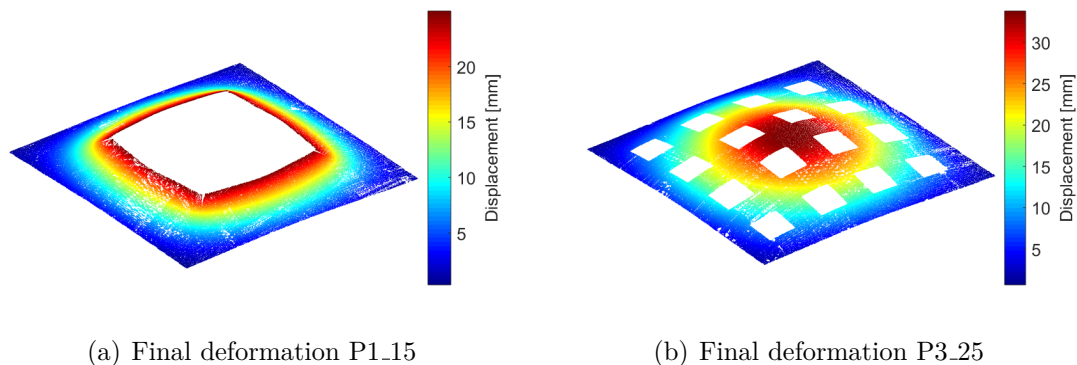


Figure 6.18: The point cloud representation of the final deformations obtained from the laser measurements.

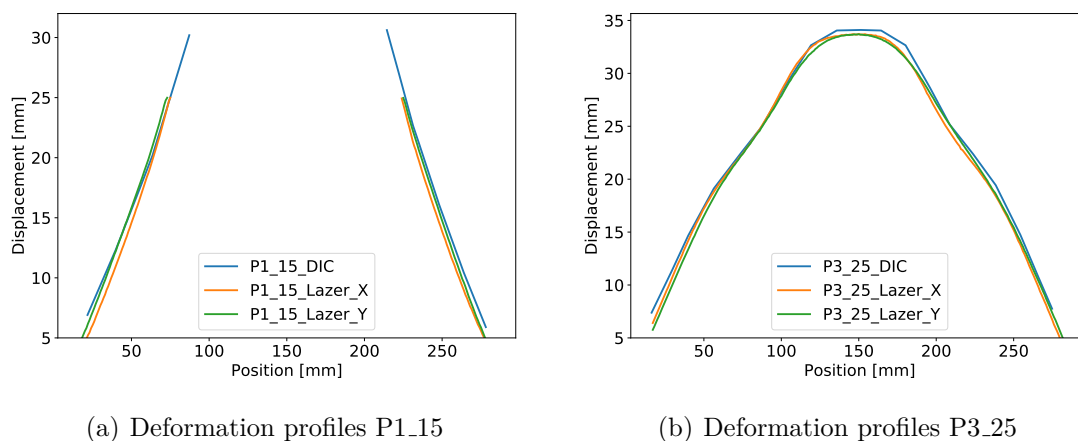


Figure 6.19: Deformation profiles obtained using the laser arm compared to using 3D-DIC.

The maximum deviation between the measurements from DIC and the laser arm is for the P1.10 and P1.15 configuration. For these two experiments, the difference is 2.7 mm and 4.6 mm respectively. To find the permanent displacements using DIC, a post picture is taken approximately a minute after the blast event is over. The picture is taken after the oscillations have stilled, and the deformation has reached its permanent state. Due to oscillations in the plexiglass, as mentioned in Section 6.2.3, the DIC analysis struggle. When the DIC-analysis is run, the post picture is added after the last valid image in the image series. This results in a quite large change in displacements between the two last images in the series, and the mesh separate along the boundary of the perforation. This is probably what causes the deviation between the two measuring techniques. With the exception of the experiments on P1.10 and P1.15, the two measuring techniques are in acceptable compliance.

The green circle Figure 6.20(a) - 6.20(b) indicates the area where the mesh has separated from the plates. Although this could be part of a possible explanation for the deviation measured between the laser and DIC, no separation was found for the P1_15 test. In this test, the deviation is even larger than for the P1_10.

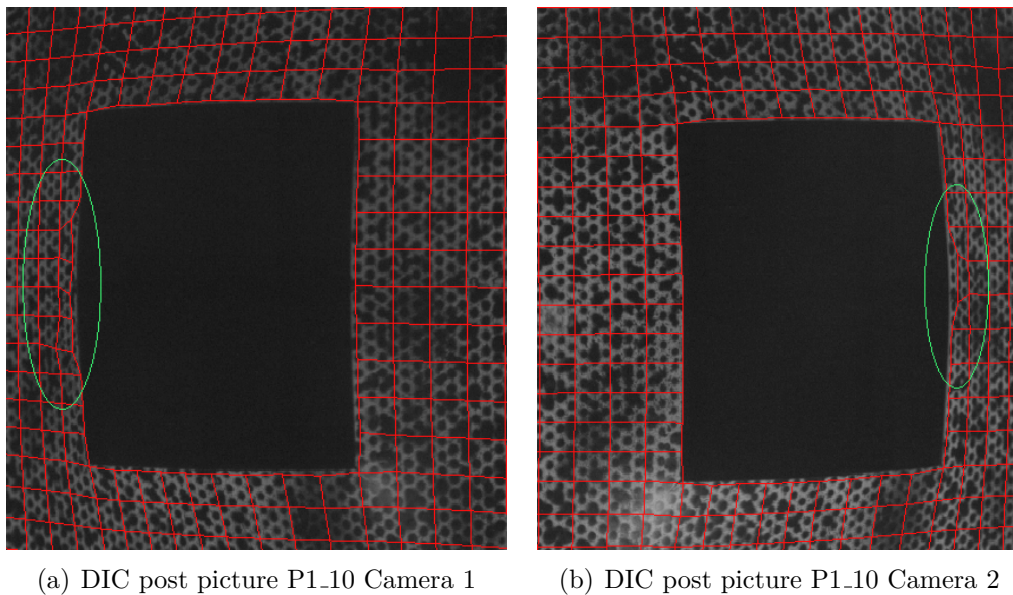


Figure 6.20: Indicating the 3D-DIC analysis where the mesh separated from the plate along the boundary of the perforation for the P1 plate tested at a nominal firing pressure of 10 bar

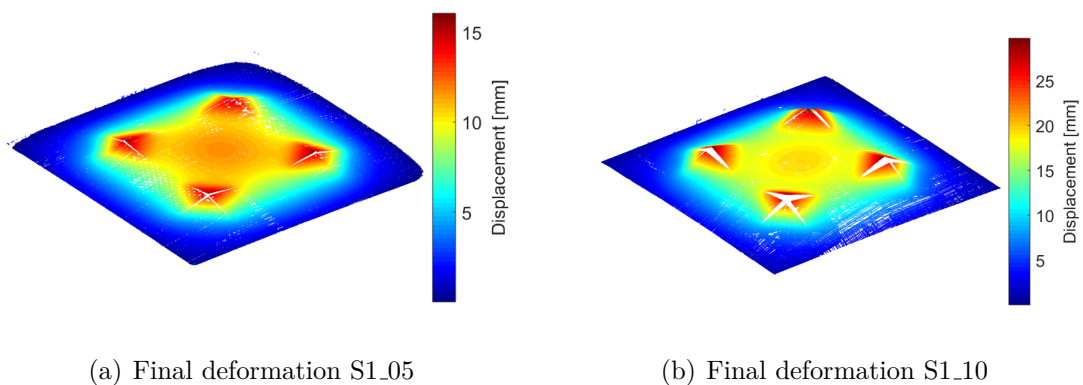
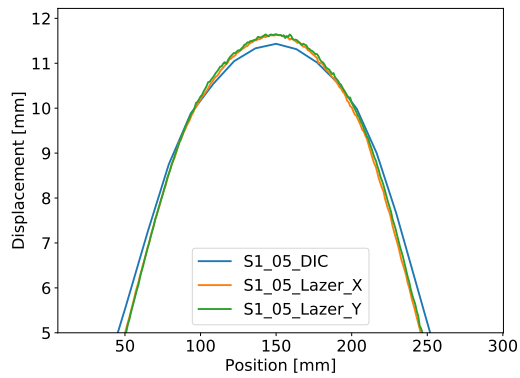
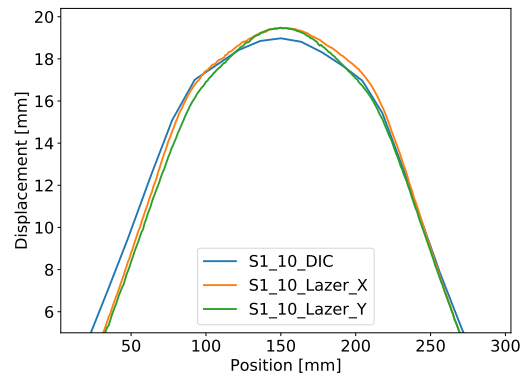


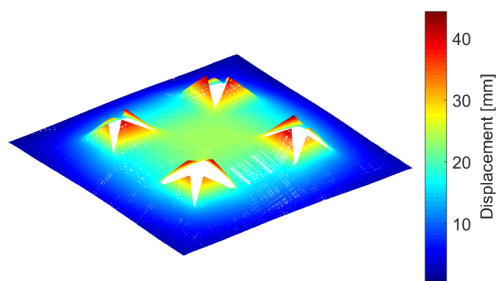
Figure 6.21: The point cloud representation of the final deformations obtained from the laser measurements.



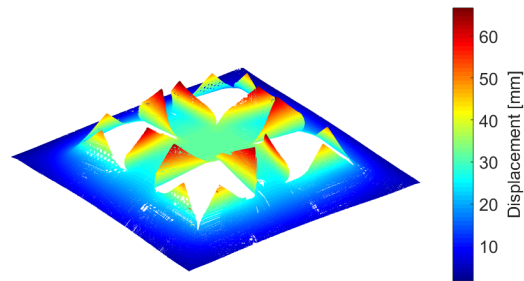
(a) Deformation profile S1.05



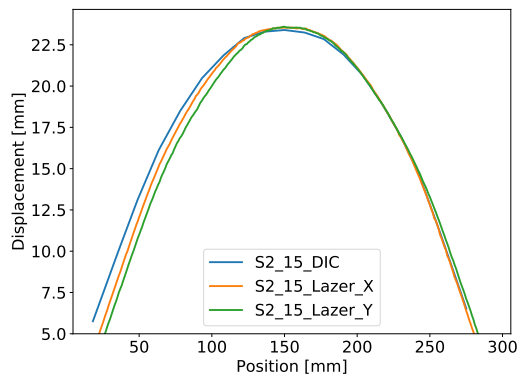
(b) Deformation profile S1.10



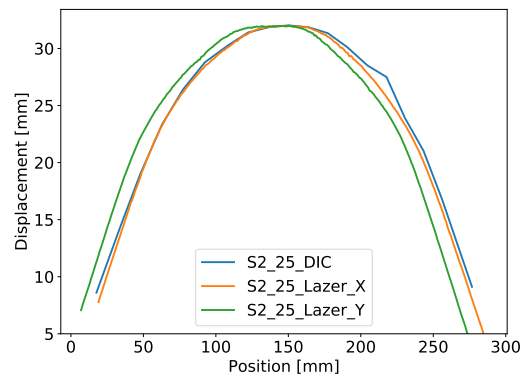
(c) Final deformation S1.15



(d) Final deformation S2.25



(e) Deformation profiles S2.15



(f) Deformation profiles S2.25

Figure 6.22: Deformation profiles obtained using the laser arm compared to using 3D-DIC, and the point cloud representation of the final deformations obtained from the laser measurements.

The deformation profile obtained from the DIC analysis for the S2.25 experiment, seen in Figure 6.22(f), is experiencing an unrealistic peak in displacement. This is seen when evaluating the displacement in the position range 200 mm to 250 mm. At this location, the slits are opening up completely and it creates a shaded area above the speckle pattern in the post image. This confuses the DIC-analysis, due to a rapid

change in grey-scale values.

The green circles in Figure 6.23(a) and 6.23(b) indicate the areas where the speckle pattern is disturbed by both a shadow and pieces of the plate itself. When looking at the horizontal center line, it is clear that the nodes/elements within the shaded region are without visual speckles. This makes it impossible for the displacements to be calculated. However, most parts of the displacement profile are in good agreement with the laser measurements in the X-direction, labeled S2_25_Lazer_X.

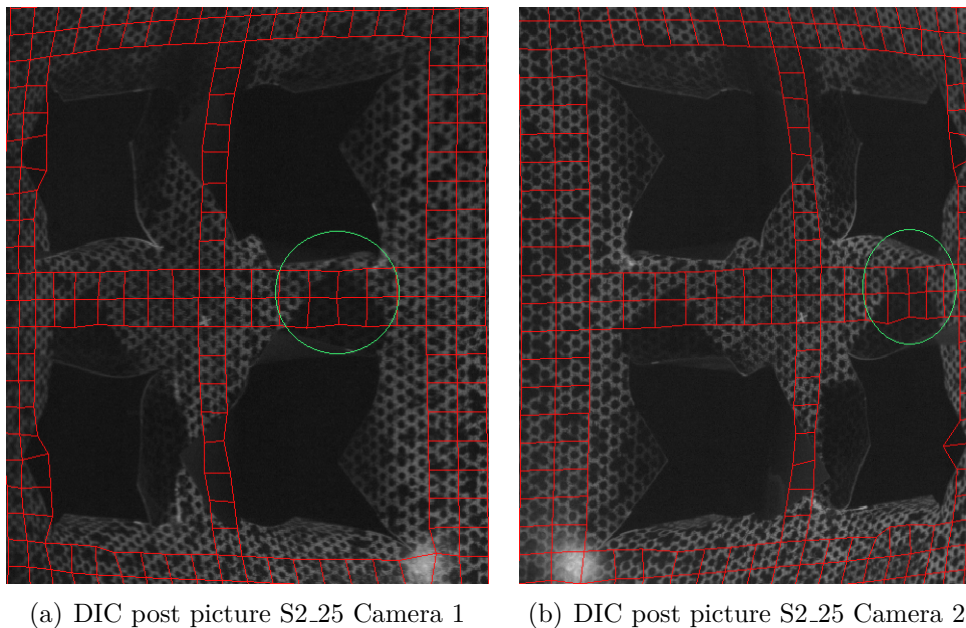


Figure 6.23: Showing the area of the S2 plates exposed to a firing pressure of 25 bar where the opening of the slits covered up the speckle patten along the center line of the plate, and disturbed the 3D-DIC analysis.

6.2.6 Observed failure modes

For the experiments that led to failure, a selection of the high-speed camera images are included to document the crack propagation. The S2 configuration tested at 25 bar is an exception as this experiment did not experience complete failure, but the crack propagation was considered large enough to be included in this section. In Figure 6.24 and 6.25, the failure modes observed for the P1 and the P3 configurations are presented.

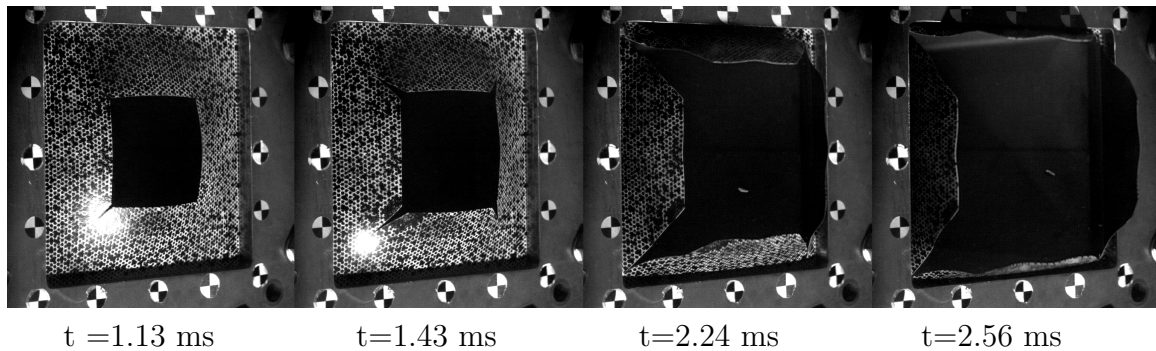


Figure 6.24: Showing the symmetric failure mode for the P1_25 test.

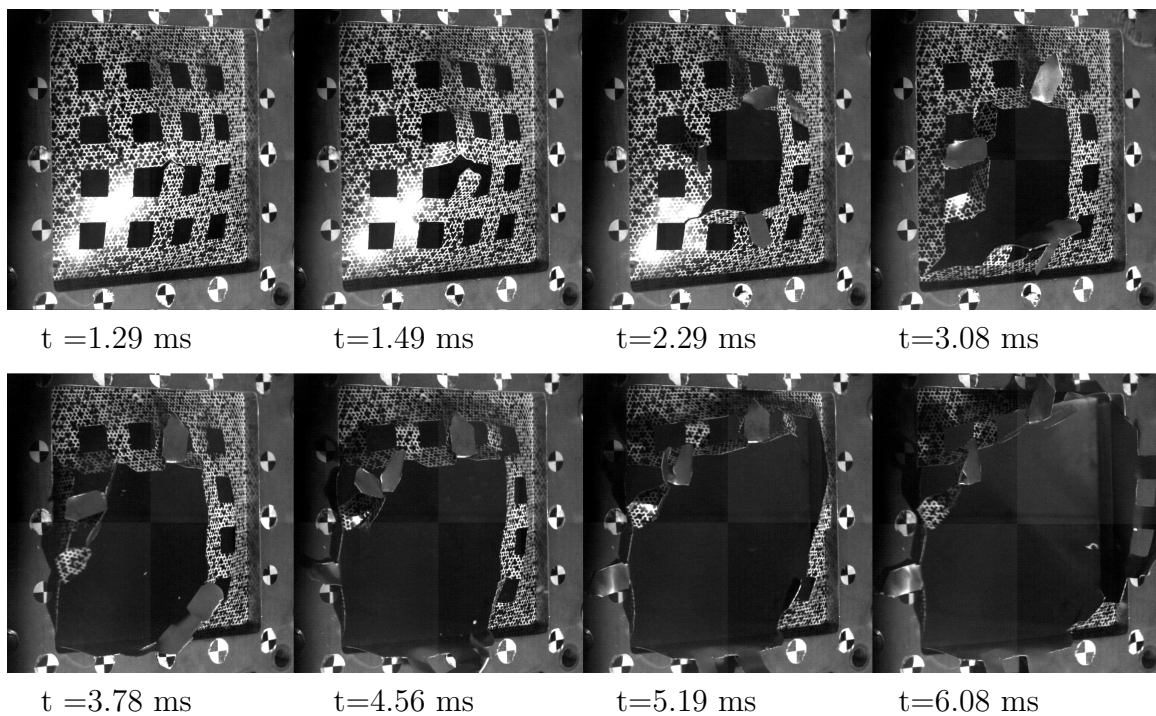


Figure 6.25: A selection of high-speed images showing the obtained failure mode for the P3.35 test. It is tried to capture the non-symmetric initiation of the failure at the center of the plate, and the propagation all the way to complete failure.

For the P1 configuration, failure happens as the cracks initiated in the perforation corners propagate diagonally all the way to the boundary of the blast-exposed area. The loose flaps, seen in the last image in Figure 6.24, ends up being wrapped around the edges of the clamping frame. This is seen in the section containing post test images. For the P3 configuration, the failure mechanism is more complicated, and it is harder to describe. As seen in Figure 6.26, the failure initiates at the center of the plate, where cracks are formed in each corner of the perforation closest to the midpoint of the plate. It becomes unsymmetrical as one crack propagate faster than

the others, and this initiates a complete tearing down towards the lower left corner of the clamping frame. This failure mode is the one deviating most from what was found in the numerical simulations done in Chapter 4.

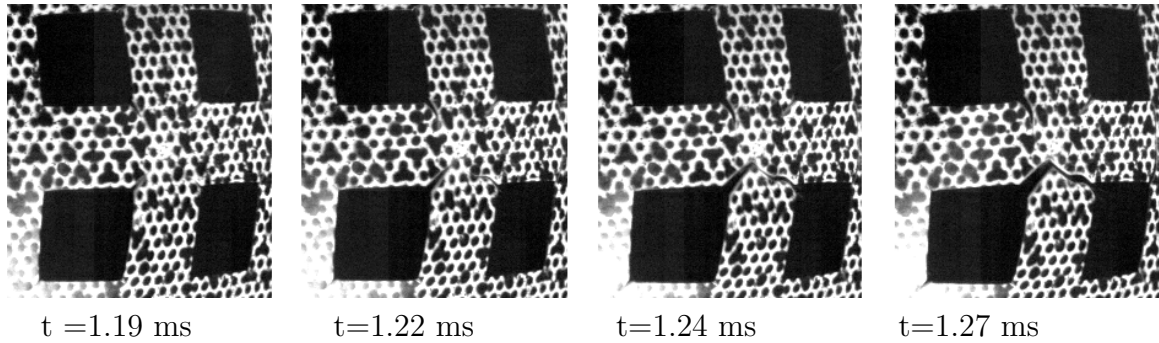


Figure 6.26: Showing the failure mode for the P3.35 test. The images are zoomed in at the center of the plate to capture the non-symmetrical initiation of the crack propagation.

For the S1 configuration, the cracking initiates symmetrical, but one horizontal crack propagating faster than the others. This is seen in Figure 6.27. The result is that a flange still connected to the plate is cut out. Regarding the S2 configuration, complete failure was never reached. As can be seen in Figure 6.28, the plate still have some rest capacity but is highly deformed.

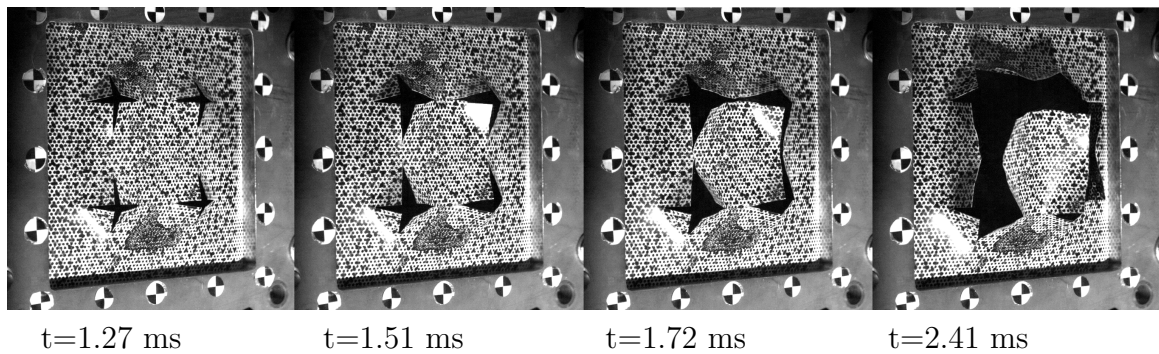


Figure 6.27: Showing high-speed images of the failure mode for S1.15 at a selection of times.

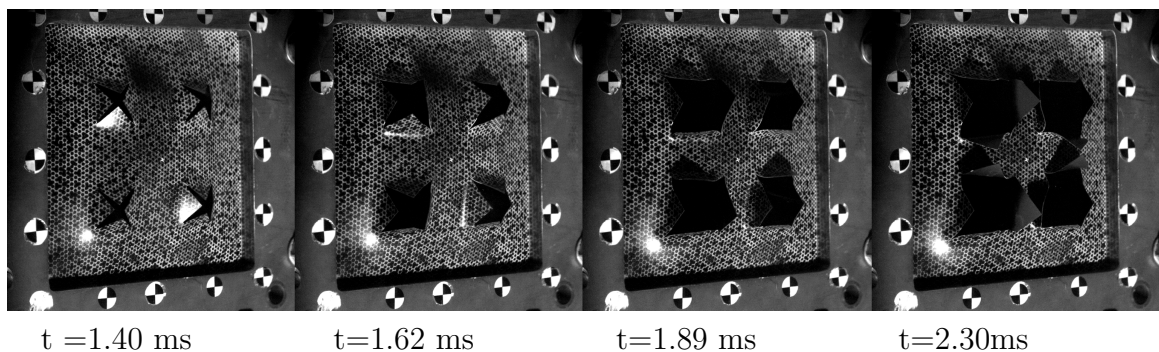


Figure 6.28: Showing high-speed images of the failure mode for S2.25 at a selection of times.

6.2.7 Measured crack lengths

In Chapter 4, crack lengths was one of the important parameters to evaluate when constructing the test matrix. For validation of new numerical models, the crack lengths are documented through this section. The measurements are given i Table 6.5, and relates to the illustrations in Figure 6.29.

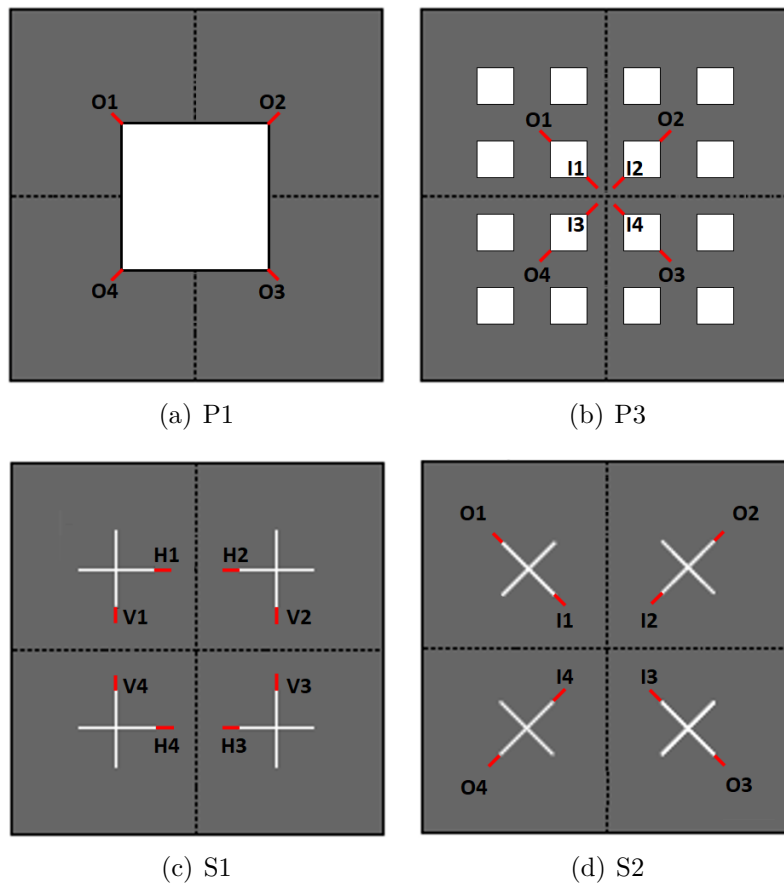


Figure 6.29: Orientations of measured cracks.

When measuring the cracks, it was found that some of the configurations did not crack, but only necked in the highly stressed areas. This was at least the finding with only a visual inspection. If applying more advanced inspection methods, small or internal cracks can possibly be found. For the plates with large visible cracks, the necking is also present at the crack-tip. To distinguish between cracks and necking may be hard, and this made the measuring process challenging. Both phenomena are illustrated in Figure 6.30. The method of measurement was rather crude, as a digital caliper was the only tool available. Based on doing repeated measurements of the same crack by two persons, the uncertainty in the measurements is given as a rough estimate. For the long and short cracks, the uncertainty is estimated to be ± 1 mm and ± 0.5 mm. In the Table 6.5, N indicates a pure necking and a number indicates an actual crack length.

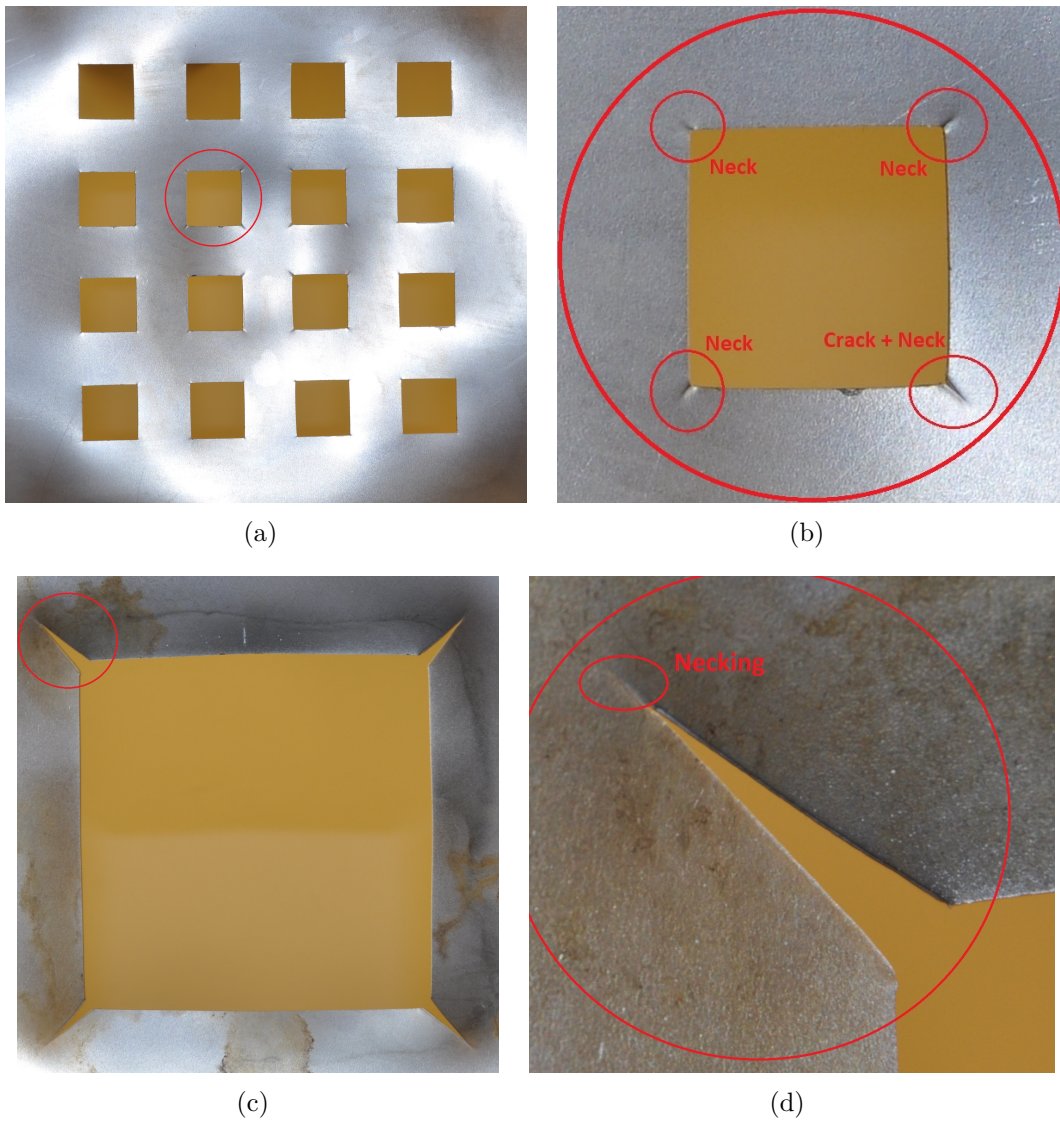


Figure 6.30: Images identifying cracks and necking for P3.25 and P1.15. (a) P3.25 showing both cracks and necking, (b) Zoomed image of cracks and necking for P3.25, (c) P1.15 showing cracks with necking at the tip, (d) Zoomed image of the combination of a crack and necking for P1.15.

All four images in Figure 6.30 are taken from the backside of the plates. The clean steel surface without the speckle pattern makes it easier to see the necking, and also to distinguish between a crack and a necking. The P3.25 test shows both pure necking and the mix of cracks and necking, while P1.15 shows more distinct cracks with a neck at the crack tip.

Table 6.5: Crack data for all tests that did not experience complete failure. Measurements are made with reference to the crack name convention introduced in Figure 6.29. Where only necking was observed, an N is given. For the S2_25 experiment cracks was too large to be practically measured, this is indicated with X.

| Test | O1 | O2 | O3 | O4 | I1 | I2 | I3 | I4 |
|-------|------|------|------|------|------|------|------|------|
| S2_10 | N | N | N | N | 4.4 | 4.7 | 4.3 | 4.2 |
| S2_15 | 5.1 | 4.4 | 4.7 | 4.8 | 11.4 | 10.8 | 10.9 | 10.3 |
| S2_25 | 22.8 | 22.2 | 21.2 | 22.5 | X | X | X | X |
| | H1 | H2 | H3 | H4 | V1 | V2 | V3 | V4 |
| S1_05 | N | N | N | N | N | N | N | N |
| S1_10 | 5.1 | 5.4 | 6.2 | 5.8 | 7.2 | 7.9 | 7.5 | 7.4 |
| | O1 | O2 | O3 | O4 | I1 | I2 | I3 | I4 |
| P3_25 | N | N | N | N | 2.0 | 2.4 | 1.6 | 2.2 |
| | O1 | O2 | O3 | O4 | | | | |
| P1_05 | N | N | N | N | | | | |
| P1_10 | 6.1 | 6.2 | 6.4 | 6.1 | | | | |
| P1_15 | 25.0 | 26.0 | 22.7 | 22.3 | | | | |

Flipping of cracks

Some of the measured cracks experienced the crack-flipping phenomenon. This is characterized by the crack changing its direction through the plate thickness with a $\pm 45^\circ$ with respect to the axis going straight through the thickness. The S2_25 is the test where this phenomenon is most evident, but it is also observed in some of the other configurations. The flipping phenomena were also reported in [29].

Figure 6.31 shows the orientation of the yield line through the thickness of the plates. The orientation has two equivalent solutions, being $\theta = \pm 45^\circ$. This is based on Hills analysis and can be found in [8]. In the experiments, it seems like the crack is changing in-between the two directions along the length axis of the crack. Figure 6.32 shows the flipping phenomenon for the S2 configuration at 25 bar.

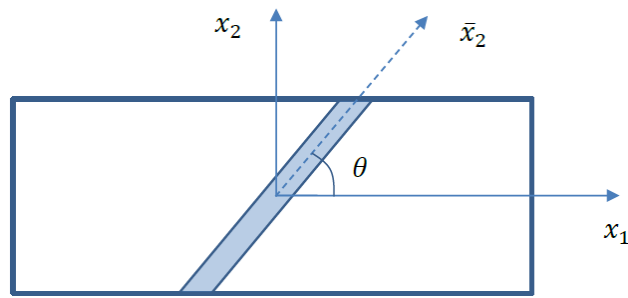


Figure 6.31: Through thickness yield line for the plates. The image is taken from [8].

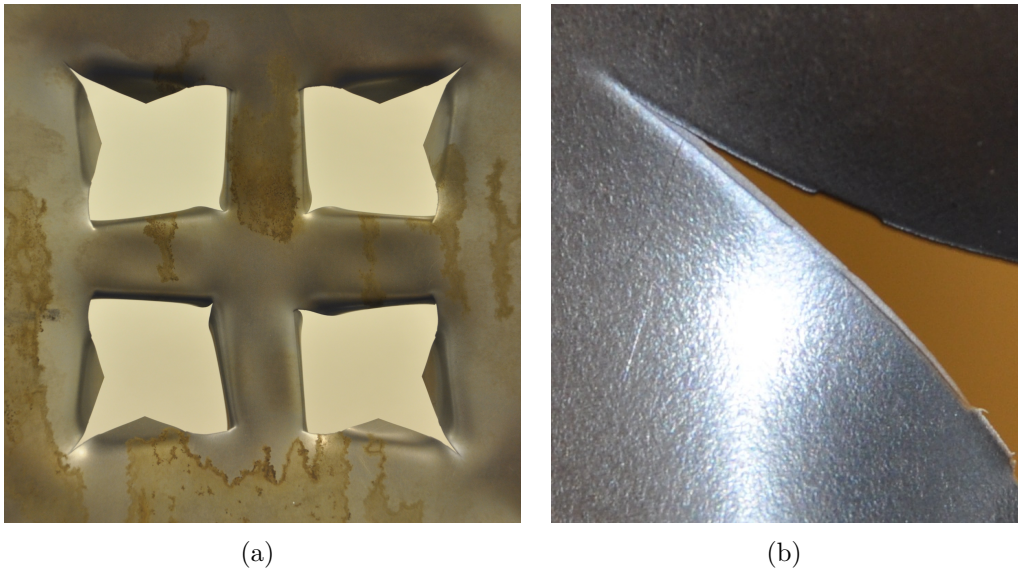


Figure 6.32: Images of the S2_25 test experiencing flipping at some of the cracks. (a) S2_25 at its final deformation, (b) Zoomed image of a crack exhibiting flipping.

6.2.8 Concluding remarks

The test matrix obtained in the preliminary study was generally in good agreement with the experimental results. Both the P3 and S1 configurations exhibited the numerically predicted behavior for all three firing pressures. The exceptions are the S2 and the P1 configurations. At 10 and 15 bar, the S2 configuration responded as predicted, while the 25 bar test did not experience complete failure as predicted numerically. For P1, the test matrix had to be expanded to a firing pressure of 25 bar to obtain complete failure, and hence, the numerically predicted capacity of the plate was under-predicted.

For the pressure-time data, the observed trend is that perforated plates produce lower reflected pressures than slitted plates. When comparing the perforated plates, some

alternation between the configurations is seen. The decrease in the reflected pressure is thought to have two main contributions, the deformation of the plate itself and the leakage of air flowing into the dump tank. Obviously, perforated plates allow for more leakage than full and slit plates. This being said, is hard to determine to what degree it is the leakage effect or the reduced stiffness that reduces the pressure build-up. Within the different perforated configurations, the experiments suggest that the P3 configuration gives the overall lowest reflected pressure. However, the lack of test data for the firing pressure of 15 bar makes it hard to conclude on this matter.

When comparing the crack propagation in the S1 and S2 configurations to the geometrically similar aluminum plates tested by Stensjøen and Thorgeirsson [30], the results are almost identical. For the S1 configuration, the failure mode found in aluminum and steel shows a similar pattern. Although complete failure did not occur for the S2 configuration, the failure mode seems to initiate in the same way as in the aluminum plates. In the appendix, some images illustrating the failure modes found in their master is included for comparison.

The observed failure modes in the plates seem to become more unsymmetrical as the geometrical complexity increase. Unfortunately, no repeated test was conducted in this study. Due to the complex geometry for the P3 configuration, it could be interesting to perform repeated tests at its failure pressure, to investigate the potential variation in failure modes.

For the most part, the results obtained from the laser measurements and DIC were in good agreement. The exceptions were the tests regarding the P1 configuration and the S2_25 test. For the P1-tests, most of the problems regarding the DIC-analysis is probably due to oscillations in the plexiglass in front of the cameras. For the S2_25 test, the complete opening of the slits gave shadows covering parts of the speckle pattern, and this caused trouble for the DIC-analysis. The results from the laser arm were considered the most trustworthy, and they also serve as a great tool to inspect details in the deformed geometry.

Chapter 7

Numerical work

This chapter will serve as a final numerical study where simulations in both Abaqus and Europlexus will be evaluated. The chapter consists of three main parts. First, the most geometrically complex Lagrangian models developed in Abaqus will be validated through a comparison with the experimental results. Here, the midpoint displacements, failure modes, and deformation profiles will be considered. The second part will compare Lagrangian models in both Abaqus and Europlexus. To identify the deviations purely related to the change of solvers, identical loading histories and material parameters will be applied to all models. The last part will evaluate the effect of including fluid-structure interaction through running coupled Eulerian-Lagrangian analyses in Europlexus.

7.1 Description

Based on the parametric study in Chapter 5, the parameters for the final Lagrangian models in Abaqus was determined and will be applied in this chapter. The fully coupled simulations are run in Europlexus, which is a software for simulations of fast transient fluid-structure interaction problems. It is developed jointly by several co-owners plus the members of a consortium, and a number of Universities. The simulations run in this code are included to investigate the effects of FSI, and to compare the pure Lagrangian approach to the fully coupled Eulerian-Lagrangian method. The use of Europlexus was only possible due to guidance from our supervisor V. Aune, and the models applied in this chapter were developed in conjunction with his PhD thesis [3] and through the work, he does as an associate professor at NTNU.

In Europlexus, both fully coupled and pure Lagrangian simulations are included. The clamping frame and bolts are modeled slightly different for the models in Europlexus and Abaqus. Therefore, it was considered important to compare results between the two solvers for similar loading histories in the Lagrangian models before evaluating the FSI effects.

It should be noted that some trouble was encountered when running simulations

in Europlexus due to a bug in the solver. This was related to the combination of adaptive meshing and the description of contact between the testing plates and the clamping frames. Europlexus has a narrow and very specialized market segment and is a cutting-edge software. Due to this, the code is not as robust as the more established solvers such as Abaqus and LS DYNA.

Initially, the goal of this chapter was to run the most complex FSI models developed by Aune and to compare the results with the experimental work. However, due to the bug in the solver, all simulations was delayed and it was decided to only evaluate the geometrically simple models when including FSI. This choice limited the focus in Section 7.5 to only evaluate the effect of including FSI in the simulations, rather than to investigate whether the coupled Eulerian-Lagrangian approach gives better results than the pure Lagrangian simulations.

7.2 Numerical models

This chapter contains numerical models in two different solvers, and the models in each solver will be presented separately. As stated, the parameters for the models in this chapter are based on the findings from part two of the preliminary study, described in Chapter 5. Table 7.1 gives the applied material parameters and friction coefficient used for both solvers. Note that μ is applied as both the static and the dynamic friction coefficient. The strain rate sensitivity parameter has also been changed from $c=0.01$ to $c=0.005$ due to findings in Chapter 4.

Table 7.1: The material parameters for the Docol 600DL steel, and the frictional coefficient applied in the numerical models. The coefficient μ is applied as both the static and dynamic friction coefficient.

| A | Q_1 | C_1 | Q_2 | C_2 | c | m | \dot{p}_0 | W_c | μ |
|-------|-------|-------|-------|-------|-------|-----|--------------------|-------|-------|
| [MPa] | [MPa] | [-] | [MPa] | [-] | [-] | [-] | [S^{-1}] | [MPa] | [-] |
| 325.7 | 234.5 | 56.2 | 445.7 | 4.7 | 0.005 | 1.0 | 5×10^{-4} | 555.0 | 0.16 |

7.2.1 Lagrangian models in Abaqus

The Lagrangian models in Abaqus are the geometrically complex models, applying three solid elements across the thickness, described in Chapter 5.

7.2.2 Europlexus

All models run in Europlexus apply the same representation of the blast-exposed plate, and all utilize symmetry about two axes. The Plate is discretized using four-noded, fully integrated shell elements, and the adaptive mesh refinement technique,

outlined in Chapter 2 is applied. The initial element size is 6mm and is refined down to the minimum size of 0.75mm as the Cockcroft-Latham damage parameter in the most affected integration point is on the interval ($0.01 \leq D \leq 0.02$).

The difference between the Europlexus models is the implementation of loading and boundary conditions. For the geometrically simple models, only the blast-exposed area of the plate is included. This is illustrated in Figure 7.1(b) for the P3 configuration. The outer boundaries are fixed and marked with black, which is equivalent to the simple models applied in Chapter [ch:prelimI].

The geometrically complex models include the clamping frame with bolts and apply the pinball contact with a penalty constraint equation. The tangential behavior is governed by the simple Coulomb friction model with an equal static- and dynamic friction coefficient. The surface on the clamping frame facing the incoming shock-wave is fixed in all degrees of freedom, and the bolts are modeled without the bolt heads. The end of the bolts facing the incoming shock wave is merged together with the clamping frame, modeled as one part. To represent the bolt load, a surface traction is applied to the area around the bolt holes on the clamping frame furthest from the incoming shock wave. This area is marked in gray in Figure 7.1(a). The applied traction force is kept constant and corresponds to a bolt force of 46.5 kN, which is equivalent to the model in Chapter 5. It is important to note that this implementation of the bolt load differs from the one presented in Chapter 4.

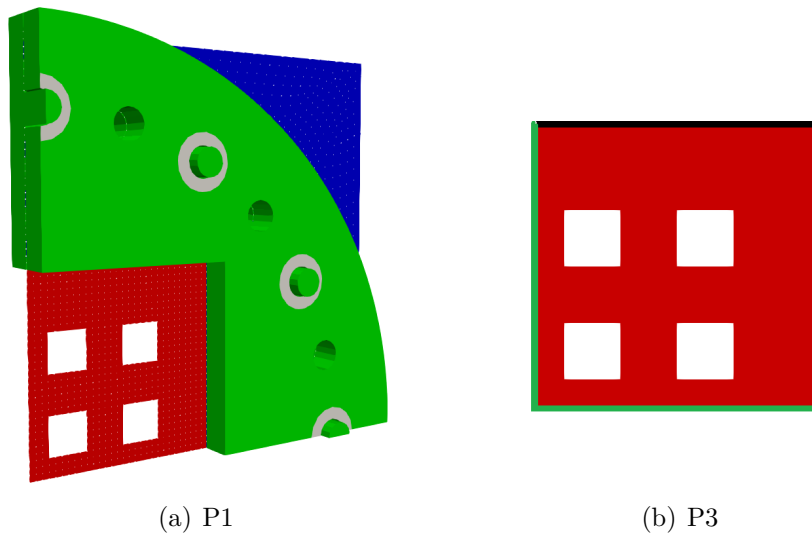


Figure 7.1: Illustration of the numerical models in Europlexus, shown with the P3 configuration as the blast exposed plate. (a) shows the geometrically complex model, including the clamping frame and bolts. (b) shows the geometrically simple model. Only the blast-exposed area is included, and the green lines indicates symmetric boundary conditions and the black lines represents the fixed outer boundary.

Lagrangian models in Europlexus

In the purely Lagrangian models, the same pressure-time curves are used in Europlexus as presented in Chapter 4 for the models in Abaqus. Lagrangian models run with both the simple and the complex boundary implementation will be included.

Fully coupled Eulerian-Lagrangian in Europlexus

The fully coupled simulations apply a finite volume formulation for the discretization of the fluid. To model the interaction between the fluid and the solid, an embedded FSI technique is applied. Both the finite volume and the embedded FSI technique is more thoroughly described in Chapter 2.

The fully coupled models include the entire shock tube, as well as the rupture of the membranes. This level of detailing has been shown by Aune et al. [32] to be necessary to get a realistic representation of the loading on the plates. The rupture process of the membranes introduce disturbances in the initial phase of the wave propagation, and this effects must be included to get good compliance with the experimentally obtained pressure measurements. To save computational time, the fluid domain is only considered as a 3D domain in the proximity of the membranes and the blast-exposed plate. In parts of the shock tube where the flow is mostly uniform, a 1D domain is used [53].

7.2.3 Naming convention

All name labels start with the same two-letter shortening of the geometrical configuration as described in Chapter 4, followed by the nominal firing pressure. The modeling-specific parts of the name labels presented in Table 7.2 states which solver that was used, and further parametric changes from the standard models. Explanations regarding different parametric changes are given in the result section.

Table 7.2: Descriptions of the naming convention used in both plots and tables in this chapter.

| Part of name | Explanation |
|--------------|--|
| _ABQ | Model in Abaqus |
| _Exp | Experimental data |
| _EPX | Model in Europlexus, geometrically complex |
| _Fix.EPX | Model in Europlexus, geometrically simple |
| _L | Purely Lagrangian model |
| _CEL | Coupled Eulerian Lagrangian |

7.3 Validation of Abaqus models

This section serves as a validation of the most realistic Lagrangian models, developed in Abaqus. The numerically obtained results will be compared with the experimental work. Crack propagation, failure modes, and displacements will be evaluated in the same manner as what was done in the preliminary study presented in Chapter 4 and 5.

Chapter 4 aimed to determine the test matrix for the experimental work, Crack arrest and failure modes has been one of the important parameters for benchmarking of the preliminary numerical models. Due to the specific focus in the prediction of the capacity of the plates, and the ability to within a reasonable range determine obtained crack lengths in previous chapters, this will be the first topic for validation of the final models. Further, the midpoint displacement response and deformation profiles will be evaluated.

7.3.1 Evaluation of failure modes and cracking

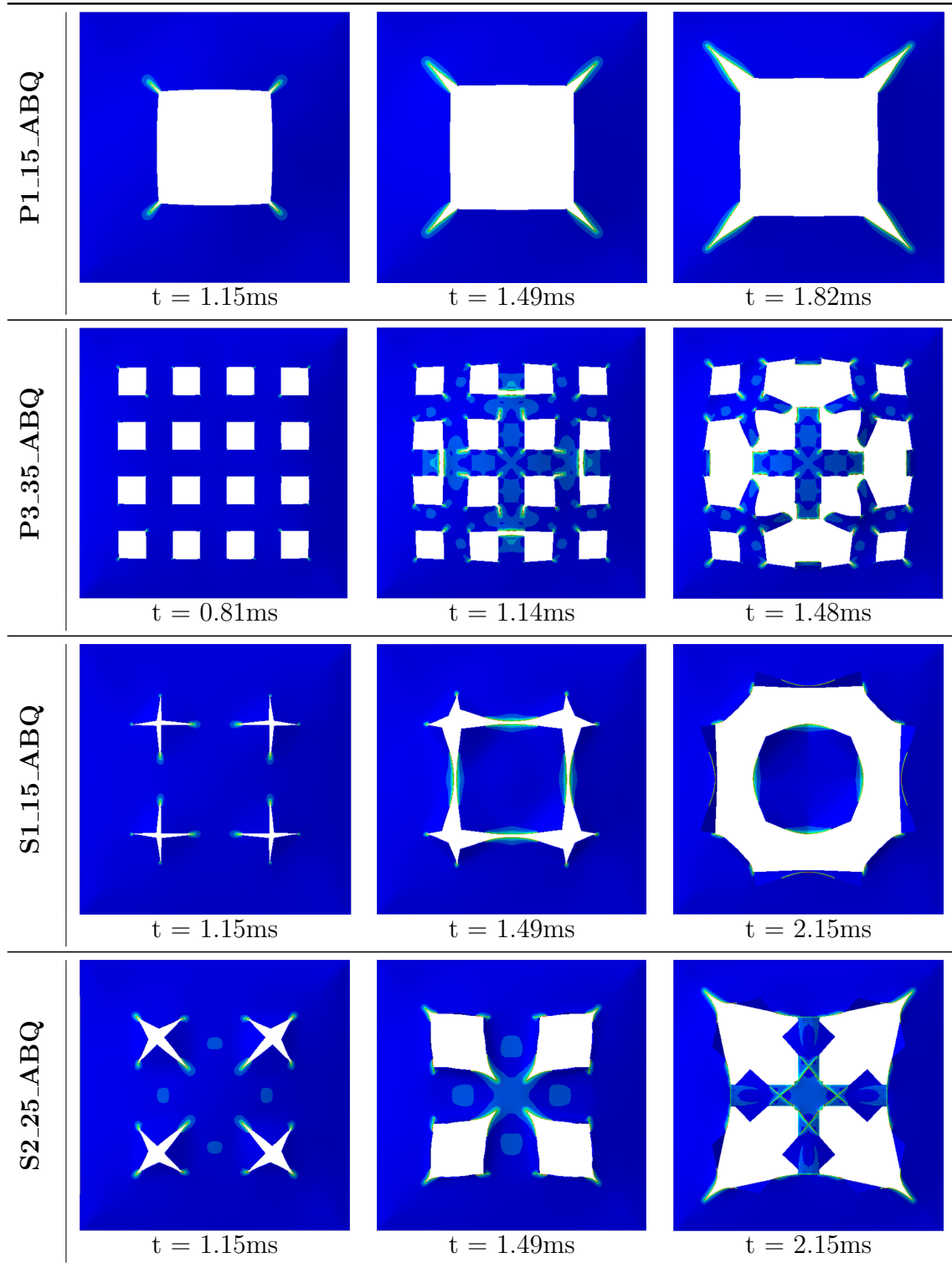
In table 7.3, the numerically predicted failure loads for the different configurations are compared to the experimental results. It is seen that the Lagrangian model in Abaqus is able to accurately predict failure for two out of four configurations. The failure estimate deviates from the experimental results by underestimating the capacities of the plate and is therefore conservative.

In Table B.4 the numerically obtained failure modes for the different configurations are given. It is seen that the simulated result for S1_15 is in good agreement with the experimental results. Both the failure load and mode are correctly predicted. For the P1 configuration, the correct failure mode is predicted, but the capacity is underestimated numerically. As stated in the experimental work, P1_15 does not experience complete failure experimentally, but numerically it does when modeled with both the geometrically complex model and the simple model from Chapter 4. For the P3 configuration, the correct failure load is predicted but the numerical failure mode differs from the experimental result. The failure mode observed for the 35 bar simulation in this section also deviates from what was found in the preliminary study, in Chapter 4. A plausible reason for this may be the change in the strain rate sensitivity. Numerically S2_25 is experiencing a complete failure. Experimentally, this test was observed to be at the very limit, but complete failure was not obtained.

Table 7.3: Comparison of how accurate the numerical models in Abaqus is at predicting total failure of the tested plates.

| | P1_15 | P3_35 | S1_15 | S2_25 |
|---------------------|--------------|--------------|--------------|------------------|
| Experimental | Not failure | Failure | Failure | Close to failure |
| Simulation | Failure | Failure | Failure | Failure |

Table 7.4: Failure modes obtained with Abaqus for the four different configurations. The deformation and crack propagation are shown at three chosen times for all simulations resulting in failure of the plates.



7.3. Validation of Abaqus models

All evaluated crack lengths from the experimental work in Chapter 6.2.8 has been compared to the numerically obtained results in this section and is given in Table 7.5. In this table, it is seen that the length of the predicted cracks is consistently overestimated. Although overestimated, the lengths of the predicted cracks are comparable to the experimental results for many of the simulations. The lowest deviation between the numerical end the experimentally obtained crack length is for the S1_10 simulation where the crack length for the O-crack is overestimated with approximately 20% and the S1_05 simulation where the simulated result is 1.1 mm cracks compared to pure necking experimentally. The least accurate crack representation is for the P1 configuration. For the P1_10 simulation, the crack length is overestimated by a factor of 2.7.

Table 7.5: Crack data for all simulations using the geometrically complex Abaqus model is compared to the experimental results. The crack names are referring to the naming convention given in Figure 6.29. From the simulations, only one crack length is given due to the symmetric model. In the table, (N) indicates pure necking, (X) indicates a crack that is too large and twisted to be measured, and (-) indicates that the simulation resulted in complete failure.

| Test | Experimental | | | | | | | | Abaqus | |
|-------|--------------|------|------|------|------|------|------|------|--------|------|
| | O1 | O2 | O3 | O4 | I1 | I2 | I3 | I4 | O | I |
| S2_10 | N | N | N | N | 4.4 | 4.7 | 4.3 | 4.2 | 1.1 | 5.3 |
| S2_15 | 5.1 | 4.4 | 4.7 | 4.8 | 11.4 | 10.8 | 10.9 | 10.3 | 5.5 | 14.5 |
| S2_25 | 22.8 | 22.2 | 21.2 | 22.5 | X | X | X | X | - | - |
| | H1 | H2 | H3 | H4 | V1 | V2 | V3 | V4 | H | V |
| S1_05 | N | N | N | N | N | N | N | N | 1.1 | 1.1 |
| S1_10 | 5.1 | 5.4 | 6.2 | 5.8 | 7.2 | 7.9 | 7.5 | 7.4 | 9.3 | 9.0 |
| | O1 | O2 | O3 | O4 | I1 | I2 | I3 | I4 | O | I |
| P3_25 | N | N | N | N | 2.0 | 2.4 | 1.6 | 2.2 | 1.5 | 6.3 |
| | O1 | O2 | O3 | O4 | | | | | O | |
| P1_05 | N | N | N | N | | | | | 1.5 | |
| P1_10 | 6.1 | 6.2 | 6.4 | 6.1 | | | | | 16.9 | |
| P1_15 | 25.0 | 26.0 | 22.7 | 22.3 | | | | | - | |

7.3.2 Evaluation of displacements

To evaluate the numerically obtained results, the calculated displacements will be compared to what was in the experimental work. Plots of the midpoint displacement are included for all combinations of configuration and firing pressure except the ones that resulted in failure experimentally. This is presented in Figure 7.2.

The experimental and the numerical midpoint displacements are plotted on a synchronized time axis through the calculated shock wave velocities. As stated in Section

6.2.2, the reference time is zero as the incoming shock wave passes the sensor closest to the plate. To obtain the equivalent time axis, the time consumed by the shock wave between the closest sensor and the plate is added to the numerical data. These time estimates are given in Table 6.4. As seen in Figure 7.2, the numerical response is qualitatively very similar to the experimental data after the time axis has been adjusted.

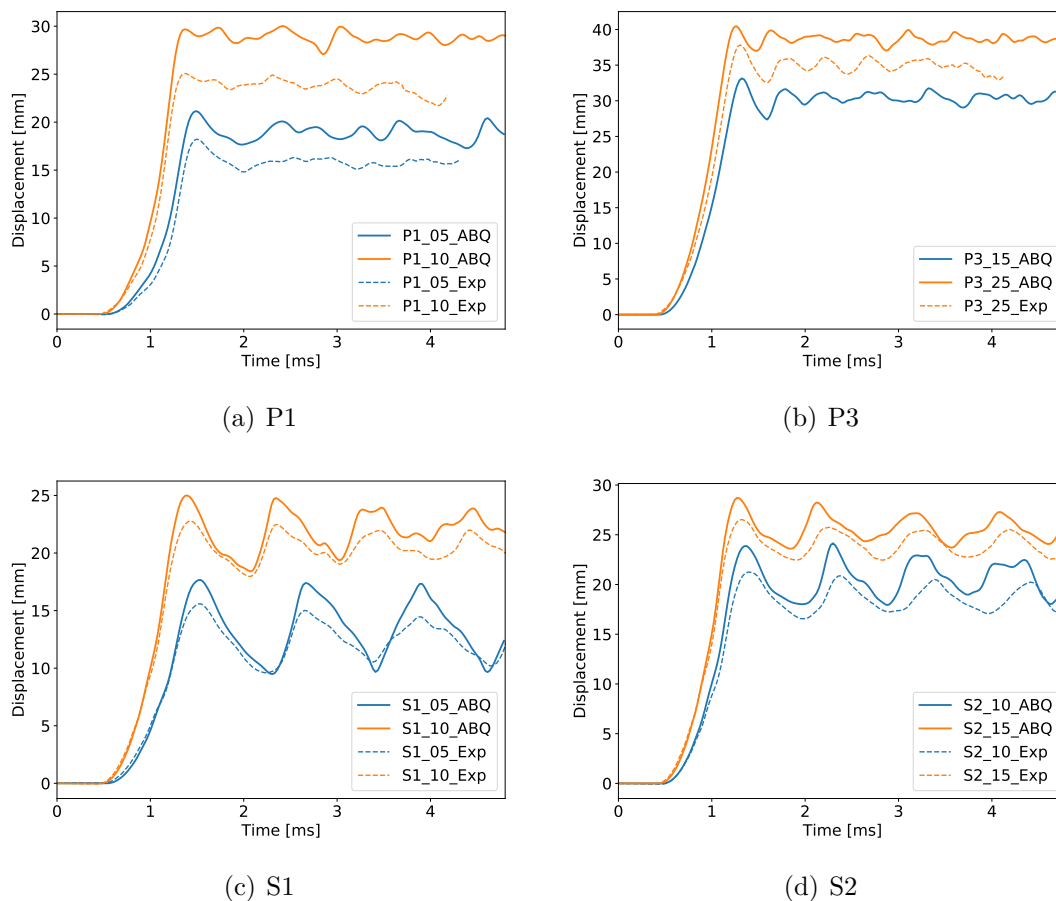


Figure 7.2: Midpoint displacements vs. time for experimentally obtained data compared to pure Lagrangian model in Abaqus. Dotted lines represents the experimentally obtained data.

The numerically predicted response is consistently larger than in the experiments. This is in agreement with previous numerical studies conducted at NTNU, as mentioned in Chapter 4. In Table 7.6 the maximum midpoint displacement is compared between the geometrically complex Abaqus model and the experimental results. To evaluate the difference between using the geometrically complex or simple models, results from Chapter 4 has also been included for equivalent element formulations and sizes. The evolution of the displacement profiles for two representative tests is included in Figure 7.3. As seen, the numerically and experimentally obtained profiles are qualitatively very similar.

7.4. Comparison of Lagrangian models in Abaqus and Europlexus

When treating all perforated simulations as one group, it is seen in Table 7.6 that the complex geometry representation increases the displacement with approximately 10%, compared to the simple representation. This is in agreement with the results in the master thesis by Granum and Løken [29]. For the group containing all slitted configuration, the deviation is approximately 14%. Within both groups, the deviation seems to be almost constant for different firing pressures. All geometrically complex models overestimate the response, but for the simple model, this is only true for the P1 configuration when loaded with the lowest firing pressures. The deviations between the numerical models and the experimental results are not constant for either the simple or the complex model.

Table 7.6: Deviation in maximum midpoint displacement, given in [%]. Between the experimental data and the clamped models from Part I of the preliminary study, the experimental data and the geometrically complex model, and the clamped models from Part I of the preliminary study and the geometrically complex model.

| Test | Clamped & Experimental [%] | Complex & Experimental [%] | Clamped & Complex [%] |
|-------|----------------------------------|----------------------------------|-----------------------------|
| P1.05 | -5.8 | -17.8 | 10.2 |
| P1.10 | -5.1 | -17.7 | 10.7 |
| P3.25 | 4.0 | -6.7 | 10.0 |
| S1.05 | 2.9 | -13.3 | 14.3 |
| S1.10 | 4.9 | -11.1 | 14.4 |
| S2.10 | 3.8 | -12.8 | 14.7 |
| S2.15 | 8.3 | -6.8 | 14.2 |

7.4 Comparison of Lagrangian models in Abaqus and Europlexus

As stated earlier in this chapter, the initial goal was to validate the geometrically complex CEL models through a comparison with the experimental results. For a thorough validation, it was decided to address all deviations in structural response purely related to the change of solvers, before including FSI. However, due to the difficulties experienced in Europlexus regarding the geometrically complex CEL simulations, the main focus was slightly changed. This section was obtained prior to the encountered bug, and it was decided to still include this part as the results may be of importance for future studies.

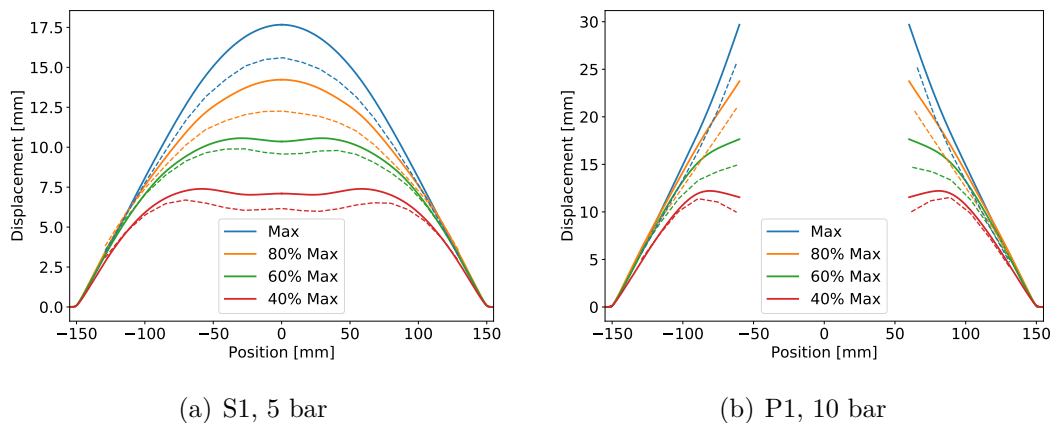


Figure 7.3: Deformation profiles for experimentally obtained data compared to the pure Lagrangian model in Abaqus. Dotted lines represent the experimentally obtained data.

The midpoint displacements obtained when running the geometrically simple and complex Lagrangian analysis in Europlexus is compared to the Lagrangian Abaqus models in Figure 7.4.

In Figure 7.4, an interesting observation is that the results for the geometrically complex model in Europlexus are consistently softer than the results obtained in Abaqus. It is important to note that both models apply the exact same material parameters and friction coefficient. Because the implementation of the boundary, with respect to the contact formulation and the modeling of the bolt loads, differed between the models, the geometrically simple model was included for comparison. As seen in Figure 7.4, even the geometrically simple models in Europlexus gives a softer response than the Abaqus models. This result excludes the boundary from being the explanation of the deviation between the models.

In Table 7.7, the maximum displacements shown in Figure 7.4 is given. This table also states the deviation between corresponding simulations, as well as the mean deviation between the Abaqus models and the two types of Europlexus models. It is seen that the mean deviation between all geometrically complex Europlexus models and the corresponding Abaqus models is 7.7%. When comparing this deviation to results from previously conducted parametric studies, the effect of changing solvers is qualitatively resulting in deviations in the same range as the effect of changing from a simple to a complex geometrical model in Abaqus.

When predicting the capacities of the plates, the geometrically complex models in Europlexus are in good agreement with the results from Abaqus. The Geometrically complex models in Europlexus repeats the findings presented in Table 7.3.

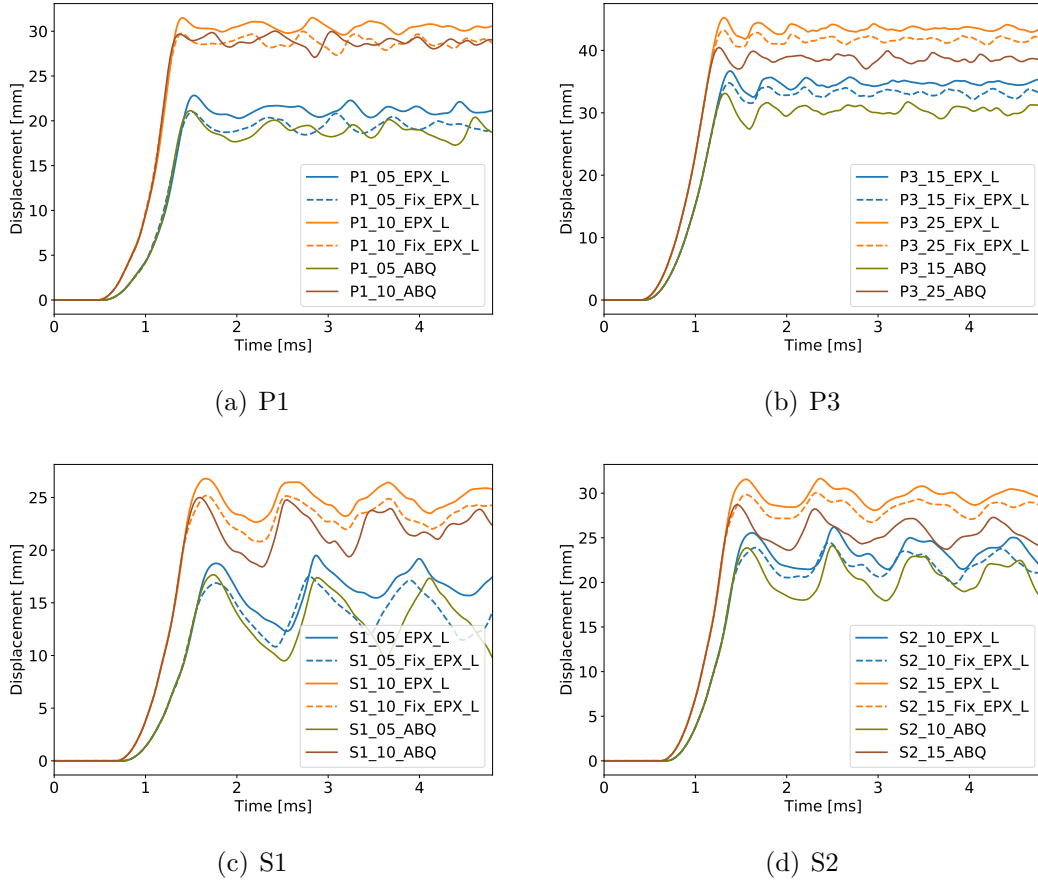


Figure 7.4: Comparison of midpoint displacement response for Lagrangian analyses run in Abaqus and Europlexus. For the models in Europlexus both the geometrically simple and the complex models in Europlexus are included.

7.5 Fluid structure interaction effects

This section aims to compare the coupled Eulerian-Lagrangian simulations to the purely Lagrangian simulations in Europlexus. As mentioned earlier in this chapter, the focus in this section will not be a detailed investigation on the capability in predicting the experimental response, but rather on how the inclusion of FSI changes the response between the pure Lagrangian and coupled Eulerian-Lagrangian simulations.

7.5.1 Midpoint displacement response

To evaluate the effect of including FSI, a comparison of the structural response for the simulations applying a Lagrangian description is compared to CEL models. Due to the fact that the structural domain is discretized in an equal manner for the two approaches, any deviations in the response may be related directly to the representation of the loading.

Table 7.7: Deviation in maximum midpoint displacement between the models in Europlexus and Abaqus. Both the simple and the geometrically complex models in Europlexus is compared to the models in Abaqus. The total mean of all deviations within the two groups is also included.

| Test | Europlexus complex& | Europlexus simple & |
|----------------|---------------------|---------------------|
| | Abaqus [%] | Abaqus [%] |
| P1_05 | 7.4 | -0.8 |
| P1_10 | 5.7 | 0.2 |
| P3_15 | 9.7 | 4.7 |
| P3_25 | 10.5 | 6.4 |
| S1_05 | 5.7 | -4.7 |
| S1_10 | 6.7 | 0.7 |
| S2_10 | 6.6 | 0.1 |
| S2_15 | 9.0 | 3.8 |
| Mean deviation | 7.7 | 1.3 |

In Figure 7.6, the midpoint displacements for the CEL and the pure Lagrangian models in Europlexus are plotted and compared. Because of an issue in Europlexus, some of the simulations aborted early and only the initial displacement peak was captured. All simulations compared are modeled with the simple boundary conditions. It should be noted that the simulations for P1_25, P3_35, P2_35, and S1_15 experienced complete failure for both modeling approaches and are therefore not included in the plots. The Lagrangian simulation for P1_15 and S2_25 are also excluded because the simulation predicts failure.

In Table 7.8 the obtained maximum midpoint displacements for both the CEL and the Lagrangian simulations are given, as well as the relative deviation between the two approaches given in [%]. It is seen that for most simulations the deviation is approximately 10%. The maximum deviation is found for the P1_10 simulation with a deviation of 10.92% and the lowest deviation is for the P3_25 simulation with only 4.79%. All simulations experiencing complete failure are excluded from Table 7.8. In Figure 7.5(a) and 7.6(c), it is seen that data is missing for the Lagrangian simulation of P1_15 and S2_25, and this is due to numerically predicted failure. Because the two different modeling approaches differ in the prediction of failure for these to combinations of configuration and firing pressure it could be argued that these are the simulations that deviate the most.

7.5. Fluid structure interaction effects

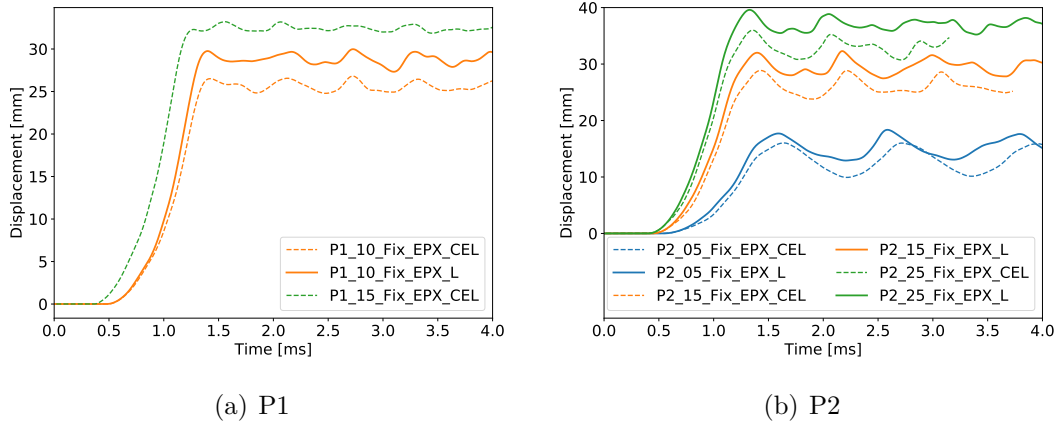


Figure 7.5: Comparison of midpoint displacement response for the CEL and the pure Lagrangian simulations in Europlexus for all configurations. The results are taken from the models using a simple fixed boundary of the blast-exposed area. Unfortunately, many of the CEL simulations exited before they had reached the total time, and this is the most evident for the P3 and S2 configuration.

Table 7.8: Comparison of the obtained maximum midpoint displacement between the coupled Euler-Lagrangian (CEL) and pure Lagrangian (L) simulations. The deviation in obtained results by using the two approaches is also indicated in the table.

| Configuration | MPD, max | MPD,Max | Deviation |
|---------------|----------|---------|-----------|
| | L | CEL | |
| | [mm] | [mm] | [%] |
| P1_10 | 29.76 | 26.51 | 10.92 |
| P2_05 | 17.71 | 16.03 | 9.49 |
| P2_15 | 32.01 | 28.86 | 9.84 |
| P2_25 | 39.60 | 35.98 | 9.14 |
| P3_15 | 34.78 | 32.68 | 6.04 |
| P3_25 | 43.24 | 41.17 | 4.79 |
| S1_05 | 16.88 | 15.44 | 8.53 |
| S1_10 | 25.18 | 22.69 | 9.89 |
| S2_10 | 23.89 | 21.87 | 8.46 |
| S2_15 | 29.84 | 26.86 | 10.00 |

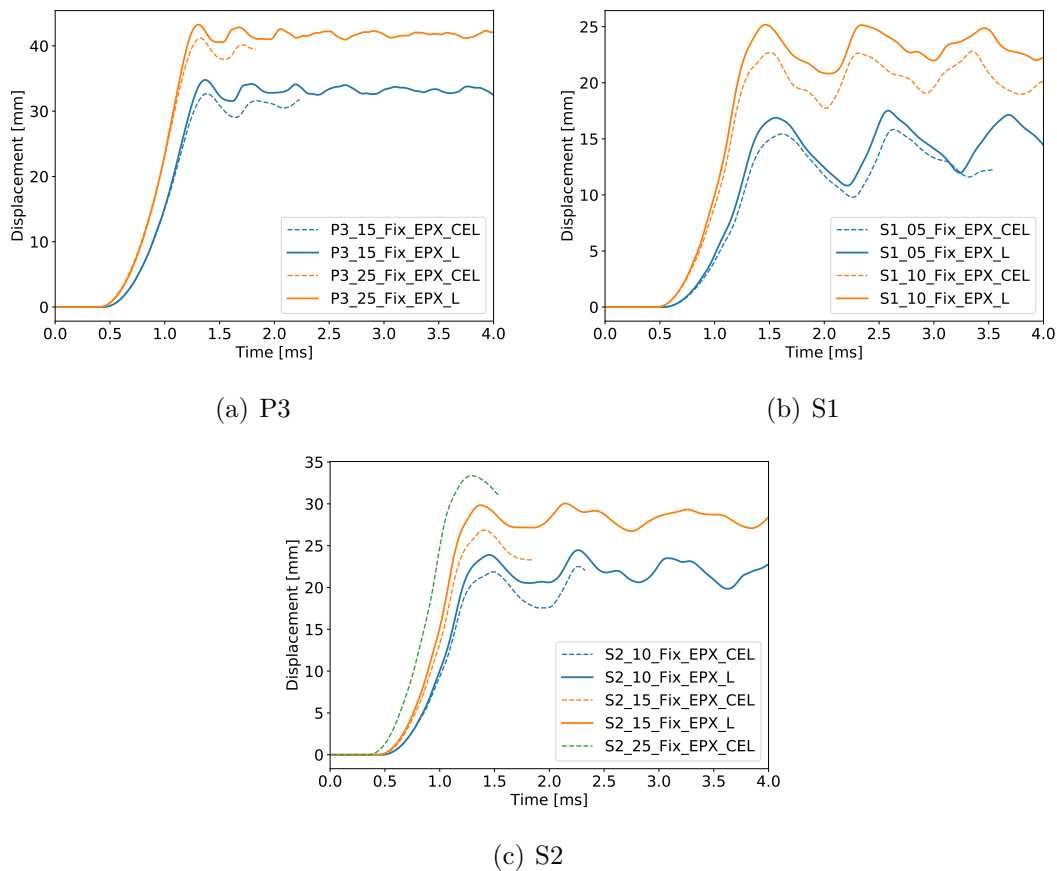


Figure 7.6: Comparison of midpoint displacement response for the CEL and the pure Lagrangian simulations in Europlexus for all configurations. The results are taken from the models using a simple fixed boundary of the blast-exposed area. Unfortunately, many of the CEL simulations exited before they had reached the total time, and this is the most evident for the P3 and S2 configuration.

7.5.2 Pressure evolution in front of the plates

To evaluate the obtained loading by including FSI, the pressure fields in front of the blast-exposed plates are shown in Figure 7.7 to 7.10. The field maps are shown for the following tests; P1.15, P2.25, P3.25, and S2.15. The S1 configuration is not included because the obtained behavior was very similar to what was found for the S2 configuration.

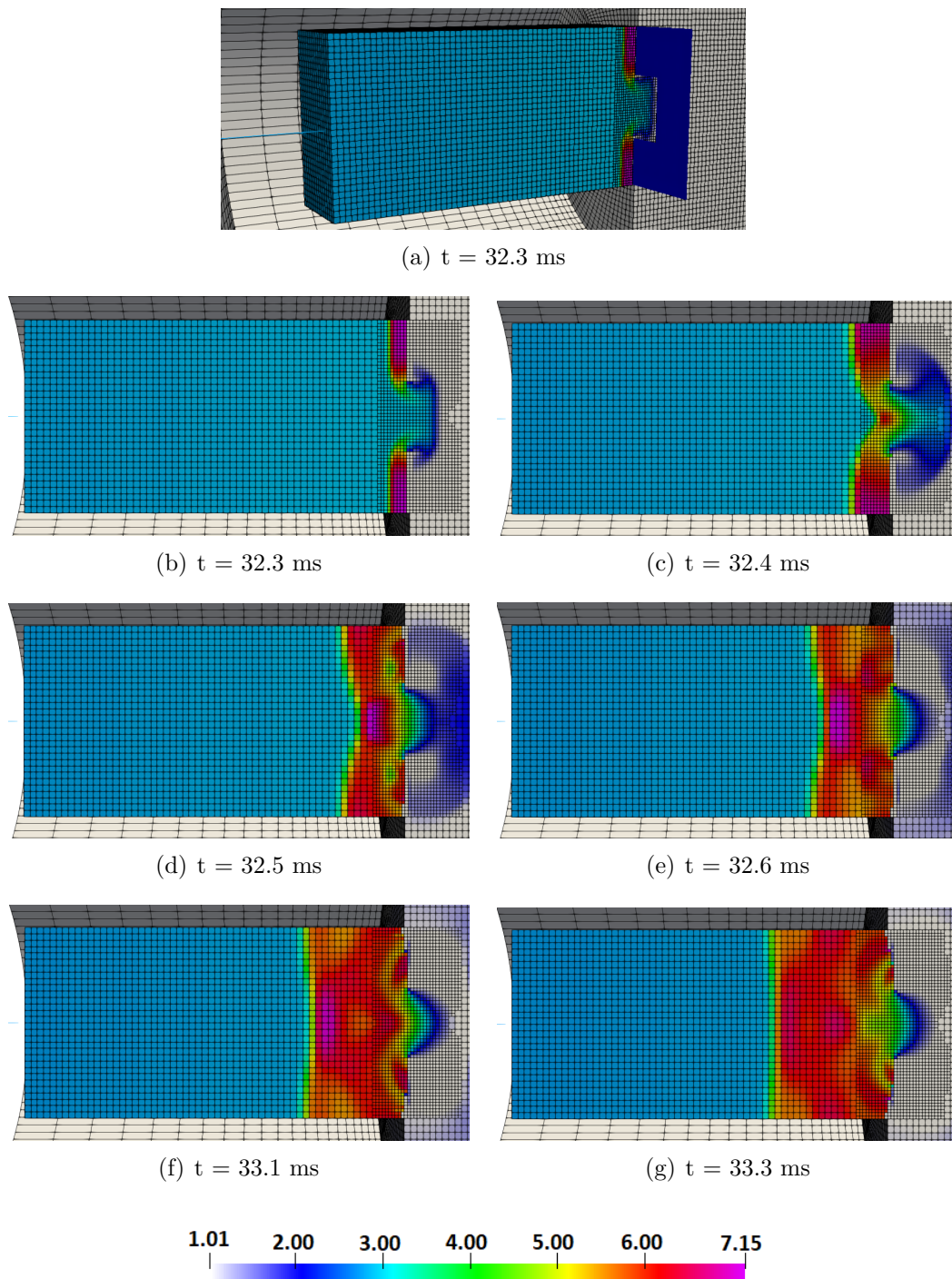


Figure 7.7: The pressure distribution in front of the P1 configuration at 15 bar is shown. The field maps are taken from the CEL simulations in Europlexus, The color shades represent the pressure in bar. All images are labeled with the total time in the simulation, which includes the propagation of the shock wave before reaching the plate. The presented field maps are taken from the cut given in image (a), and the grey mesh represent the air initially at rest in the dump tank.

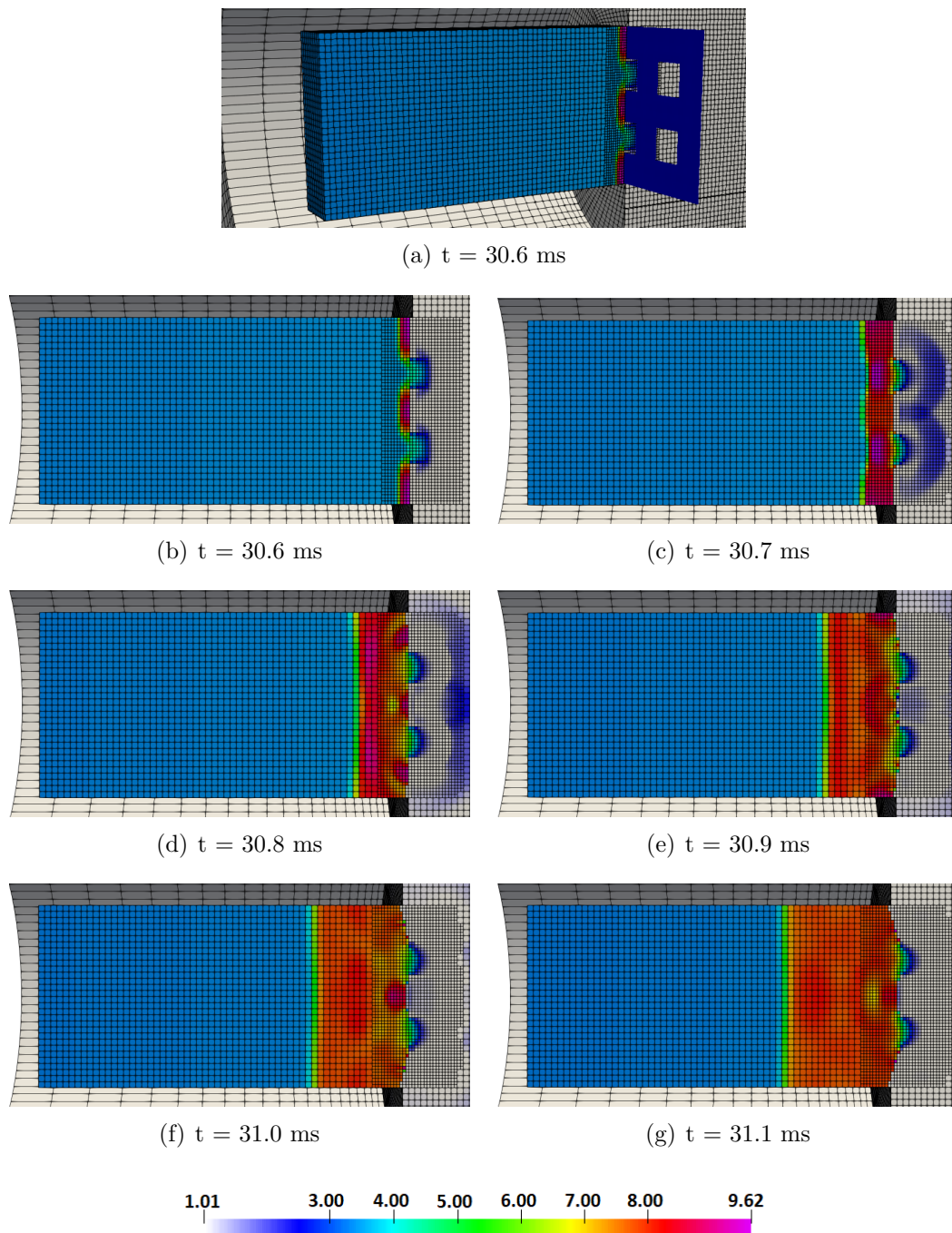


Figure 7.8: The pressure distribution in front of the P2 configuration 25 bar is shown. The field maps are taken from the CEL simulations in Europlexus, and the color shades represent the pressure in bar. All images are labeled with the total time in the simulation, which includes the propagation of the shock wave before reaching the plate. The presented field maps are taken from the cut given in image (a), and the grey mesh represent the air initially at rest in the dump tank.

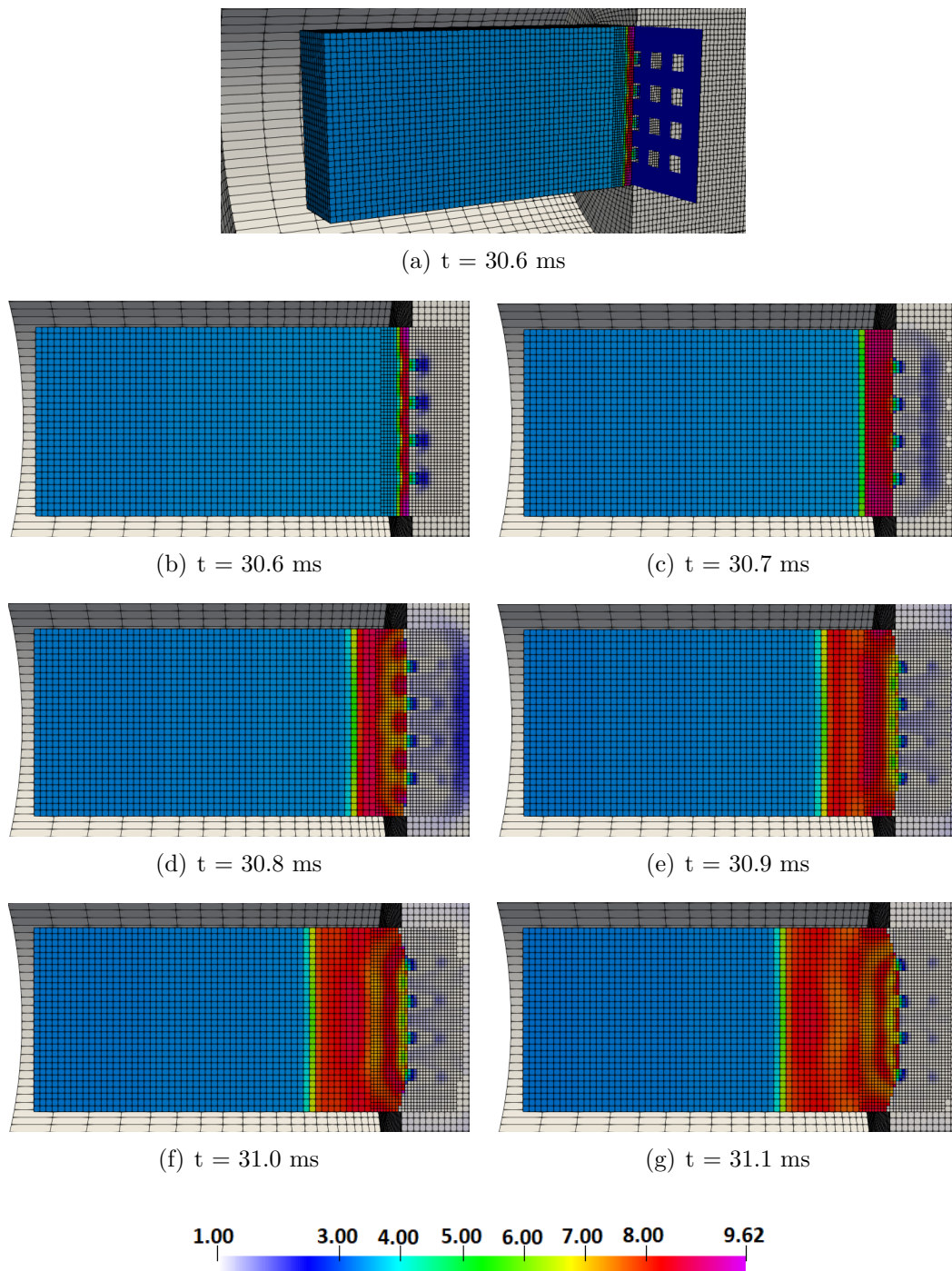


Figure 7.9: The pressure distribution in front of the P3 configuration at 25 bar is shown. The field maps are taken from the CEL simulations in Europlexus, and the color shades represent the pressure in bar. All images are labeled with the total time in the simulation, which includes the propagation of the shock wave before reaching the plate. The presented field maps are taken from the cut given in image (a), and the grey mesh represent the air initially at rest in the dump tank.

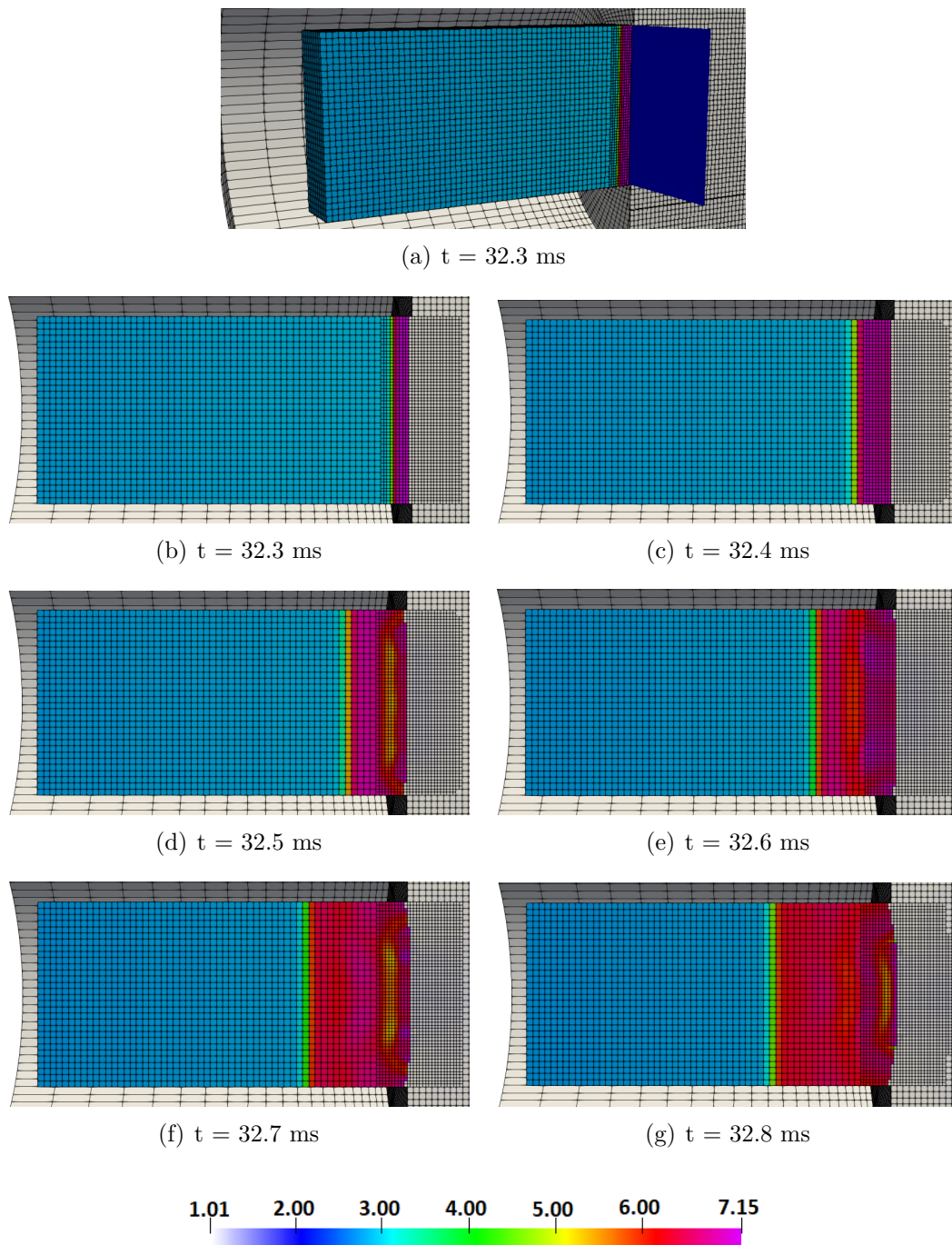


Figure 7.10: The pressure distribution in front of the S2 configuration at 15 bar is shown. The field maps are taken from the CEL simulations in Europlexus, and the color shades represent the pressure in bar. All images are labeled with the total time in the simulation, which includes the propagation of the shock wave before reaching the plate. The presented field maps are taken from the cut given in image (a), and the grey mesh represents the air initially at rest in the dump tank. Note that the slits are not visible in the undeformed configuration.

Figure 7.7 to 7.10 indicates that the geometry of the different plate configurations affect the pressure build up in front of the blast-exposed plates differently. The pressure fields for the perforated configurations show similar features and stand out compared to the slitted configurations. With reference to Figure 7.7(b), parts of the shock wave passes through the centered perforation in the P1 plate in the initial part of the interaction. After passing through the perforation, parts of the shock front are still planar but the profile of the pressure front changes quickly. Within a time span of 0.1 ms the profile changes from partly planar into a mushroom-like shape, and as a less intense pressure wave propagates into the dump tank, the pressure profile over the perforation takes the shape of an arch. This evolution is seen in Figure 7.7(c) to 7.7(g).

The initial propagation for the shock wave, as described for the P1 configuration, is very similar for the P2 and the P3 configuration. The difference is that the pattern repeats two and three times respectively. Although similar, the evolution of the P3 configuration, shown in Figure 7.9(b) to 7.9(g), differ by having an initially higher pressure across the perforations. The simulated trend seems to be that many small perforations are less suited for letting particles through than few larger ones.

When evaluating the pressure field in front of the perforated plates, the pressure seems to build up in a less uniform manner due to the flow through the perforations. This is especially evident in Figure 7.7(c) and 7.7(d) for P1, Figure 7.8(b) to 7.8(e) for P2 and Figure 7.9(d) to 7.9(f). These figures imply that the pressure field across the blast-exposed area of the perforated plates is distributed in a non-uniform manner, and the effect seems to be the most significant for P1. Here it is seen that the pressure loading on the blast-exposed surface varies with the radial distance from the perforation. The variation in pressure is approximately 2.15 bar from the edge of perforation to the clamped edge of the plate. Relative to the maximum pressure in this pressure field, the difference is 30%. The fact that the pressure is far from uniform for the P1 plates is thought to be a major contributor to why the CEL and the pure Lagrangian simulations differ for this configuration.

For the S2_15 simulation, shown in Figure 7.10, the pressure distribution is more uniform than what is seen for the perforated plates. The S1_10 configuration showed a similar behavior and can be found in the appendix. The simulations for the slitted configurations did not result in pressure waves passing through the slits in the plates. This might be due to a relatively coarse fluid mesh compared to the size of the slit opening. As stated in Chapter 2, the embedded FSI approach is sensitive to the relative size of the fluid mesh compared to the structure it interacts with. To illustrate this, Figure 7.11 is included. In this figure, it is clearly seen that no air passes through the slits even as they open up. The same effect can possibly be important for the P3 configuration as well, due to its small perforations.

With reference to Table 7.8, it is evident that the only configuration group that stands out significantly with respect to the deviation between the Lagrangian and the CEL simulations is the P3 configuration. The mean deviation when treating all

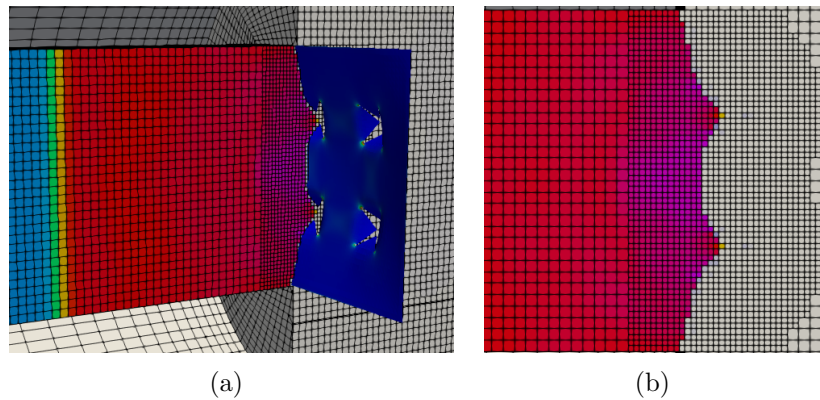


Figure 7.11: It is seen that the fluid mesh is too coarse to let air pass through the opened slits for the S2 configuration. The images are taken from the S2_15 simulation in Europlexus at $t = 33.2$ ms. (a) The image includes the blast-exposed S2 plate. (b) Pressure profile in the cut seen from the side. The pressure field values are excluded for this figure.

P3 simulations as a group is 5.6%, whereas it is 9.41% and 9.22% when treating P1 and P2, and both slitted configurations as one group respectively. It is interesting to note that when comparing the complex Abaqus model to the experimental results in Table 7.6, the P3_25 test deviate from the Lagrangian Abaqus model with 6.7%, and the slitted configurations deviate with 11% if treated as a group. The P1 configurations deviate with 17.8% when treated as a group. This indicates that it is indeed true that the P3 configuration is the one configuration that is the least prone to the FSI effects.

7.6 Concluding remarks

The geometrically complex Abaqus models, using a pure Lagrangian description was found to be in good agreement with the experimental results. For experimental tests not experiencing failure, the deviation between the simulated and the experimental midpoint displacement was approximately 10% and 14% for the perforated and the slitted configurations respectively. The deviation was a result of the numerical models consistently overestimating the displacements. This finding is in agreement with previous work conducted by both Granum and Løken [29], and Aune [3].

When evaluating failure modes and cracking, the Abaqus models were capable of predicting the exact failure load for two out of four tests. The predicted failure load was not correct for the P1 and the S2 configuration. However, the S2 configuration was observed to be on the limit to failure when exposed to the predicted failure loading in the SSTF. The crack lengths predicted with the Abaqus models was consistently found to be larger than the experimentally measured results and makes the overall

prediction of capacity conservative.

The comparison between the Lagrangian models in Abaqus and Europlexus revealed that the models in the two solvers differ in their prediction of the midpoint displacement with an average deviation of 7.7%. However, the prediction of the critical pressure and failure modes coincides for both solvers.

Even though some difficulties were encountered for the simulations run in Europlexus, the results were promising. By inspecting the pressure field in front of the plates, the CEL analyses indicated that the different configurations are experiencing non-uniform pressure distributions, which deviates from the applied loadings in the pure Lagrangian analyses.

Chapter 8

Concluding remarks

This chapter aims to draw the lines between all the work done in the context of this thesis. A brief summary of the work, as well as a discussion of the most important findings and experiences, will be presented. Specific details from each chapter will not be repeated here, as both of the preliminary studies, the chapter on experimental work and the last numerical chapter are all ended with concluding remarks.

8.1 Summary and discussion

The main objective of this thesis was to determine how thin perforated steel plates behave under blast-loading and to validate to which extent this can be predicted using computational tools. The starting point was to perform a thorough preliminary numerical study on the structural response of the steel plates, prior to the experimental work. Through this study, the test matrix for the experiments in the SSTF was determined. Four configurations were decided, two with preformed holes and two containing slits. Each configuration was tested at three different pressure levels, intended to provoke different behaviors. To evaluate the experimental work, all experiments were recorded through the use of two high-speed cameras, pressure measurements and a laser scanner. The experimental testing was followed by a final numerical study. Lagrangian analyses in Abaqus was validated through a comparison with the experiments, and the effect of including fluid-structure interaction in the numerical work was explored.

A comprehensive literature review, where the representation of a blast loading, modeling techniques for both the structural and fluid sub-domains, shock tube theory as well as previously conducted studies on the topic was evaluated. This thesis mainly serves as a continuation of the work done by Aune in his PhD thesis, the work he does as an associate professor at NTNU, and the work done by Granum and Løken in their masters thesis [29].

The two perforated configurations, P1 and P3 were chosen to study the effect of

different distributions of a fixed total hole area. The findings through both the experimental work and the CEL analyses suggest that problem is less prone to FSI effects as the hole size in the plates is being decreased. The P1 configuration was found to be the most susceptible configuration for FSI, while P3 was the least. It was not studied whether it was the reduced stiffness or the relative size of the perforations in the plate that governs the FSI effects.

In the preliminary numerical study, presented in Chapter 4 and 5, a trusted material model as well as a validated description of the loading histories was available. This resulted in accurate numerical predictions prior to the experimental testing. This shows that for the investigated blast-loaded steel plates, it is possible to obtain good results with pure Lagrangian models. When only evaluating the structural response, the inclusion of FSI through CEL analyses did not result in any significant changes in behavior. However, the combined modeling of fluid and structure allow for a much deeper insight into the physics governing the behavior, and the phenomenon of blast-loading to be studied in detail.

In the numerical work conducted with Lagrangian models in Abaqus, three parameters were given special attention. The first part of the study focused on the discretization of the blast-loaded plates by investigating the effect of different element sizes and formulations. Secondly, the effect of different representations of the boundary condition was instigated. Lastly, strain rate sensitivity parameter in the modified Johnson-Cook equation was studied.

When exposed to blast loadings below the failure capacity, the parametric study on element size and formulation revealed that the global deformation of the blast-exposed plates is equally represented for fine and coarse discretizations. The plates are resisting the motion induces by the blast load through membrane forces, and as long as the cracks are small, they do not significantly decrease the stiffness of the plates. This makes the coarsely discretized models capable of predicting the displacements with good accuracy but to capture the failure phenomenon, a fine discretization of the plates are required.

It is interesting to note that how one chooses to evaluate the FSI effect may be of great importance. Through the experimental work in Chapter 2, it is indicated that the P3 configuration exhibit the structural response resulting in the lowest reflected peak pressures. Although this was never rigidly confirmed, due to the premature firing of the system. It indicates that the geometry of the P3 configuration changes the fluid behavior noticeably compared to the other configurations. The pressure measured by the sensor 24.5 cm upstream the plate differ the most from the calibration experiments for this configuration. This indicates an FSI effect, but P3 is actually the configuration that is most accurately predicted with the pure Lagrangian models, and also the configuration with least difference between CEL and Lagrangian analysis. The latter could be argued to indicate the absence of FSI effects for this configuration. The contradicting results imply that to evaluate the FSI effects for

the fluid and for the structure should be treated separately. It seems like the geometry of the P3 configuration interact with the shock wave in a way that effectively changes the pressure field, at least when evaluating 24.5 cm away, but in such a way that the effective loading felt by the plate is very similar to what a rigid plate would have experienced. The possible mechanism might be evaluated by running the geometrically complex CEL model and doing a detailed sampling of the pressure on the blast-exposed plate. This could then be compared to the pressure measurements conducted on the massive steel plate tested by Aune [3].

8.2 Conclusions

This section will briefly conclude on the most important findings obtained through the work on this thesis.

- Due to available results from previous work and validated loading curves, reliable Lagrangian models were established in the preliminary study prior to testing in the SSTF.
- The chosen defects in the plates provoked FSI effects. This was confirmed through both experimental tests and the numerical study applying CEL models.
- Overall, the calibrated material parameters and constitutive relation describing the behavior of the Docol 600DL steel plates gave good results.
- Changes in the strain rate sensitivity parameter described in the modified Johnson-Cook constitutive relation affected the stiffness, capacity and failure modes observed for the numerical models.
- For the Lagrangian analyses in Abaqus, the inclusion of the clamping frames and bolts to the numerical models resulted in noticeably increased displacements compared to models applying fixed boundary conditions.
- The experiments in the SSTF served as a great tool for validating the applied numerical models, and the comparison of 3D-DIC and the laser measurements showed that the two techniques coincide.

8.3 Further work

The results obtained in this thesis suggest that different distributions of the holes in the perforated configurations change the fluid-structure interaction. Although CEL analysis was run, it has not been concluded whether this is related to the flow going through the holes, or if it is related to the structural response. An interesting study would, therefore, be to conduct tests on perforated 5 cm rigid steel plates. This allows for the effect of different hole setups to be studied in an isolated manner. By excluding the material behavior of the structural domain, this could also thoroughly validate the simulations of the fluid sub-domain.

Three different values of the strain rate sensitivity in the modified Johnson-Cook equation was applied in this thesis. Conducted simulations indicate that the different values of c are considerable affecting the behavior both regarding the stiffness and the capacity of the plates. This is an interesting parameter to investigate, as shown by Rakvåg [27], and may be hard to determine experimentally.

In Chapter 7 Lagrangian simulations in Abaqus and Europlexus was compared. The results obtained in Europlexus showed a significantly softer behavior than what was found in Abaqus. Due to the fact that both solvers applied identical material cards, and boundary conditions, it could be interesting to perform a more comprehensive comparative study to identify the differences between the two solvers.

References

- [1] T. Børvik V. Aune and M. Langseth. *An Introduction to Blast Mechanics*. 2016.
- [2] P. Smith D. Cormie G. Mays. *Blast effects on buildings*. Thomas Telford, 1995.
- [3] V. Aune. “Behaviour and modelling of flexible structures subjected to blast loading”. PhD thesis. Department of Structural Engineering, Norwegian University of Science and Technology - NTNU, 2017.
- [4] M. Langseth V. Aune E. Fagerholt and T. Børvik. “A shock tube facility to generate blast loading on structures”. In: *International Journal of Protective Structures* 7.3 (2016), pp. 1–31.
- [5] D. Rubin W. M Lai and E Kreml. *Introduction to Continuum Mechanics*. Butterworth-Heinemann, 2010.
- [6] SAS IP Inc. *Lagrangian and Eulerian Reference Frames*. URL: https://www.sharcnet.ca/Software/Ansys/16.2.3/en-us/help/wb_sim/exp_dyn_theory_lag_eul_360.html (visited on 03/05/2018).
- [7] M. E Plesha R. D. Cook D. S. Malkus and R. J. Witt. *Concepts and Applications of Finite Element Analysis*. Wiley, 2001.
- [8] O. S. Hopperstad and T. Børvik. *Impact Mechanics - Part 1. Modelling of plasticity and failure with explicit finite element method*. 2017.
- [9] W. K. Liu T. Belytschko and B. Moran. *Nonlinear Finite Elements for Continua and Structures*. Wiley, 2000.
- [10] ABAQUS. *Lecture 1, Overview of ABAQUS/Explicit, by ABAQUS*. URL: <https://pdfs.semanticscholar.org/presentation/afcd/576d8b8c92b7475b58c2952f8c0a3a9805.pdf> (visited on 03/06/2018).
- [11] DYNA support. *LS-DYNA support, Hourglass*. URL: <https://www.dynasupport.com/howtos/element/hourglass> (visited on 03/06/2018).
- [12] J. L. Lacombe A. G. Hanssen J. Petit L. Olovsson J. Limido. “Modeling Fragmentation With New High Order Finite Element Technology and Node Splitting”. In: *The European Physical Journal Conferences Web of Conferences* 94 ().
- [13] F. Casadei M. Langseth V. Aune G. Valsamos and T. Børvik. “On the dynamic response of blast-loaded steel plates with and without pre-formed holes”. In: *International Journal of Impact Engineering* 108 (2017), pp. 27–46.

References

- [14] F. Casadei P. Diez F. Verdugo. “An algorithm for mesh refinement and unrefinement in fast transient dynamics”. In: *International Journal of Computational Methods* 10 (2013), pp. 1–31.
- [15] *SIMULIA User Assistance 2017, section; Interactions*. Dassault Systemes Simulia Corp.
- [16] Europlexus. *Europlexus Users Manual*. URL: http://europlexus.jrc.ec.europa.eu/public/manual_pdf/manual.pdf (visited on 01/06/2018).
- [17] T. Belytschko and M.O. Neal. “Contact-impact by the pinball algorithm with penalty and Lagrangian methods”. In: *International Journal for Numerical Methods in Engineering* 31.3 (1991), pp. 3–12.
- [18] T. Belytschko and S.E. Law. “An assembled surface normal algorithm for interior node removal in three-dimensional finite element meshes”. In: *Engineering with Computers* 1.1 (1985), 55–60.
- [19] F. Casadei M. Langseth T. Børvik V. Aune G. Valsamos. “On the dynamic response of blast-loaded steel plates with and without pre-formed holes”. In: *International Journal of Impact Engineering* 108 (2017), pp. 27–46.
- [20] DASSULT systemes. *SIMULIA Abaqus 2016 Theory Guide, Section 5.2.3 Coulomb friction*. URL: <http://ivt-abaqusdoc.ivt.ntnu.no:2080/v2016/books/stm/default.htm?startat=ch04s04ath117.html> (visited on 01/06/2018).
- [21] continuummechanics.org. *Navier-Stokes Equation*. URL: www.continuummechanics.org/navierstokes.html.
- [22] F. M. White. *Viscous Fluid Flow*. McGraw-Hill, 2005.
- [23] E. F. Toro. *Riemann Solvers and Numerical Methods for Fluid Dynamics*. Springer, 2009.
- [24] F. G. Friedlander. *The diffraction of sound pulses I. Diffraction by a semi-infinite plane*. Proceedings of the Royal Society A: Mathematical, Physical and Engineering Science.
- [25] C. N. Kingery and G. Bulmash. *Airblast Parameters from TNT Spherical Air Burst and Hemispherical Surface Burst*. National government publication. Defence Technical Information Center, Ballistic Research Laboratory, Aberdeen Proving Ground, Maryland.
- [26] M. Larcher F. Casadei and N. Leconte. “Strong and Weak Forms of a Fully Non-conforming FSI Algorithm in Fast Transient Dynamics for Blast Loading of Structures”. In: *Proceedings of the 3rd International Conference on Computational Methods in Structural Dynamics and Earthquake Engineering COMP-DYN 2011* (2011), 1120–1139.
- [27] K.G. Rakvåg. “Combined Blast and fragment loading on steel plates”. PhD thesis. Department of Structural Engineering, Norwegian University of Science and Technology - NTNU, 2013.

-
- [28] T.M Djupvik C. Baglo. “Experimental and Numerical Study on Plated Structures Subjected to Blast Loading”. MA thesis. Department of Structural Engineering, Norwegian University of Science and Technology - NTNU, 2015.
- [29] L.M Løken H.M. Granum. “Experimental and Numerical Study on Perforated Steel Plates Subjected to Blast Loading”. MA thesis. Department of Structural Engineering, Norwegian University of Science and Technology - NTNU, 2016.
- [30] S.T Thorgeirsson J.M. Stensjøen. “An Experimental and Numerical Investigation of the Blast Response of Pre-damaged Aluminum Plates”. MA thesis. Department of Structural Engineering, Norwegian University of Science and Technology - NTNU, 2017.
- [31] H. Zhu Z. Wu Y. Li W. Wu and Z. Du. “The influence of different pre-formed holes on the dynamic response of square plates under air-blast loading”. In: *Engineering Failure Analysis* 78 (2017), 122–133.
- [32] F. Casadei M. Larcher M. Langseth V. Aune G. Valsamos and T. Børvik. “Use of damage-based mesh adaptivity to predict ductile failure in blast-loaded aluminium plates”. In: *Procedia Engineering* 197 (2016), pp. 3–12.
- [33] O. S. Hopperstad and T. Børvik. *Material Mechanics, Part 1*. 2016.
- [34] O. S. Hopperstad G. Gruben E. Fagerholt and T. Børvik. “Fracture characteristics of a cold-rolled dual-phase steel”. In: *European Journal of Mechanics A/Solids* 30 (2011), 204–218.
- [35] O. S. Hopperstad G. Gruben and T. Børvik. “Evaluation of uncoupled ductile fracture criteria for the dual-phase steel Docol 600DL”. In: *International Journal of Mechanical Sciences* 62 (2012), 133–146.
- [36] O. S. Hopperstad J. K. Holmen and T. Børvik. “Low velocity impact on multi-layered dual-phase steel plates”. In: *International Journal of Impact Engineering* 78 (2015), 161–177.
- [37] G.K. Schleyer T. Børvik K.G. Rakvåg N.J. Underwood and O.S. Hopperstad. “Transient pressure loading of clamped metallic plates with pre-formed holes”. In: *International Journal of Impact Engineering* 53 (2013), pp. 44–55.
- [38] M. G. Cockcroft and D. J. Latham. “Ductility and the workability of metals”. In: *Journal of the Institute of Metals* 96 (1968), 33–39.
- [39] B. Müller. *Introduction to Computational Fluid Dynamics*. Lecture notes for the course Computational Heat and Fluid Flow. Department of Energy, Process Engineering, Norwegian University of Science, and Technology (NTNU), Aug. 2014.
- [40] E. F. Toro. *Riemann solvers and numerical methods for fluid dynamics*. Springer-Verlag, 2009.
- [41] engineeringtoolbox.com. *Properties of dry air*. URL: www.engineeringtoolbox.com/dry-air-properties-d_973.html (visited on 03/06/2018).

References

- [42] Y.A. Cengel and J.M. Cimbala. *Fluid Mechanics: Fundamentals and Applications*. McGraw-Hill, 2010.
- [43] *SIMULIA User Assistance 2017, section; Choosing a shell element*. Dassault Systemes Simulia Corp.
- [44] J. P. Lathama L. Guoa J. Xiang and B. Izzuddinb. “A numerical investigation of mesh sensitivity for a new three-dimensional fracture model within the combined finite-discrete element method”. In: *Engineering Fracture Mechanics* 15 (2016), pp. 70–91.
- [45] *SIMULIA User Assistance 2017, Section; What is the difference between the medial axis algorithm and the advancing front algorithm*. Dassault Systemes Simulia Corp.
- [46] *SIMULIA User Assistance 2017, Section; Three-dimensional solid element library*. Dassault Systemes Simulia Corp.
- [47] *SIMULIA User Assistance 2017, Section; Top-down meshing*. Dassault Systemes Simulia Corp.
- [48] *SIMULIA User Assistance 2017, Section; Abaqus/Explicit output variable identifiers*. Dassault Systemes Simulia Corp.
- [49] F. Casadei M. Larcher M. Langseth V. Aune G. Valsamos and T. Børvik. “Numerical study on the structural response of blast-loaded thin aluminium and steel plates”. In: *International Journal of Impact Engineering* 99 (2016), pp. 131–144.
- [50] Engineeringtoolbox. *Friction and Friction Coefficients*. URL: https://www.engineeringtoolbox.com/friction-coefficients-d_778.html.
- [51] E. Fagerholt. *eCorr v4.0 Documentation*. URL: <http://www.ntnu.edu/kt/ecorr> (visited on 05/06/2018).
- [52] Hexagon. *Home Page, Romer Absolute Arm, Laser measurements*. URL: <http://www.hexagonmi.com/en-GB/products/portable-measuring-arms/romer-absolute-arm> (visited on 03/05/2018).
- [53] G. Valsamos M. Langseth V. Aune F. Casadei and T. Børvik. “A shock tube used to study the dynamic response of blast-loaded plates”. In: ed. by The editor. 2018.

Bibliography

- [1] K.G. Rakvåg, N.J. Underwood , G.K. Schleyer , T. Børvik, O.S. Hopperstad. *Transient pressure loading of clamped metallic plates with pre-formed holes* In: "International Journal of Impact Engineering 53" (2013) pp: 44-55
- [2] C. Baglo, T.M Djupvik. Master Thesis: *Experimental and Numerical Study on Plated Structures Subjected to Blast Loading*, Department of Structural Engineering, Norwegian University of Science and Technology - NTNU (2015)
- [3] H.M. Granum, L.M Løken. Master Thesis: *Experimental and Numerical Study on Perforated Steel Plates Subjected to Blast Loading*, Department of Structural Engineering, Norwegian University of Science and Technology - NTNU (2016)
- [4] J.M. Stensjøen, S.T Thorgeirsson. Master Thesis: *An Experimental and Numerical Investigation of the Blast Response of Pre-damaged Aluminum Plates*, Department of Structural Engineering, Norwegian University of Science and Technology - NTNU (2017)
- [5] Y. Li, W. Wu, H. Zhu, Z. Wu, Z. Du *The influence of different pre-formed holes on the dynamic response of square plates under air-blast loading* In: "Engineering Failure Analysis 78" (2017) pp: 122–133
- [6] V. Aune, G. Valsamos, F. Casadei, M. Langseth, T. Børvik *On the dynamic response of blast-loaded steel plates with and without pre-formed holes* In: "International Journal of Impact Engineering 108" (2017) pp: 27-46
- [7] J.K. Holmen, O.S. Hopperstad, T. Børvik *Influence of yield-surface shape in simulation of ballistic impact* In: "International Journal of Impact Engineering 108" (2017) pp: 136-146
- [8] V. Aune, G. Valsamos, F. Casadei, M. Larcher, M. Langseth, T. Børvik *Use of damage-based mesh adaptivity to predict ductile failure in blast-loaded aluminium plates* In: "Procedia Engineering 197" (2017) pp: 3-12
- [9] V. Aune *Behaviour and modelling of flexible structures subjected to blast loading* Department of Structural Engineering, Norwegian University of Science and Technology - NTNU (2017)
- [10] O.S. Hopperstad & T. Børvik *Material Mechanics, Part 1*

Bibliography

- [11] O.S. Hopperstad & T. Børvik *Impact Mechanics - Part 1: Modelling of plasticity and failure with explicit finite element methods*
- [12] V. Aune, T. Børvik, M. Langseth *An Introduction to Blast Mechanics*
- [13] *eCorr v4.0 Documentation*. [ONLINE] Available at: <http://folk.ntnu.no/egilf/ecorr/doc/index.html> [Accessed 4 March 2018].
- [14] K.G. Rakvåg *Combined Blast and fragment loading on steel plates* Department of Structural Engineering, Norwegian University of Science and Technology - NTNU (2013)
- [15] *Home Page, Romer Absolute Arm, Laser measurements* Available at: <http://www.hexagonmi.com/en-GB/products/portable-measuring-arms/romer-absolute-arm>
- [16] T. Belytschko, M.O. Neal *Contact-impact by the pinball algorithm with penalty and Lagrangian methods* In: International Journal for Numerical Methods in Engineering Volume 31, Issue 3
- [17] T. Belytschko, S.E. Law *An assembled surface normal algorithm for interior node removal in three-dimensional finite element meshes* In: Engineering with Computers, Volume 1, Issue 1
- [18] *SIMULIA User Assistance 2017, section; Interactions* Publisher: Dassault Systemes Simulia Corp
- [19] V. Aune, G. Valsamos, F. Casadei, M. Langseth, T. Børvik *On the dynamic response of blast-loaded steel plates with and without pre-formed holes* In: International Journal of Impact Engineering 108 (2017) pp:27-46
- [20] G. Gruben, E. Fagerholt, O. S. Hopperstad, and T. Børvik *characteristics of a cold-rolled dual-phase steel* In: European Journal of Mechanics A/Solids, 30:204–218, 2011
- [21] G. Gruben, O. S. Hopperstad, and T. Børvik *Evaluation of uncoupled ductile fracture criteria for the dual-phase steel Docol 600DL* In: International Journal of Mechanical Sciences, 62:133–146, 2012
- [22] J. K. Holmen, O. S. Hopperstad, and T. Børvik *Low velocity impact on multi-layered dual-phase steel plates* In: International Journal of Impact Engineering, 78:161–177, 2015
- [23] C. N. Kingery and G. Bulmash. *Airblast Parameters from TNT Spherical Air Burst and Hemispherical Surface Burst*. In: Defence Technical Information Center, Ballistic Research Laboratory, Aberdeen Proving Ground, Maryland, 1984.

-
- [24] F. Casadei, M. Larcher, and N. Leconte. *Strong and Weak Forms of a Fully Non-conforming FSI Algorithm in Fast Transient Dynamics for Blast Loading of Structures* In: Proceedings of the 3rd International Conference on Computational Methods in Structural Dynamics and Earthquake Engineering (COMPDYN 2011), pages 1120–1139, 2011.
- [25] *Properties of dry air* [ONLINE] Available at: www.engineeringtoolbox.com/dry-air-properties-d_973.html [Accessed 3rd June 2018].
- [26] *Navier-Stokes Equation* [ONLINE] Available at: www.continuummechanics.org/navierstokes.html [Accessed 25th April 2018].
- [27] *Europlexus Users Manual* [ONLINE] Available at: http://europlexus.jrc.ec.europa.eu/public/manual_pdf/manual.pdf [Accessed 1st June 2018].
- [28] *SIMULIA Abaqus 2016 Theory Guide, Section 5.2.3 Coulomb friction* [ONLINE] Available at: <http://ivt-abaqusdoc.ivt.ntnu.no:2080/v2016/books/stm/default.htm?startat=ch04s04ath117.html> [Accessed 1st May 2018].
- [29] *Lecture 1, Overview of ABAQUS/Explicit, by ABAQUS* Available at: <https://pdfs.semanticscholar.org/presentation/afcd/576d8b8c92b7475b58c2952f8c0a3a9805f0.pdf> [Accessed 3rd June 2018]
- [30] *LS-DYNA support, Hourglass* Available at: <https://www.dynasupport.com/howtos/element/hou> [Accessed 3rd June 2018]
- [31] F. Casadei, P. Diez, F. Verdugo *An algorithm for mesh refinement and un-refinement in fast transient dynamics* In: International Journal of Computational Methods 2013; 10: 1-31.
- [32] Y.A. Cengel and J.M. Cimbala *Fluid Mechanics: Fundamentals and Applications* McGraw-Hill, second edition, 2010.
- [33] D. Cormie, G. Mays, P. Smith. *Blast effects on buildings* Thomas Telford, London, UK, Second edition.
- [34] E. F. Toro *Riemann Solvers and Numerical Methods for Fluid Dynamics* Springer, 2009.
- [35] B. Müller *Introduction to Computational Fluid Dynamics* Lecture notes for the course Computational Heat and Fluid Flow, Department of Energy and Process Engineering, Norwegian University of Science and Technology (NTNU), Trondheim, Norway Version of 15 August 2014
- [36] F. M. White *Viscous Fluid Flow* McGraw-Hill, second edition, International Edition

Bibliography

- [37] V. Aune, E. Fagerholt, M. Langseth and T. Børvik A shock tube facility to generate blast loading on structures. Found in: *International Journal of Protective Structures*, (2016), Vol. 7(3).
- [38] W. M Lai, D. Rubin and E Krempl. (2010). *Introduction to Continuum Mechanics* [4th Ed.]. Oxford: Butterworth-Heinemann.
- [39] SAS IP, Inc. (2016). Lagrangian and Eulerian Reference Frames. Available at: https://www.sharcnet.ca/Software/Ansys/16.2.3/en-us/help/wb_sim/exp_dyn_theory_lag_eul_360.html
- [40] R. D. Cook, D. S. Malkus, M. E Plesha, R. J. Witt. (2002). *Concepts and Applications of Finite Element Analysis*. Hoboken, NJ: Wiley.
- [41] T. Belytschko, W. K. Liu, B. Moran. (2000). *Nonlinear Finite Elements for Continua and Structures*. Hoboken, JJ: Wiley.
- [42] L. Olovsson, J. Limido, J. L Lacome, A. G. Hanssen, and J Petit. (2015). Modeling Fragmentation With New High Order Finite Element Technology and Node Splitting. *The European Physical Journal Conferences Web of Conferences*. 94. 04050.
- [43] F. G. Friedlander. (1946). The diffraction of sound pulses. I. Diffraction by a semi-infinite plane. *Proceedings of the Royal Society A: Mathematical, Physical and Engineering Science* 186(1006). 322–344.
- [44] E. F. Toro. (2009). *Riemann solvers and numerical methods for fluid dynamics* [3rd Ed.]. Berlin: Springer-Verlag
- [45] V. Aune, Folco Casadei, Georgios Valsamos, Magnus Langseth and Tore Børvik *A shock tube used to study the dynamic response of blast-loaded plates* Presented at: 18th International Conference on Experimental Mechanics (ICEM18), Brussels 1-5 July 2018.
- [46] V. Aune, G. Valsamos, F. Casadei, M. Larcher, M. Langseth, T. Børvik. (2016). Numerical study on the structural response of blast-loaded thin aluminium and steel plates. *International Journal of Impact Engineering*, Volume 99, 131-144.
- [47] *Friction and Friction Coefficients* [ONLINE] Available at: https://www.engineeringtoolbox.com/friction-coefficients-d_778.html [Accessed 15th Feb 2018].
- [48] *SIMULIA User Assistance 2017, section; Choosing a shell element* Publisher: Dassault Systemes Simulia Corp
- [49] M. G. Cockcroft and D. J. Latham. Ductility and the workability of metals. *Journal of the Institute of Metals*, 96:33–39, 1968.

- [50] L. Guoa, J. Xianga, J. P. Lathama, B. Izzuddinb. (2016). A numerical investigation of mesh sensitivity for a new three-dimensional fracture model within the combined finite-discrete element method. *Engineering Fracture Mechanics*, Volume 15, 70-91.
- [51] *SIMULIA User Assistance 2017, Section; Abaqus/Explicit output variable identifiers* Publisher: Dassault Systemes Simulia Corp
- [52] *SIMULIA User Assistance 2017, Section; What is the difference between the medial axis algorithm and the advancing front algorithm* Publisher: Dassault Systemes Simulia Corp
- [53] *SIMULIA User Assistance 2017, Section; Three-dimensional solid element library* Publisher: Dassault Systemes Simulia Corp
- [54] *SIMULIA User Assistance 2017, Section; Top-down meshing* Publisher: Dassault Systemes Simulia Corp

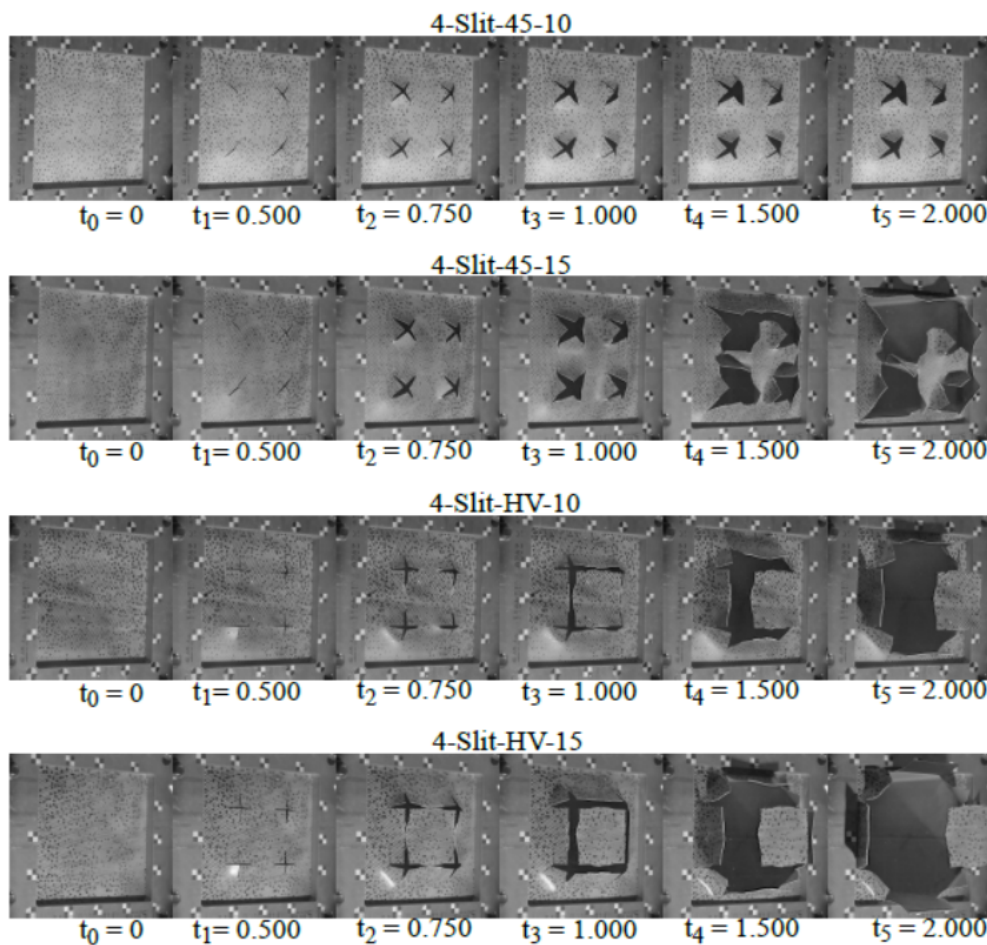
Appendices

Appendix A

Experimental results

A.1 Failure modes obtained from [30]

Figure (A.1) is included in this appendix as a tool to easily compare the failure modes found in aluminum plates compared to steel plates. The last number in the figure text is referring to the nominal firing pressure, and the driver length in this tests was 77cm, equal to the length used in the tests conducted in this thesis.



ii

Figure A.1: Failure modes aluminum plates

A.1.1 Experimentally measured midpoint displacements.

A.1.2 Experimental deformation evolution

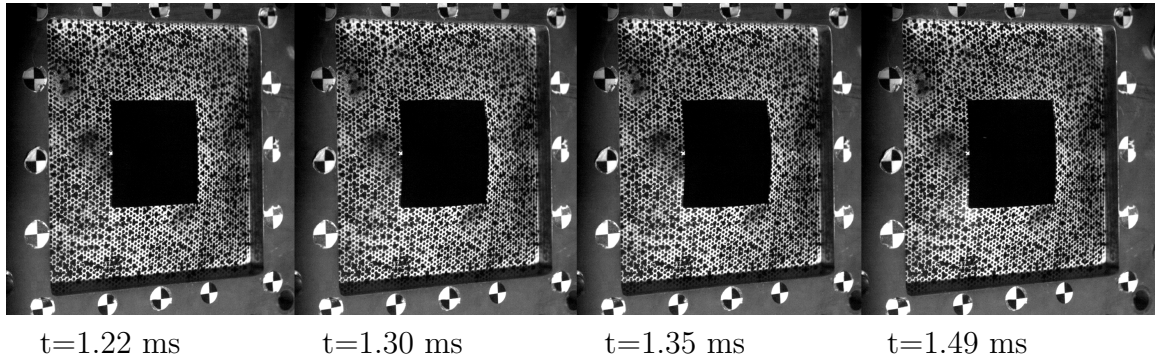


Figure A.2: P1_05

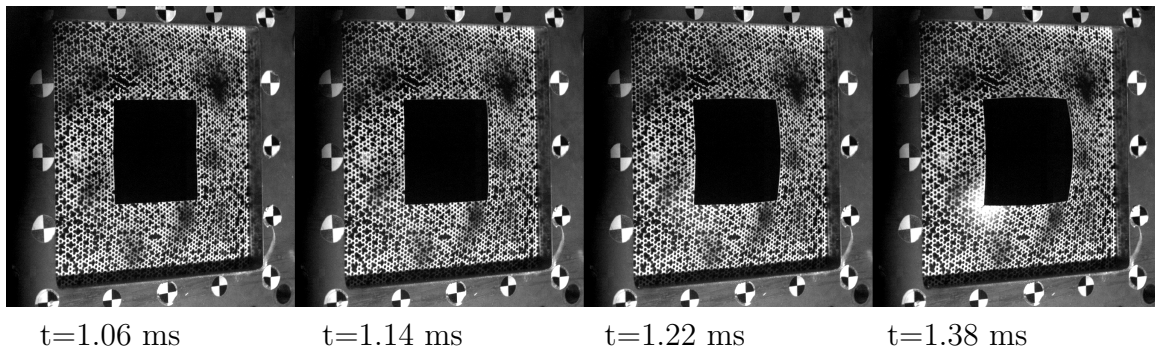


Figure A.3: P1_10

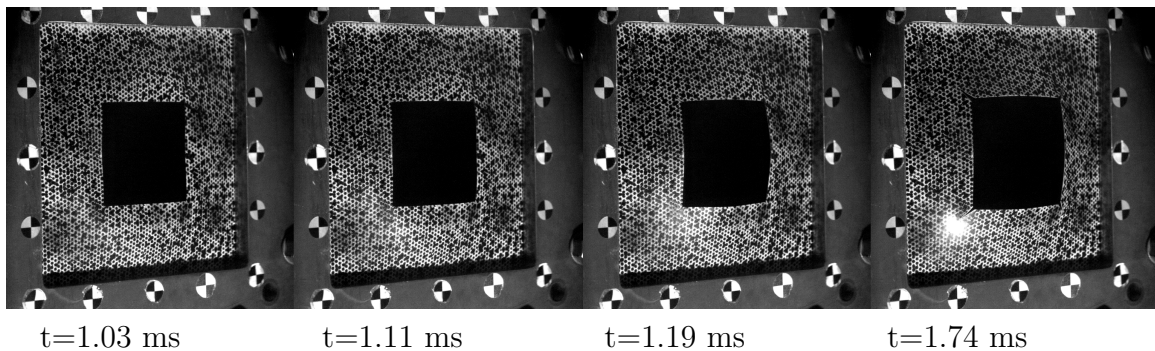


Figure A.4: P1_15

Appendix A. Experimental results

The measured maximum midpoint displacement for each test is listed in Table A.1. In addition, the permanent midpoint deflection measured with both DIC and the laser is given. For consistency, the midpoint displacement data obtained by Granum and Løken [29] is included as a mean of comparison. They were not given the possibility of using the laser scanner, and this column is, therefore, left blank.

Table A.1: Maximum midpoint displacement measured with DIC, and permanent midpoint displacements measured with DIC and the laser arm.

| Test | Maximum MPD | Permanent MPD | Permanent MPD |
|-------|-------------|---------------|---------------|
| | DIC [mm] | DIC [mm] | Laser [mm] |
| P1.05 | 18.2 | 13.5 | 13.0 |
| P1.10 | 25.0 | 24.2 | 21.5 |
| P1.15 | 34.7 | 30.6 | 25.98 |
| P1.25 | - | - | - |
| FP.15 | 25.5 | 22.1 | - |
| FP.25 | 31.3 | 28.8 | - |
| FP.35 | 36.2 | 34.5 | - |
| P2.15 | 29.6 | 26.9 | - |
| P2.25 | 37.3 | 36.3 | - |
| P3.25 | 37.8 | 34.1 | 33.7 |
| P3.35 | - | - | - |
| S1.05 | 15.6 | 11.4 | 11.6 |
| S1.10 | 22.8 | 18.9 | 19.5 |
| S1.15 | - | - | - |
| S2.10 | 21.3 | 17.4 | 17.7 |
| S2.15 | 26.5 | 23.4 | 23.6 |
| S2.25 | 35.6 | 32.0 | 32.0 |

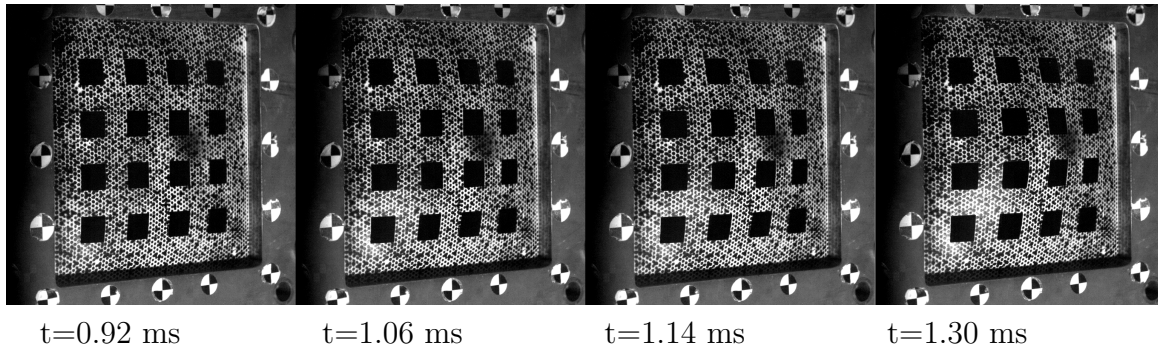


Figure A.5: P3.25

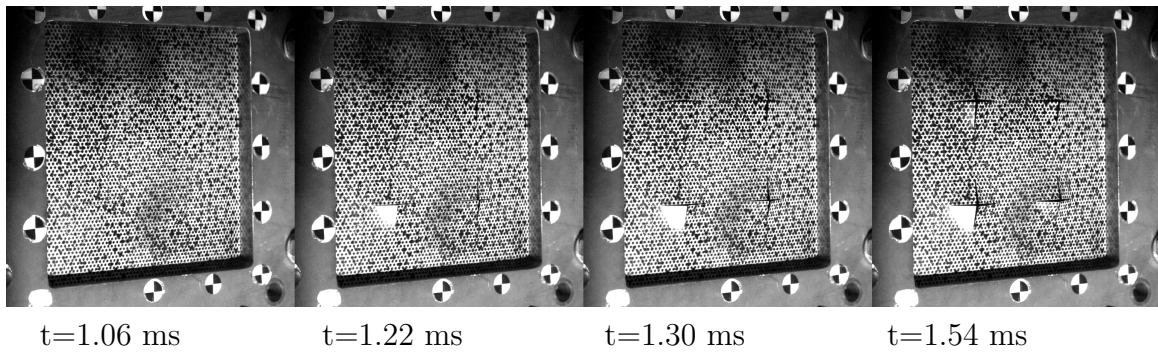


Figure A.6: S1.05

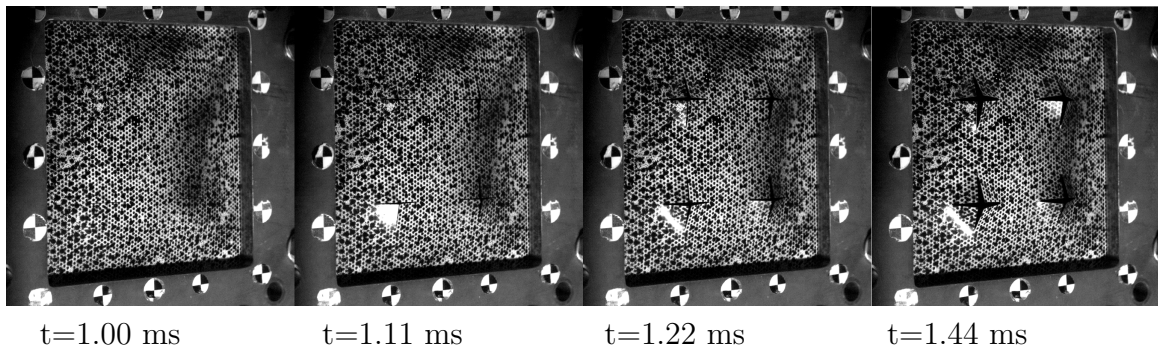


Figure A.7: S1.10

Appendix A. Experimental results

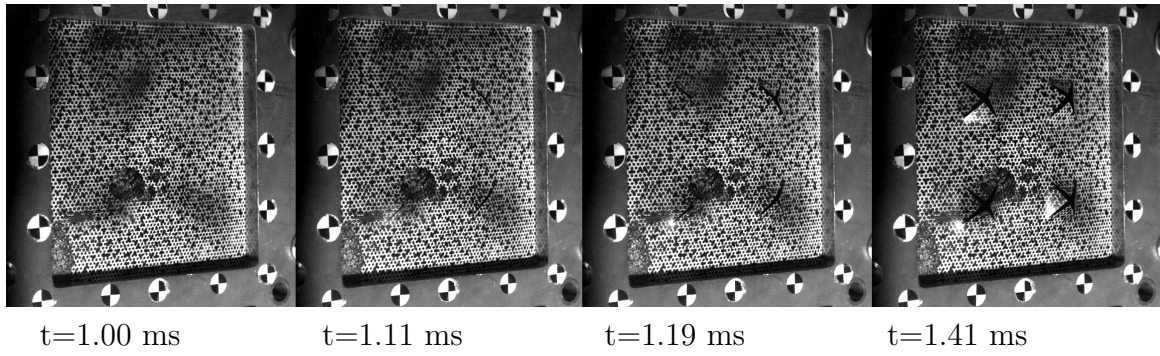


Figure A.8: S2.10

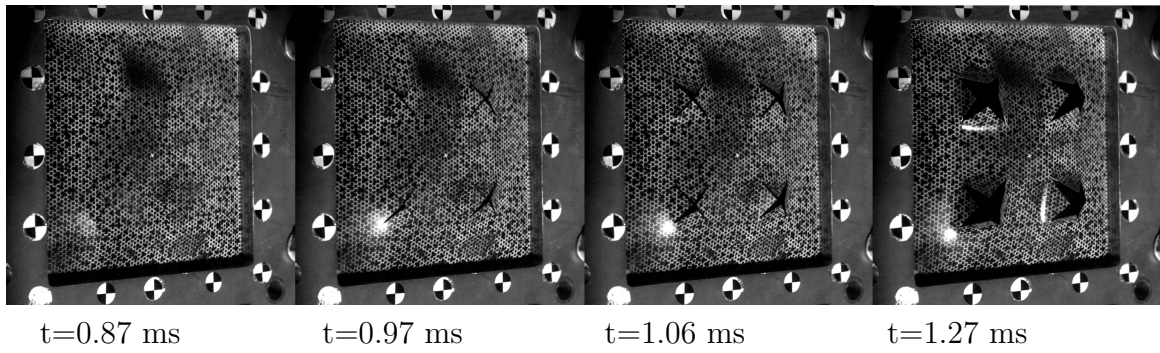


Figure A.9: S2.25

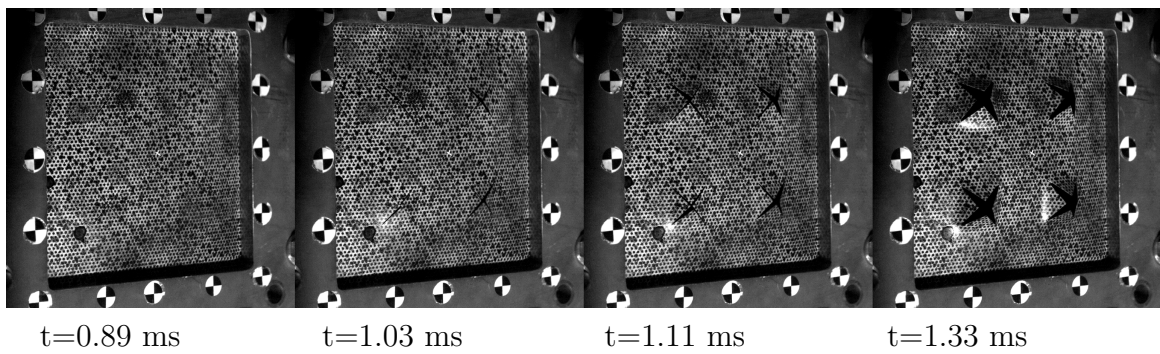
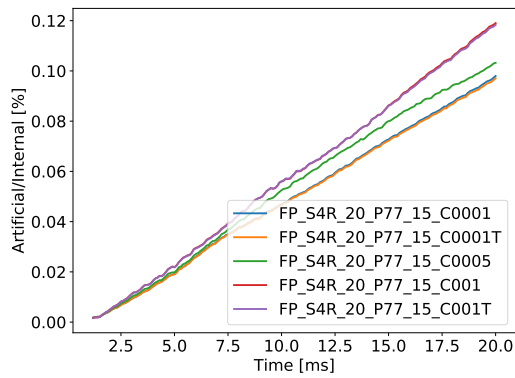


Figure A.10: S2.15

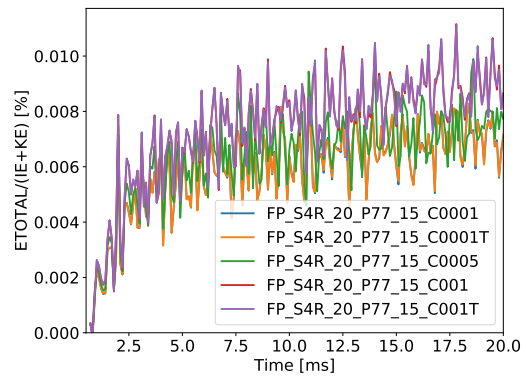
Appendix B

Numerical results

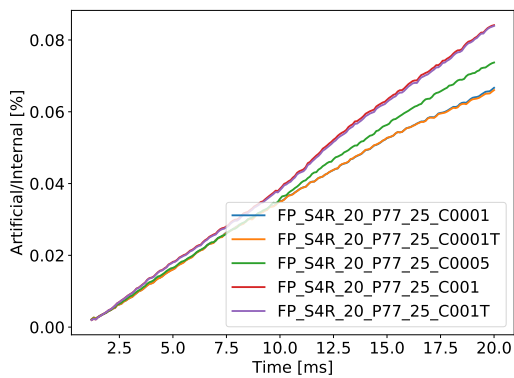
B.1 Energy plots from Chapter 5



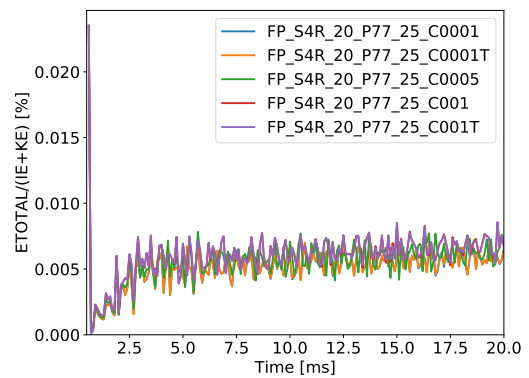
(a) Artificial energy



(b) Conservation of energy



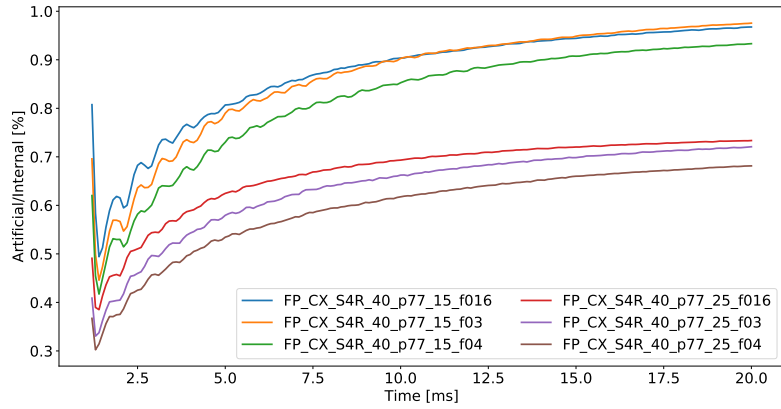
(c) Artificial energy



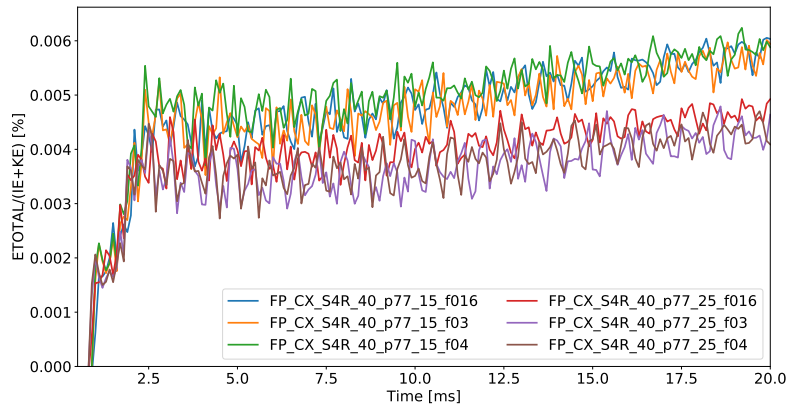
(d) Conservation of energy

Figure B.1: Plots from models i Chapter 5

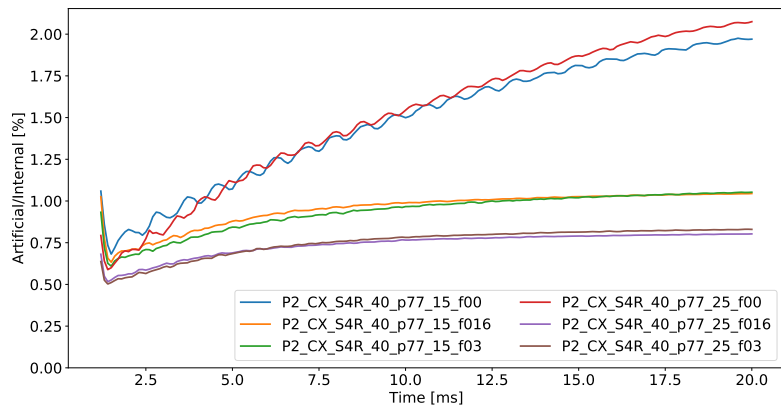
Appendix B. Numerical results



(a) Artificial energy



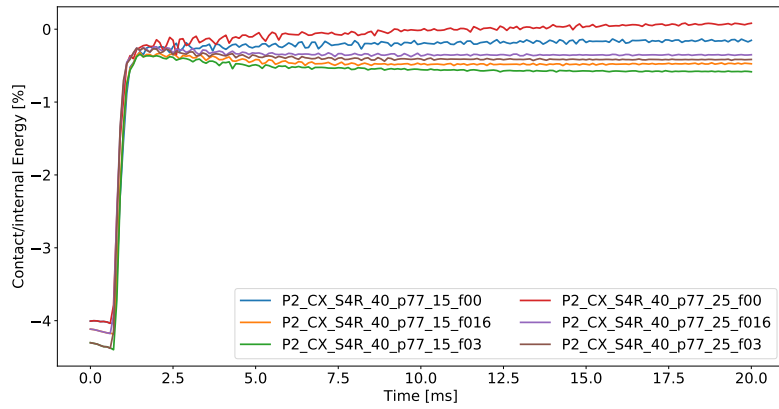
(b) Conservation of energy



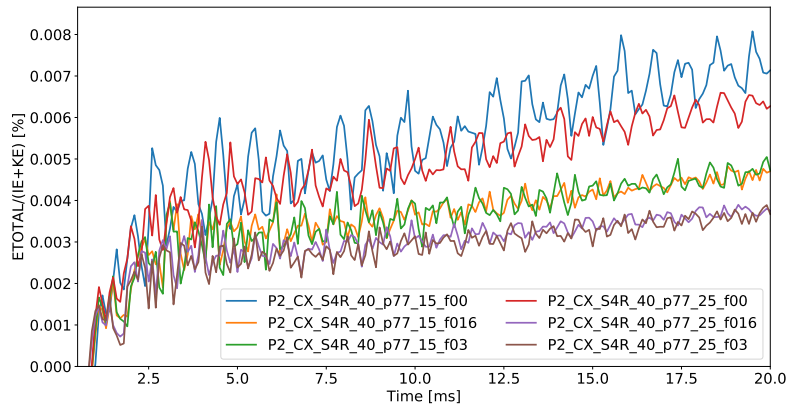
(c) Artificial energy

Figure B.2: Plots from models i preliminary study Part II

B.1. Energy plots from Chapter 5



(a) Contact energy



(b) Conservation of energy

Figure B.3: Plots from models i preliminary Chapter 5

B.2 Midpoint displacement plots for from Chapter 7

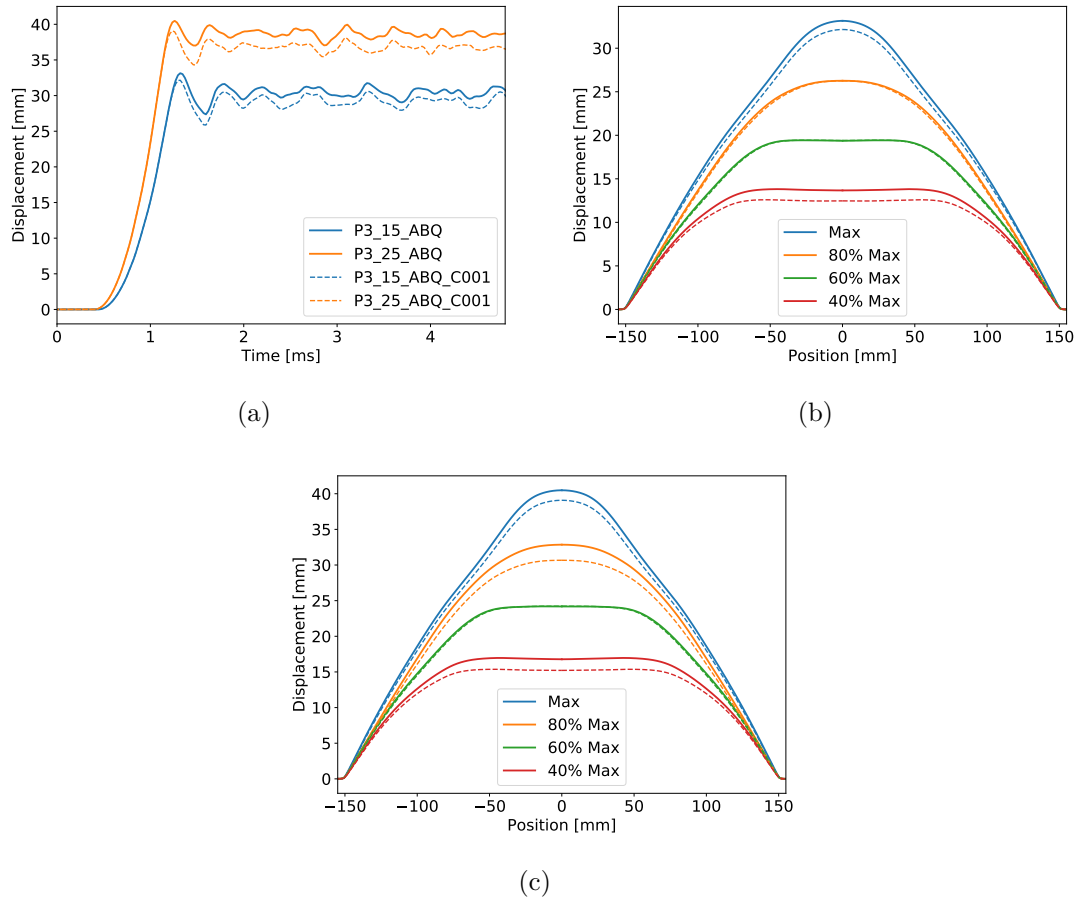


Figure B.4: (a) Midpoint displacements, (b) and (c) are showing Deformation profiles

For the midpoint displacements, the same trend as found in the preliminary study is observed. The solution gets slightly stiffer for a higher rate dependency but is still over-predicting the displacements with respect to experimental results.

B.3 Effect of excluding the pre-tension in the bolts for the clamping frame

As mentioned in the description of the models, the tightening of the bolts is modeled slightly different in Abaqus and Europlexus. Due to the deviation in response shown in the previous section, it was decided to check the effect of varying the pre-tension in the bolts for the Abaqus model. The models labeledLB has the clamping frame, bolts, and contact modeled in the same way at the other Abaqus models, but the bolt tightening step is removed. This means that when the loading is being applied to the plates, the bolts are completely stress-free. For comparison, both the midpoint displacement and the sliding at the supports has been measured for the simulations. The sliding was measured by finding the relative distance in the x-direction between a node on the clamping frame, and a node at the testing plate initially placed in the same x-position. The nodes applied for measurements are indicated in Figure B.5(c)

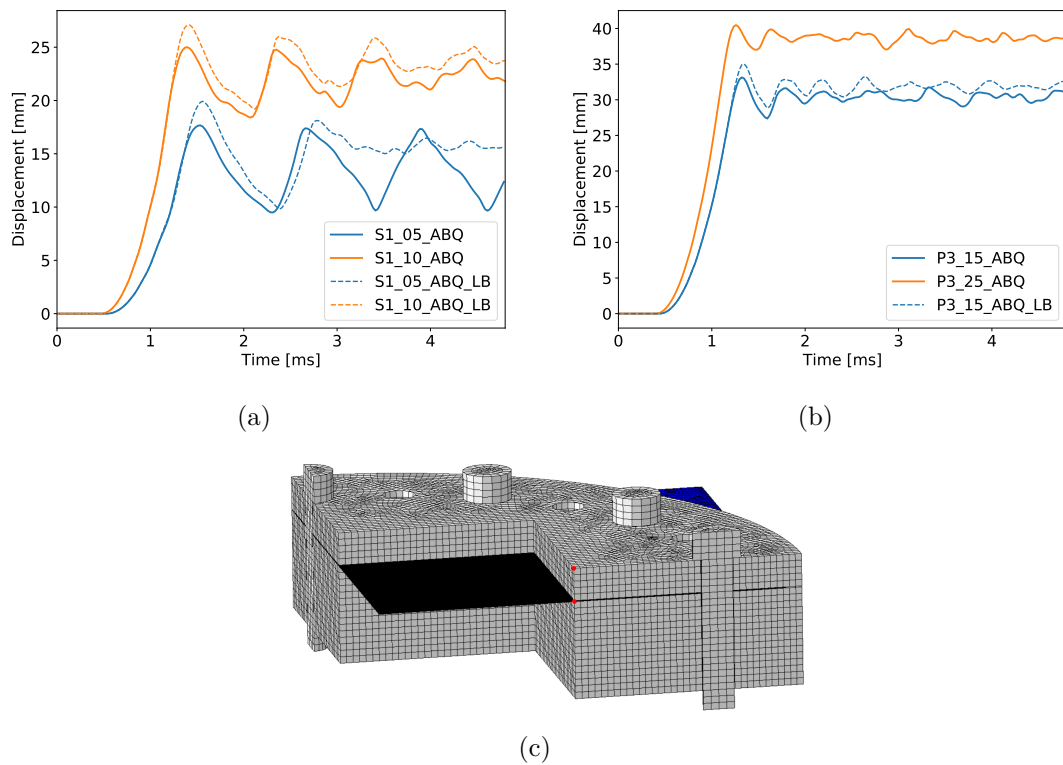


Figure B.5: Shows the effect of not including pre-tension in the bolts for the clamping frame. (a) Midpoint displacements vs. time for S1, (b) Midpoint displacements vs. time for P3 and (c) is showing the defined points for evaluation of sliding at the supports.

Appendix B.

As seen from the midpoint displacement response shown in figure (B.5(b)) the effect of loose bolts is allowing for a much softer behavior. An increase of 11% and 8% is obtained for firing pressures of 5bar and 10bar respectively. The sliding is increased with 0.27mm and 0.25mm for the two tests. By evaluating these results it is evident that the behavior if the plates are sensitive to changes in the modeling of the boundary.

Another important observation is that the oscillations for the firing pressure of 5bar are highly reduced for the models applying loose bolts. This might be due to more sliding at the supports resulting in an increased frictional damping for the system.

Table B.1: Maximum midpoint displacement and relative sliding. The sliding at the supports are measured as the relative movement in x-direction between the two points indicated in Figure B.5(b).

| Configuration | MPD, max [mm] | Sliding at supports [mm] |
|---------------|------------------|-----------------------------|
| S1.05_A | 17.67 | 0.31 |
| S1.05_A.LB | 19.92 | 0.58 |
| S1.10_A | 25.00 | 0.52 |
| S1.10_A.LB | 27.08 | 0.77 |
| P3.15_A | 33.14 | 0.43 |
| P3.15_A.LB | 35.03 | 0.65 |
| P3.25_A | 40.49 | 0.53 |
| P3.25_A.LB | | |

B.3. Effect of excluding the pre-tension in the bolts for the clamping frame

B.3.1 Tables from Chapter 7

Table B.2: Maximum midpoint displacement, the deviation between simulated results and experimental data, and the time it takes to reach the maximum displacement. The time relates to the defined time axis defined in section 6.2.2.

| Configuration | MPD, max [mm] | Deviation, MPD % | Time [ms] |
|-----------------|------------------|---------------------|--------------|
| P1_05 | 17.95 | - | 1.49 |
| P1_05_ABQ | 21.15 | 20 | 1.49 |
| P1_05_EPX.L | 22.83 | 30 | 1.54 |
| P1_05_Fix_EPX.L | 20.98 | | 1.52 |
| P1_10 | 25.22 | - | 1.38 |
| P1_10_ABQ | 29.69 | 18 | 1.36 |
| P1_10_EPX.L | 31.49 | 25 | 1.41 |
| P1_10_Fix_EPX.L | 29.76 | | 1.40 |
| P3_15 | | - | - |
| P3_15_ABQ | 33.14 | - | 1.32 |
| P3_15_C001 | 32.15 | - | 1.32 |
| P3_15_EPX.L | 36.71 | - | 1.38 |
| P3_15_Fix_EPX.L | 34.78 | - | 1.37 |
| P3_25 | 37.95 | - | 1.30 |
| P3_25_ABQ | 40.49 | 7 | 1.26 |
| P3_25_C001 | 39.08 | 3 | 1.24 |
| P3_25_EPX.L | 45.24 | 19 | 1.31 |
| P3_25_Fix_EPX.L | 43.24 | | 1.31 |

Appendix B.

Table B.3: Maximum midpoint displacement, the deviation between simulated results and experimental data, and the time it takes to reach the maximum displacement. The time relates to the defined time axis defined in section 6.2.2.

| Configuration | MPD, max [mm] | Deviation, MPD % | Time [ms] |
|-----------------|------------------|---------------------|--------------|
| S1_05 | 15.60 | - | 1.54 |
| S1_05_ABQ | 17.67 | 13 | 1.54 |
| S1_05_EPX_L | 18.74 | 20 | 1.77 |
| S1_05_Fix_EPX_L | 16.88 | | 1.77 |
| S1_10 | 22.51 | - | 1.44 |
| S1_10_ABQ | 25.00 | 11 | 1.39 |
| S1_10_EPX_L | 26.80 | 19 | 1.66 |
| S1_10_Fix_EPX_L | 25.18 | | 1.67 |
| S2_10 | 21.17 | - | 1.41 |
| S2_10_ABQ | 23.87 | 12 | 1.37 |
| S2_10_EPX_L | 25.56 | 21 | 1.62 |
| S2_10_Fix_EPX_L | 23.89 | | 1.66 |
| S2_15 | 26.87 | - | 1.33 |
| S2_15_ABQ | 28.71 | 7 | 1.25 |
| S2_15_EPX_L | 31.55 | 17 | 1.55 |
| S2_15_Fix_EPX_L | 29.84 | | 1.55 |

B.3. Effect of excluding the pre-tension in the bolts for the clamping frame

B.3.2 Pressure distribution from Chapter 7

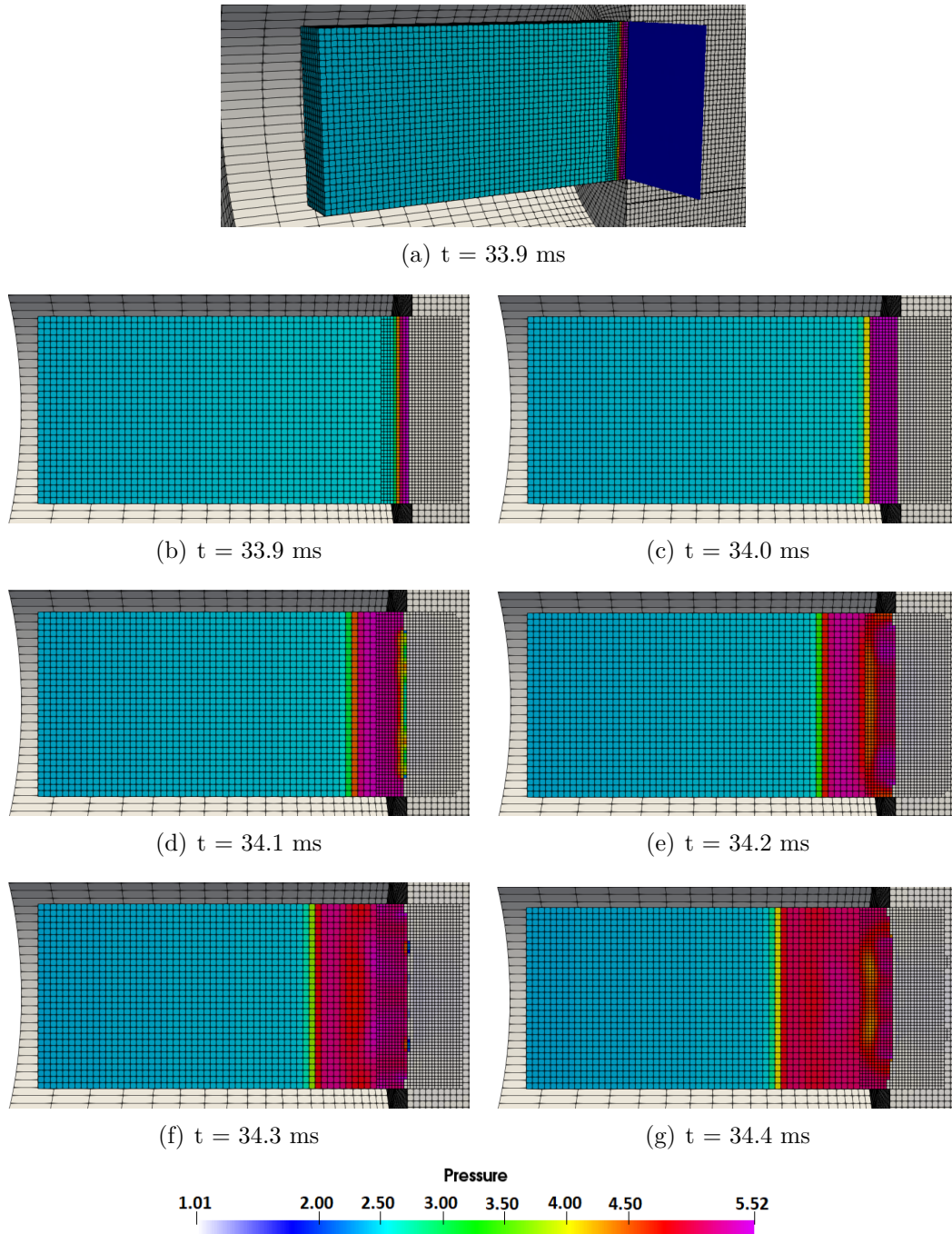


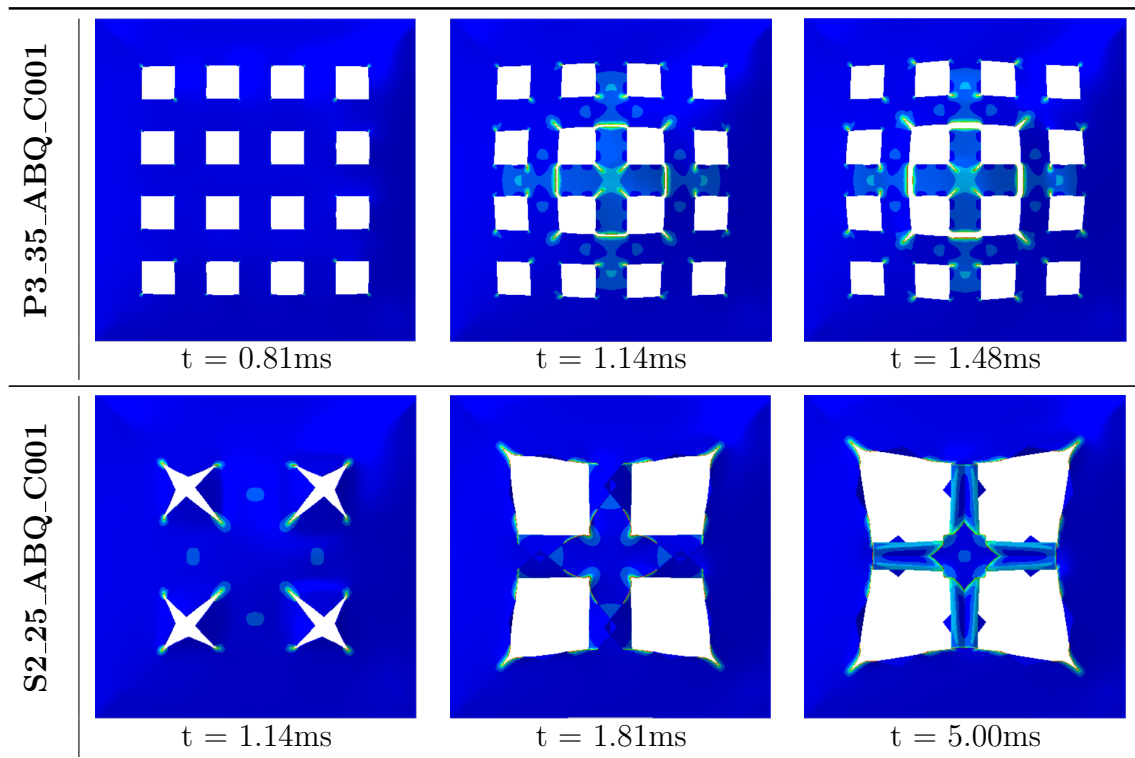
Figure B.6: The pressure distribution in front of the S1 configuration at the nominal firing pressure of 10 bar is shown. The field maps are taken from the fully coupled Eulerian-Lagrangian simulations in Europlexus, and the color shades represent the pressure in bar. All images are labeled with the total time in the simulation, which includes the propagation of the shock wave before reaching the plate. The presented field maps are taken from the cut given in image (a), and the grey mesh represents the air initially at rest in the dump tank. Note that the slits are not visible in the undeformed configuration.

B.3.3 Varying the strain rate sensitivity for P3 and S2

As a result of the deviations in failure modes observed between the numerical models of the P3- and the S2 configuration compared to experimental results and previous numerical work, it was decided to conduct a small parametric study. The strain rate sensitivity parameter c is changed from 0.005 to 0.01.

In this section, only the effect on the failure modes will be presented as a similar study evaluating the midpoint displacement response was performed in Chapter 5. However, the obtained midpoint displacement plots from this section are included in the Appendix. Due to high computational costs, the study is limited to only consider P3 and S2, and the obtained failure modes are shown in Table B.4.

Table B.4: Failure modes obtained by changing the strain rate sensitivity from $c = 0.005$ to $c = 0.01$ for the complex models of P3 at 35 bar and S2 at 25 bar.



B.3. Effect of excluding the pre-tension in the bolts for the clamping frame

From the results presented in Table B.4 it is evident that the failure modes are dependent on the strain rate sensitivity parameter. For $c = 0.005$, seen in the previous section, both S2_25_ABQ and P3_35_ABQ went to complete failure. By increasing the dependency to $c = 0.01$, both simulations resulted in crack arrest rather than failure. However, the deformation pattern for S2 is rather unrealistic. Due to the symmetric model, flaps are being bent outwards and wrapped around the outer boundary of the quarter model, as shown in Figure B.7. When visualizing the full geometry, by mirroring the model across the two symmetry planes, it is seen that the flaps are penetrating each other. This deformation is clearly non-physical, and can only be accounted for by modeling the full geometry, or with a more advanced contact formulation.

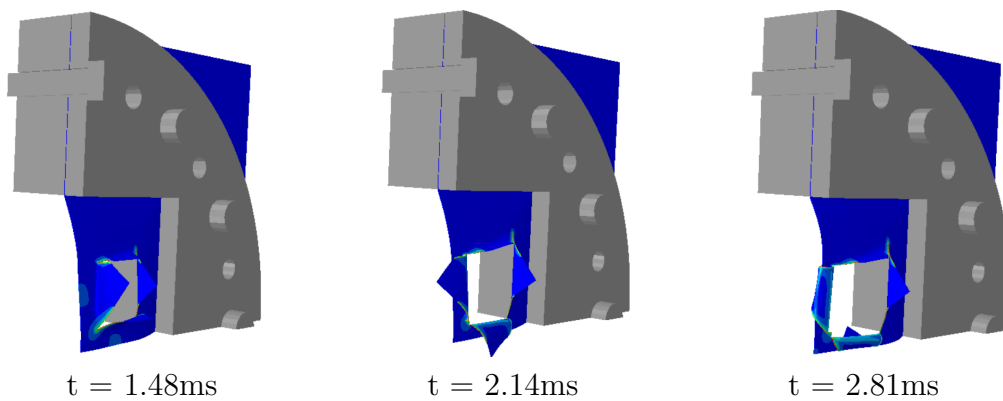


Figure B.7: Failure mode for the quarter model S2_25_A_C001

Regarding the P3 configuration, it is interesting to note that the failure pattern is rather unstable in the numerical simulations. When comparing the failure mode obtained in Chapter 4 with the two modes found with the complex models varying the strain rate sensitivity parameter, it gives three different failure modes.

B.3.4 Evaluation of displacements, from Chapter 7

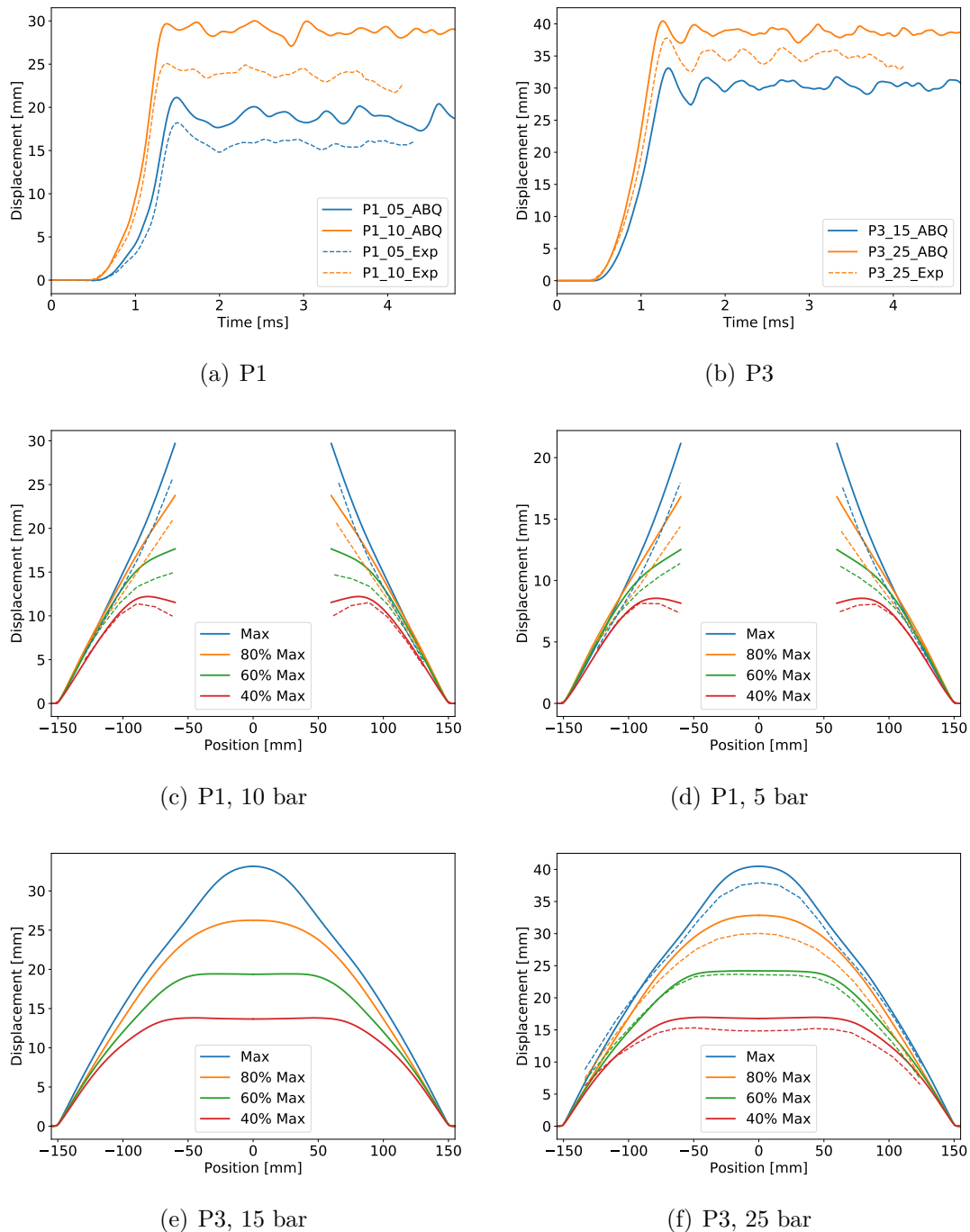
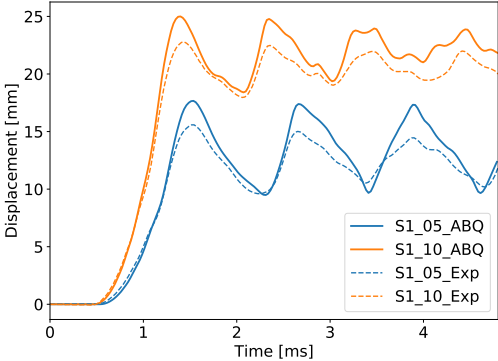


Figure B.8: Midpoint displacements vs. time and deformation profiles for experimentally obtained data compared to pure Lagrangian model in Abaqus. Dotted lines represents the experimentally obtained data.

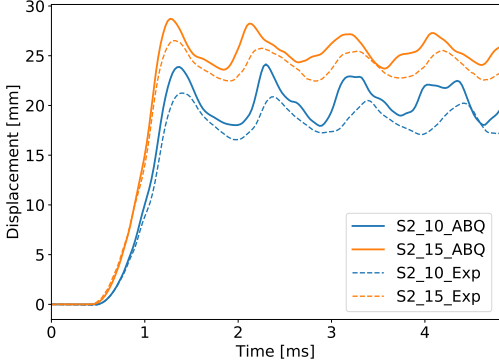
B.3. Effect of excluding the pre-tension in the bolts for the clamping frame

Regarding the deformation profiles, it is important to note that the sampling frequency used to log displacement data in the simulations is too low compared to the rapid response of the plates. The profiles are created by collecting displacement data at 80%, 60% and 40% of the maximum displacement respectively, but the low frequency results in a deviation of approximately $\pm 2\%$. This error is especially evident in the S2_15 test, as seen in Figure B.8. Here, the deformation profiles obtained numerically and experimentally coincide at 40% of max displacement, but are deviating at the maximum displacement. As a result of the low sampling rate, the profiles are not directly comparable. However, for all configurations and all firing pressures both the development of the profiles and the profiles when the maximum displacement is reached are qualitatively equal to the experimental results.

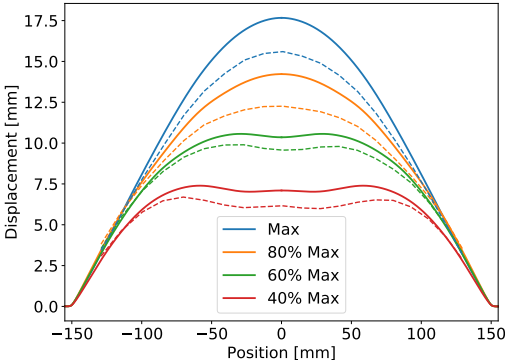
Appendix B.



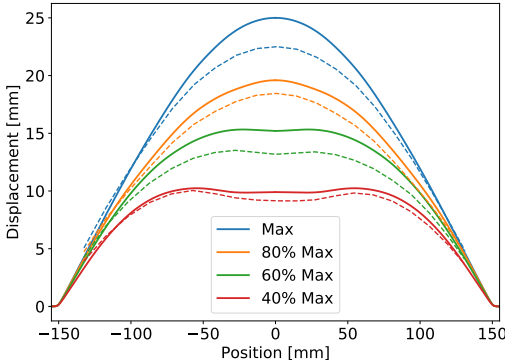
(a) S1



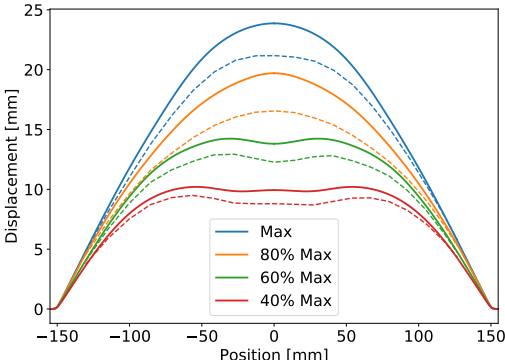
(b) S2



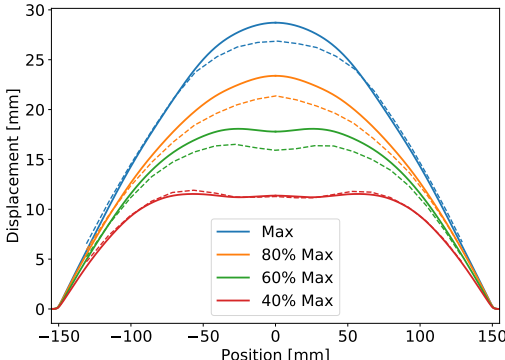
(c) S1, 5 bar



(d) S1, 10 bar



(e) S2, 10 bar



(f) S2, 15 bar

Figure B.9: Midpoint displacements vs.time and deformation profiles for experimentally obtained data compared to pure Lagrangian model in Abaqus. Dotted lines represents the experimentally obtained data.